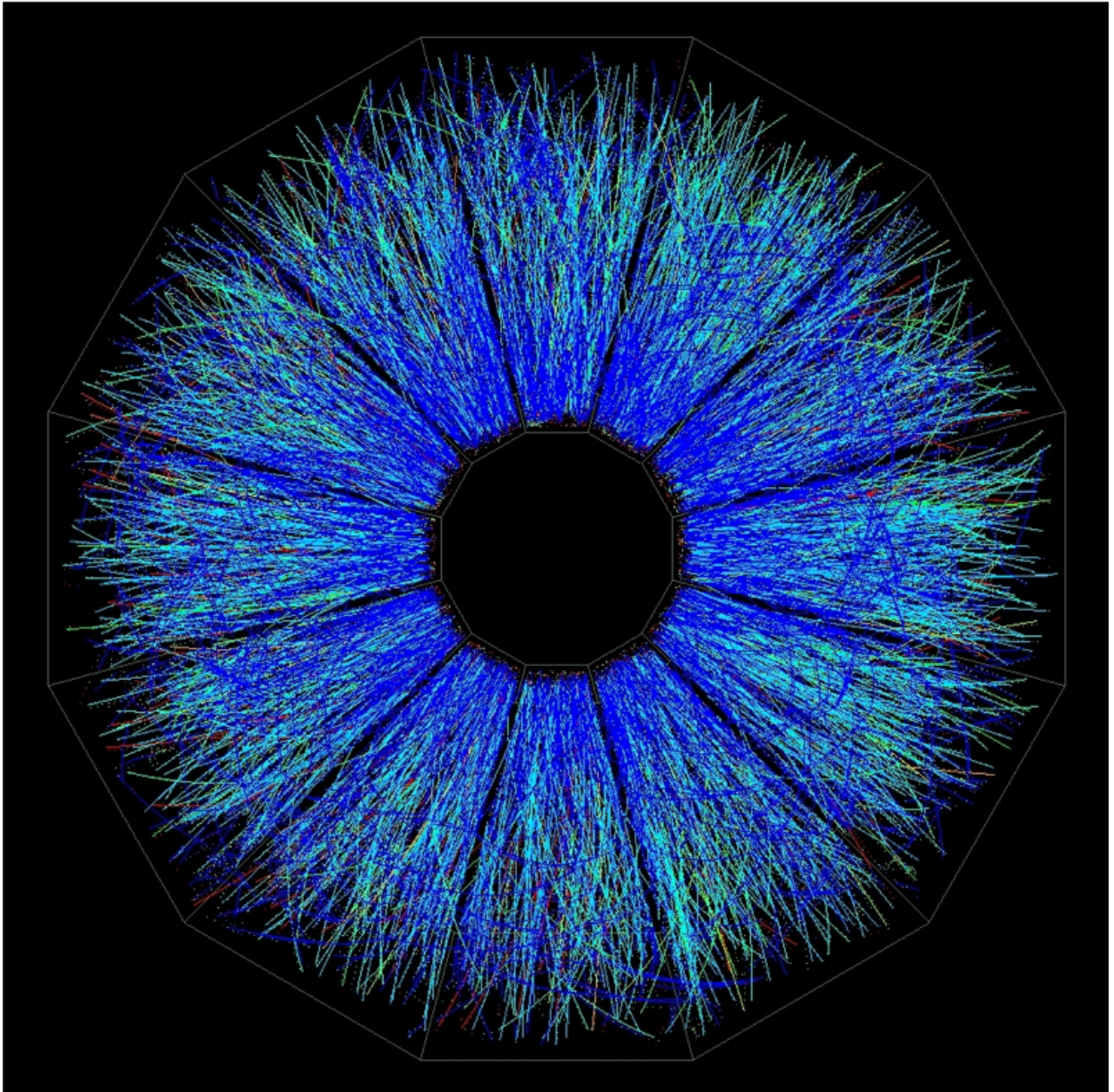


# The STAR Beam Use Request for Runs 19 and 20

The STAR Collaboration



May 1, 2018

## Executive Summary

This Beam Use Request from the STAR collaboration for RHIC Runs 19 and 20 is focused on the NSAC endorsed [1] Beam Energy Scan Phase II (BES-II) program and is key to the completion of the RHIC BES mission which started in 2010 and completed its Phase I milestone in 2014. Collection of all the data outlined in 1 is STAR **highest scientific priority**.

BES-II will dramatically enhance our understanding of the QCD phase diagram. The proposed program involves dedicated low beam energy running and high precision measurements of the observables that have been found to be sensitive to the phase structure of QCD matter. In addition to the four lower energies from BES-I, STAR’s plan is to run a fifth beam energy at  $\sqrt{s_{NN}} = 9.1$  GeV. This energy will bridge the large gap in chemical potential between the 7.7 and 11.5 GeV energies.

**Table 1:** Summary of all BES-II and FXT Au+Au beam energies, equivalent chemical potential, requested event statistics, and run times.

Beam Energy (GeV/nucleon)	$\sqrt{s_{NN}}$ (GeV)	$\mu_B$ (MeV)	Run Time	Number Events
9.8	19.6	205	4.5 weeks	400M
7.3	14.5	260	5.5 weeks	300M
5.75	11.5	315	5 weeks	230M
4.55	9.1	370	9.5 weeks	160M
3.85	7.7	420	12 weeks	100M
31.2	7.7 (FXT)	420	2 days	100M
19.5	6.2 (FXT)	487	2 days	100M
13.5	5.2 (FXT)	541	2 days	100M
9.8	4.5 ( FXT)	589	2 days	100M
7.3	3.9 (FXT)	633	2 days	100M
5.75	3.5 (FXT)	666	2 days	100M
4.55	3.2 (FXT)	699	2 days	100M
3.85	3.0 (FXT)	721	2 days	100M

The collaboration proposes to extend its energy range further down to lower center-of-mass energies by means of a fixed-target (FXT) program. The proposed energies for both collider and fixed-target mode are summarized in Table 1.

Three upgrades were proposed for BES-II. Both the inner Time Projection Chamber (iTTPC) and the endcap Time of Flight (eTOF) are on schedule for full installation in Run 19; these increase the rapidity and low transverse momentum acceptance of STAR, and extend our particle identification capabilities. The event plane detector (EPD) is currently being commissioned as it was completed and installed prior to Run 18.

STAR’s **highest scientific priority for Run 19** is the commencement of the RHIC Beam Energy Scan II. The collaboration proposes to start with the two highest beam energies

in collider mode (19.6 and 14.5 GeV), as well as the associated FXT energies (4.5 and 3.9 GeV). Next, FXT energies starting at  $\sqrt{s_{NN}}=7.7$  GeV should follow. Access to FXT data at  $\sqrt{s_{NN}}=7.7$  GeV will provide for an important cross-check with the collider-mode data at that same energy. We list the Run-19 priorities and proposed sequence in Table 2

STAR’s **highest scientific priority for Run 20** is the continuation of the RHIC Beam Energy Scan II. The collaboration proposes to start with the highest beam energies in collider mode, as well as the fixed-target energies that are associated with the single-beam energies for those collider-mode energies.

The request for the start of the BES-II program considers the following scenarios:

- Scenario 1: 19 cryo-weeks in 2019 and and 24 cryo-weeks 2020 (Tables 2, 3)
- Scenario 2: 19 cryo-weeks in 2019 and 2020 (Tables 2, 4)
- Scenario 3: 24 cryo-weeks in 2019 and 2020 (Tables 2, 5)
- Scenario 4: 24 cryo-weeks in 2019 and and 19 cryo-weeks 2020 (Tables 2, 6)

With guidance from the Collider-Accelerator Department, each scenario has cryo-weeks assigned to commissioning of Low-Energy RHIC electron Cooling (LEReC): six weeks in Run 19 and five weeks in Run 20. For all scenarios we have to assume a third year of RHIC running to follow, in order to allow the completion of the BES-II physics mission. Specifically, the request of twelve weeks for  $\sqrt{s_{NN}} = 7.7$  GeV will need to be collected in a third year of BES-II. Moreover, some scenarios necessitate this third run to address parts of the requests for the  $\sqrt{s_{NN}} = 9.1$  GeV. Run 21 would thus combine the remainder of BES-II with the start of STAR’s forward physics program which would see a  $\sqrt{s} = 500$  GeV polarized  $pp$  run that year as proposed in [2, 3].

For scenarios 3 and 4, STAR proposes to split the cryo-week budget between a nineteen-week run in the Spring of 2019 and combine the remaining five weeks with part of the cryo-week budget of Run 20 to allow for second run in the Fall of 2019. Tables 5 and 6 provide more details. Consequently, the Beam Use Request for the first nineteen cryo-weeks of Run 19 will be similar for every scenario and is listed in Table 2.

This BUR document is outlined as follows: first, as requested, in Section 1 we report highlights from analyses completed since the last PAC meeting, with a focus on data from Runs 14-17. Sections 2 and 3 detail the STAR Collaboration’s BES-II and Fixed-Target physics programs which motivates the Run 19 and Run 20 beam use request. Next in Section 4 we outline the status of the upgrades intended for both programs.

**Table 2: Scenarios 1, 2, 3, and 4** -Run 19 assuming nineteen cryo-weeks of running, including six weeks of LEReC commissioning, and two weeks of cool-down/set-up time

Single-Beam Energy (GeV/n)	$\sqrt{s_{NN}}$ (GeV)	Run Time	Species	Events	Priority	Sequence
9.8	19.6	4.5 weeks	Au+Au	400M	1	1
9.8	4.5 (FXT)	2 days	Au+Au	100M	2	2
7.3	14.5	5.5 weeks	Au+Au	300M	1	3
7.3	3.9 (FXT)	2 days	Au+Au	100M	2	4
31.2	7.7 (FXT)	2 days	Au+Au	100M	3	5

**Table 3: Scenario 1** - Run 20 assuming twenty-four cryo-weeks of running, including five weeks of LEReC commissioning, and two weeks of cool-down/set-up time.<sup>1</sup>

Single-Beam Energy (GeV/n)	$\sqrt{s_{NN}}$ (GeV)	Run Time	Species	Events	Priority	Sequence Spring 2020
5.75	11.5	5 weeks	Au+Au	230M	1	1
5.75	3.5 (FXT)	2 days	Au+Au	100M	2	2
4.55	9.1	7 weeks <sup>2</sup>	Au+Au	118M <sup>2</sup>	1	3
4.55	3.2 (FXT)	2 days	Au+Au	100M	3	4
19.5	6.2 (FXT)	2 days	Au+Au	100M	3	5
13.5	5.2 (FXT)	2 days	Au+Au	100M	3	6
3.85	3.0 (FXT)	2 days	Au+Au	100M	4	7

<sup>1</sup> The BES-II request includes a 7.7 GeV run which requires 12 cryo-weeks. This data set will need to be collected in a third year of BES-II.

<sup>2</sup> The complete request is for 160M MB events and will take 9.5 cryo-weeks to collect assuming design cooling performance. The remainder of the data will be collected in a third year of BES-II.

**Table 4: Scenario 2** - Run 20 assuming nineteen cryo-weeks of running, including five weeks of LEReC commissioning, and two weeks of cool-down/set-up time.<sup>1</sup>

Single-Beam Energy (GeV/n)	$\sqrt{s_{NN}}$ (GeV)	Run Time	Species	Events	Priority	Sequence Spring 2020
4.55	9.1	9.5 weeks	Au+Au	160M	1	1
4.55	3.2 (FXT)	2 days	Au+Au	100M	2	2
5.75	3.5 (FXT)	2 days	Au+Au	100M	3	3
7.3	3.9 (FXT)	2 days	Au+Au	100M	3	4
19.5	6.2 (FXT)	2 days	Au+Au	100M	3	5
13.5	5.2 (FXT)	2 days	Au+Au	100M	3	6
3.85	3.0 (FXT)	2 days	Au+Au	100M	4	7

<sup>1</sup> The BES-II request includes an 11.5 GeV and 7.7 GeV run which require 5 and 12 cryo-weeks, respectively. These data sets will need to be collected in a third year of BES-II.

**Table 5: Scenario 3** - combined Fall '19 run with five cryo-weeks from Run 19 and nine cryo-weeks from Run 20 assuming twenty-four cryo-weeks of running, including five weeks of LEReC commissioning, and two weeks of cool-down/set-up time. Followed by a Spring '20 run of the remaining thirteen cryo-weeks.<sup>1</sup>

Single-Beam Energy (GeV/n)	$\sqrt{s_{NN}}$ (GeV)	Run Time	Species	Events	Priority	Sequence Fall 2019
5.75	11.5	5 weeks	Au+Au	230M	1	1
5.75	3.5 (FXT)	2 days	Au+Au	100M	2	2
19.5	6.2 (FXT)	2 days	Au+Au	100M	3	3
13.5	5.2 (FXT)	2 days	Au+Au	100M	3	4
3.85	3.0 (FXT)	2 days	Au+Au	100M	4	5
						Spring 2020
4.55	9.1	9.5 weeks	Au+Au	160M	1	1
4.55	3.2 (FXT)	2 days	Au+Au	100M	2	2

<sup>1</sup> The BES-II request includes a 7.7 GeV run which requires 12 cryo-weeks. This data set will need to be collected in a third year of BES-II.

**Table 6: Scenario 4** - combined Fall '19 run with five cryo-weeks from Run 19 and eight cryo-weeks from Run 20 assuming nineteen cryo-weeks of running, including five weeks of LEReC commissioning, and two weeks of cool-down/set-up time. Followed by a Fall '20 run which combines the remaining eleven cryo-weeks with those of a third year of BES-II<sup>1</sup>

Single-Beam Energy (GeV/n)	$\sqrt{s_{NN}}$ (GeV)	Run Time	Species	Events	Priority	Sequence Fall 2019
5.75	11.5	5 weeks	Au+Au	230M	1	1
5.75	3.5 (FXT)	2 days	Au+Au	100M	2	2
19.5	6.2 (FXT)	2 days	Au+Au	100M	3	3
13.5	5.2 (FXT)	2 days	Au+Au	100M	3	4
3.85	3.0 (FXT)	2 days	Au+Au	100M	4	5
						Fall 2020
4.55	9.1	9.5 weeks	Au+Au	160M	1	1
4.55	3.2 (FXT)	2 days	Au+Au	100M	2	2

<sup>1</sup> The BES-II request includes a 7.7 GeV run which requires 12 cryo-weeks. This data set will also need to be collected in a third year of BES-II, extending into Spring '21.

# Contents

<b>1</b>	<b>Highlights from the STAR Program</b>	<b>1</b>
1.1	Cold QCD & Spin Highlights . . . . .	1
1.1.1	Transverse Spin Program . . . . .	1
1.1.2	Longitudinal Spin Program . . . . .	4
1.1.3	Update on 2017 Data Analysis . . . . .	6
1.2	Heavy Ion Highlights . . . . .	8
1.2.1	Open Heavy flavor . . . . .	8
1.2.2	Quarkonia . . . . .	12
1.2.3	Beam Energy Scan - Phase I . . . . .	13
1.2.4	Bulk Correlations . . . . .	14
1.2.5	Jet Measurements . . . . .	21
<b>2</b>	<b>Proposal for Beam Energy Scan Phase 2</b>	<b>22</b>
2.1	Search for the First-Order Phase Boundary: Measurement of Baryon Directed Flow . . . . .	23
2.2	Global Polarization and Future Measurement of the Transient Magnetic Field During Heavy-Ion Collisions . . . . .	27
2.3	Disappearance of the Chiral Magnetic Effect (CME) in Low-Energy Au+Au Collisions . . . . .	28
2.4	Dilepton Measurements and Search for Chiral Symmetry Restoration . . . . .	30
2.5	Onset of Deconfinement: the Disappearance of QGP Signatures . . . . .	34
2.5.1	Elliptic Flow $v_2$ of $\phi$ Meson . . . . .	34
2.5.2	Nuclear Modification Factor $R_{CP}$ . . . . .	36
2.6	Higher Moments and the Search for the QCD Critical Point . . . . .	38
<b>3</b>	<b>Proposal for Fixed Target Program</b>	<b>41</b>
3.1	Motivation for the FXT Program . . . . .	41
3.2	FXT Test Runs . . . . .	42
3.3	FXT Physics Program . . . . .	44
3.4	FXT Beam Request . . . . .	46
<b>4</b>	<b>Detector Upgrades for Runs 19 and 20</b>	<b>48</b>
4.1	iTPC Upgrade . . . . .	48
4.2	EPD Upgrade . . . . .	52
4.3	eTOF Upgrade . . . . .	56

# 1 Highlights from the STAR Program

## 1.1 Cold QCD & Spin Highlights

The STAR spin physics program seeks to advance our understanding of the spin and flavor structure of the proton in terms of its constituent quarks and gluons, exploiting the unique capability of RHIC to provide longitudinally and transversely polarized  $p + p$  collisions at multiple collision energies. Using longitudinally polarized beams, one can probe the helicity preferences of the gluons and of up and down (anti-)quarks, to determine the contribution of each to the total spin of the proton. With spins transverse to their momentum direction, the  $pp$  collisions exhibit kinematic and dynamical effects that are directly sensitive to quark transversity and partonic motion within the proton. This program is complemented by studies of polarized  $pp$  elastic scattering and central exclusive production, in which a far-forward proton is detected intact.

Since 2009 RHIC STAR has completed several highly successful polarized  $pp$  runs both at  $\sqrt{s} = 200$  GeV and  $\sqrt{s} = 510$  GeV. The STAR sampled luminosity and the luminosity averaged beam polarization as measured by the hydrogen jet (H-jet) polarimeter are summarized in Table 7. These data sets formed the basis for papers and new preliminary results, which are highlighted in the following sections.

Year	$\sqrt{s}$ (GeV)	Recorded Luminosity ( $\text{pb}^{-1}$ )	Spin Orientation	B/Y $\langle P \rangle$
2009	200	25	Longitudinal	55
2009	500	10	Longitudinal	39
2011	500	12	Longitudinal	48
2011	500	25	Transverse	48
2012	200	22	Transverse	61/56
2012	510	82	Longitudinal	50/53
2013	510	300	Longitudinal	51/52
2015	200	52	Transverse	53/57
2015	200	52	Longitudinal	53/57
2017	510	320	Transverse	55

**Table 7:** Summary of  $pp$  running periods at RHIC since 2009, including center-of-mass energy, integrated luminosity collected at STAR and the average beam polarizations for blue (B) and yellow (Y) beams from the H-jet polarimeter. Years with a single polarization value indicate both beams were running at the same average value.

### 1.1.1 Transverse Spin Program

Since last year’s PAC meeting, the STAR spin and cold QCD physics working group has published two papers focused on transverse spin, one in Physical Review D [4] and the other in Physics Letters B [5]. Both analyses present complementary results from the  $\sqrt{s} = 500$  GeV

data collected in 2011. Because of the large center-of-mass energy delivered by RHIC, the results presented by STAR in these papers cover a completely different kinematic region than semi-inclusive deep inelastic scattering (SIDIS) experiments that target the same physics [6, 7, 8]. Particularly, STAR is able to probe a range in  $x$  similar to SIDIS coverage, but at much higher values of  $Q^2$ . Figure 1 presents a summary of the STAR kinematic coverage for the results presented in this section.

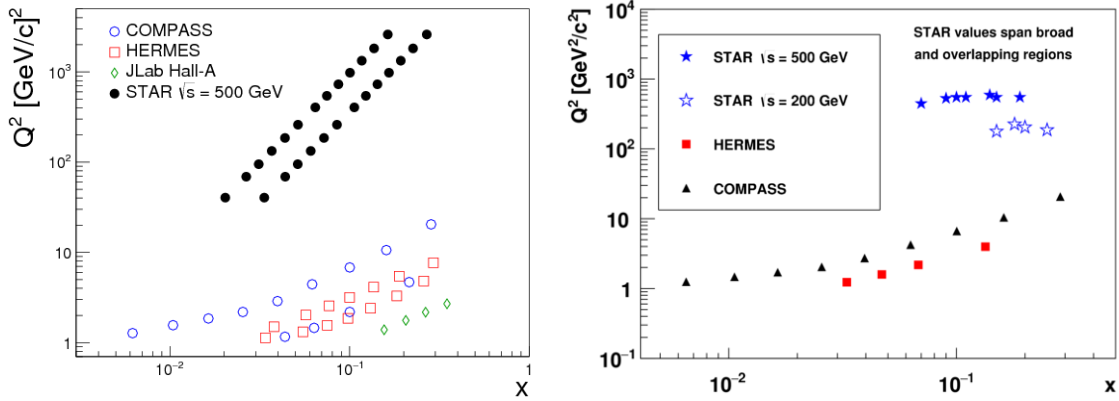


**Figure 1:** STAR kinematic coverage for the Collins [4] (left) and interference fragmentation function (IFF) [5] (right) analyses. Notice these results cover a very different region than SIDIS results [6, 7, 8] which target the same physics.

STAR has the ability to measure the Interference Fragmentation Function (IFF) and Collins asymmetries simultaneously. These asymmetries correlate the initial state transverse quark spin to the final state azimuthal distribution of hadron pairs [9, 10, 11] and hadrons in a jet [12], respectively. Hence, both asymmetries access the quark transversity distribution through totally different channels. This opens the door to study universality for transversity and the fragmentation functions using in-house comparisons between STAR results and comparing our results to similar analyses coming from SIDIS and  $e^+e^-$ . Because of the different range of  $Q^2$ , STAR is also in an excellent position to give necessary input to help theorists better understand the evolution of these distributions. The IFF channel is described by the collinear factorization where both the fragmentation function and transversity distribution integrate over any transverse momentum dependence. This contrasts the Collins channel where the fragmentation function carries a built in transverse momentum dependence to describe final state hadronic motion, and is therefore described with the transverse momentum dependent (TMD) factorization. The collinear factorization is understood quite well and is readily applicable to hadronic collisions, however there are lingering questions about whether or not the TMD factorization is broken in hadronic collisions. Input from STAR can help our understanding of the TMD factorization in hadronic collisions.

Figure 2 shows the Collins asymmetry measured as a function of pion  $z = p_\pi/p_{jet}$  in

$\sqrt{s} = 500$  GeV collisions, plotted over the top of model calculations [13, 14], and represents the first observation of Collins asymmetries in hadronic collisions. Assuming factorization isn't broken for this hadronic Collins channel, these models calculate the asymmetry using the transversity distribution and fragmentation functions extracted from global analyses of SIDIS and  $e^+e^-$  results. Note that the KPRY-NLL [14] model assumes TMD evolution, while the other models assume no evolution. The STAR results match up quite well with these model calculations. Within the error budget of this result, we observe no effects of factorization breaking for the Collins channel in hadronic collisions. Furthermore, the good agreement with the models, whether or not TMD evolution is included, points to a slow evolution with  $Q^2$ .

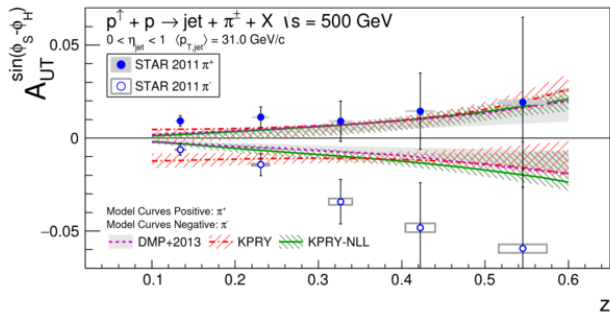


**Figure 2:** This asymmetry, measured in  $\sqrt{s} = 500$  GeV collisions, is the first statistically significant Collins asymmetry measured in hadronic collisions. The results are plotted over the top of model calculations which use distributions from global analyses of SIDIS and  $e^+e^-$ .

The  $\sqrt{s} = 500$  GeV IFF result is shown in Figure 3, and is compared to both model predictions [15] as well as the previous IFF result measured in  $\sqrt{s} = 200$  GeV collisions [16]. The results from the two datasets are compared in the same kinematic regime, thus the expectation is that they match each other very well. The 200 GeV and 500 GeV results do agree quite well with each other, and they both agree well with the theory model calculation which also uses transversity and the IFF extracted from global analyses of SIDIS and  $e^+e^-$  data. This great agreement with the model again points to a slow evolution with  $Q^2$ .

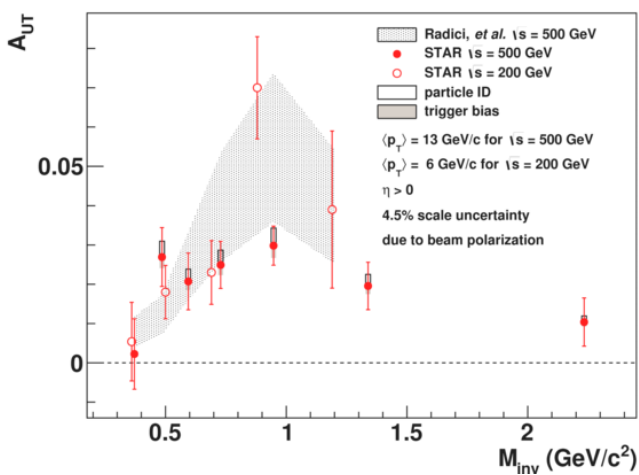


**Figure 3:** The IFF asymmetry measured in  $\sqrt{s} = 500$  GeV collisions. When the same kinematics are sampled, the asymmetries from the 200 GeV and 500 GeV analyses agree quite well. Systematic errors due to pion sample purity (particle ID) and trigger bias are shown as white and grey bands, respectively. A 4.5% scale uncertainty due to errors in the polarization measurements is not included in the systematic errors, but is common to each asymmetry point.

A channel similar to the Collins channel, dubbed the Collins-like asymmetry, is sensitive

to the linearly polarized gluons inside of a transversely polarized proton, and a fragmentation function that describes the azimuthal distribution of hadrons in a jet which result from these gluons. STAR has the ability to measure the Collins-like asymmetry, with the result shown in Figure 4. Gluons dominate the proton at low values of jet  $p_T$ , hence the best sensitivity would be found there. As a function of jet  $p_T$ , there is no observed significant asymmetry, even when charge states are combined for maximum statistical precision. The results are shown over the top of the shaded maximized projections [13]. This result from STAR is the first measurement of the Collins-like asymmetry and will give excellent input to help constrain these maximized projections.

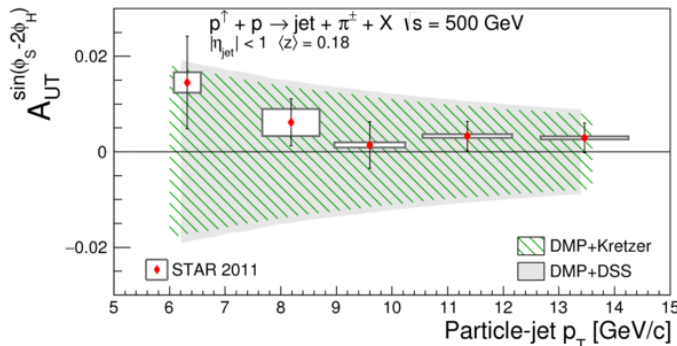


**Figure 4:** The Collins-like asymmetry measured in  $\sqrt{s} = 500$  GeV collisions. This channel is sensitive to linearly polarized gluons, hence the largest effect is expected at lower values of jet  $p_T$ .

Ref. [4] also reports results on the single spin inclusive jet asymmetry that is sensitive to initial state twist-3 quark-gluon correlation functions, which are related to the leading twist TMD Sivers function. Consistent with previous results released by STAR at  $\sqrt{s} = 200$  GeV [17], there is no observed asymmetry at  $\sqrt{s} = 500$  GeV. However, the measured asymmetries will give input to help better constrain the twist-3 functions, with an emphasis on stronger gluonic subprocesses.

### 1.1.2 Longitudinal Spin Program

STAR has released two preliminary results focused on longitudinal spin [18, 19], and submitted two papers to Physical Review D [20, 21]. These analyses are aimed at providing additional constraints to the gluon helicity parton distribution function,  $\Delta g(x, Q^2)$ . Longitudinal double spin asymmetry ( $A_{LL}$ ) analyses using inclusive jets and dijets are two ways STAR can gain access to  $\Delta g(x, Q^2)$ . While inclusive jets maximize the precision of the available statistics, the underlying partonic kinematics, such as momentum fractions, are integrated together in the results which is not favorable for theoretical extractions of the total integral  $\Delta G(Q^2)$ . On the other hand, dijet analyses are able to reconstruct information about the underlying partonic kinematics, however requiring two jets for a dijet event leads to decreased statistical precision when compared to an inclusive jet analysis. Over the past year, one inclusive jet  $A_{LL}$  result and two dijet  $A_{LL}$  results have been released.

Figures 5 and 6 show the preliminary results of  $A_{LL}$  using inclusive jets and preliminary dijet  $A_{LL}$  measured at midrapidity ( $|\eta| < 0.9$ ) from the 2013  $\sqrt{s} = 510$  GeV dataset released last year at the RHIC and AGS User's Meeting. The inclusive  $A_{LL}$  result agrees very

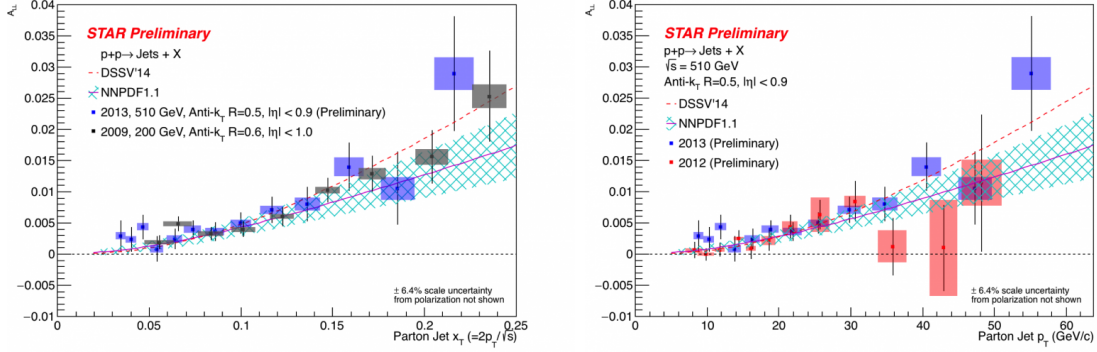


**Figure 5:** 2013  $\sqrt{s} = 510$  GeV STAR preliminary inclusive jet  $A_{LL}$  plotted as a function of  $x_T = 2p_T/\sqrt{s}$  along side the 2009 result from  $\sqrt{s} = 200$  GeV (left) and plotted as a function of parton level jet  $p_T$  along side the 2012  $\sqrt{s} = 500$  GeV preliminary result from 2012. In both cases the results agree well with each other and also with the provided theory curves.

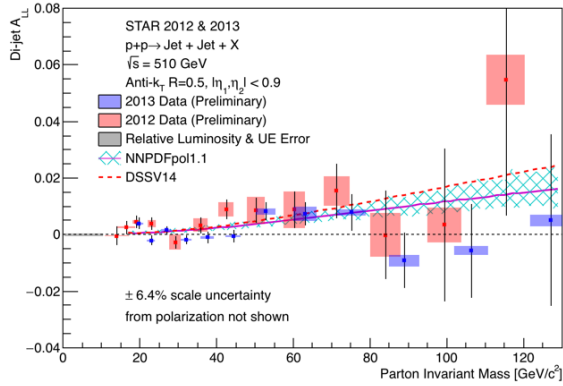


**Figure 6:** STAR preliminary dijet  $A_{LL}$  at  $\sqrt{s} = 510$  GeV for 2013 (blue) and 2012 (red) plotted as a function of  $M$ , which is proportional to the products of the momentum fractions of the partons in the hard scattering. These results are compared to theory predictions from the DSSV [22] and NNPDF [23] groups.

well with both the 2009  $\sqrt{s} = 200$  GeV result where the kinematics overlap, and the 2012  $\sqrt{s} = 500$  GeV result. This result will contribute necessary additional data that will help to further constrain  $\Delta g(x, Q^2)$ . The dijet  $A_{LL}$  is plotted as a function of the invariant mass,  $M$ , which is directly proportional to the product of the momentum fractions of the partons in the hard scattering. The results agree very well with the previous 2012  $\sqrt{s} = 510$  GeV result and with the theory predictions from DSSV [22] and NNPDF [23] groups. This result will also help place constraints on  $\Delta g(x, Q^2)$ , but in a more known and narrow range of  $x$  than the inclusive jet result.

Where the two 2013  $\sqrt{s} = 510$  GeV  $A_{LL}$  results were both measured at midrapidity, a new result from STAR takes advantage of the endcap electromagnetic calorimeter to increase this range in pseudorapidity, and require for the first time ever that one jet in the dijet lie in the range  $0.8 < \eta < 1.8$ . This will shift the  $x$  coverage down from the analysis at midrapidity. The endcap dijet  $A_{LL}$  measured from the 2009  $\sqrt{s} = 200$  GeV data is shown in Figure 7.

The data agree within statistics in the top two panels where one jet lies at midrapidity in the barrel electromagnetic calorimeter and the other lies in the endcap with the theory curves from the DSSV [22] and NNPDF [23] groups. However, when both jets in the dijet lie forward in the endcap, the data diverge significantly from the theory predictions. This is also the case where the lowest value of  $x$  is sampled over a very narrow range. These data will provide constraints at very low values of  $x$  for  $\Delta g(x, Q^2)$  where the distribution is still very unconstrained.

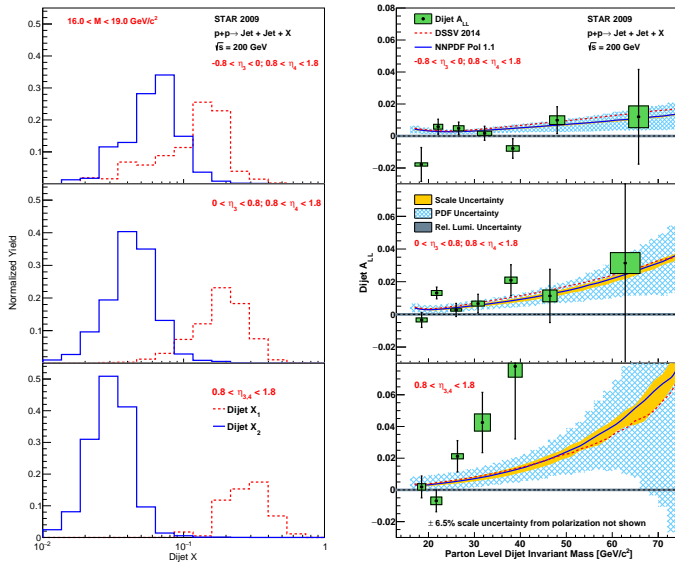


**Figure 7:** STAR endcap dijet kinematic coverage (left) and  $A_{LL}$  (right) at  $\sqrt{s} = 200$  GeV from the 2009 dataset [20]. Here,  $x_1$  and  $x_2$  represent the momentum fractions of the partons which participate in the hard scattering,  $\eta_3$  and  $\eta_4$  represent the pseudorapidity of the final state jets resulting from the partons. Using  $\eta_3$  and  $\eta_4$ , jets may be sorted into different topological arrangements, as presented here. The lowest value of  $x$  is probed when both jets lie in the endcap (bottom panel). The solid yellow and blue hatched bands represent errors on the NNPDF model calculations of  $A_{LL}$ .

It is possible to push the kinematic coverage to even smaller values of  $x$ , but to do so the measurements must go farther forward, such as with the forward meson spectrometer (FMS). In addition to using jets,  $A_{LL}$  may be measured by reconstructing  $\pi^0$ s and looking at the difference in yield when the proton helicities are aligned versus anti-aligned. STAR has measured this asymmetry in the forward region ( $2.65 < \eta < 3.9$ ) using  $\sqrt{s} = 510$  GeV data collected during the 2012 and 2013 runs. Figure 8 shows the results of this work, and within the current statistical precision the  $\pi^0$   $A_{LL}$  results are consistent with the theory predictions resulting from global analyses by the DSSV [22] and NNPDF [23] groups. This analysis pushes the kinematic coverage for  $\Delta g(x, Q^2)$  down to  $x \sim 0.001$ , which is well below the coverage from the inclusive jet and dijet analyses. Therefore STAR is able to provide input for  $\Delta g(x, Q^2)$  global analyses across a broad range of very small  $x$  values where the distribution is still largely unconstrained.

### 1.1.3 Update on 2017 Data Analysis

Currently, work is underway to perform a calibration of the FMS and its components. Figure 9 is from the fast offline production, and provides a first look into the performance of the FMS and post-shower (FPOST) components. The FPOST has two orthogonal layers of

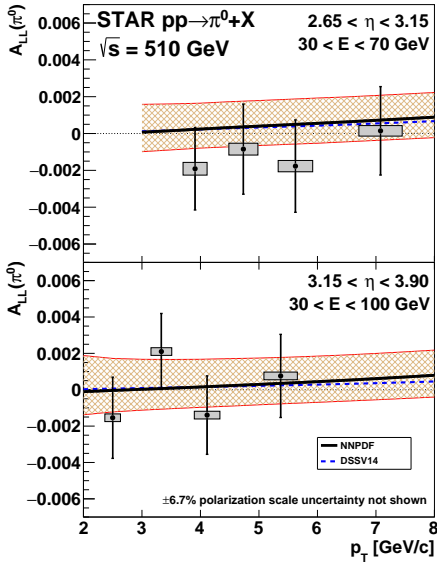


**Figure 8:** STAR  $\pi^0$   $A_{LL}$  at  $\sqrt{s} = 510$  GeV from the 2012 and 2013 RHIC runs. Particles this far forward are produced when a high- $x$  parton strikes a very low- $x$  parton pushing it back toward the FMS [21]. Hence, larger values of  $\eta$  will sample smaller values of the momentum fraction,  $x$ . Therefore, the results in the bottom panel here will push the  $x$  coverage lower than the result presented in the top panel. These results are compared to theoretical model predictions using results from the DSSV [22] and NNPDF [23] groups.

scintillator slats with an additional diagonal layer to reduce ambiguities for leakage of high energy showers out of the back end of the FMS. The left plot in Figure 9 shows the alignment between reconstructed points in the FMS ( $x$ -axis) and one of the layers ( $y$ -axis) of the FPOST. An upper energy cut of 2 GeV is used here to enhance the fraction of hadrons that will punch through the calorimeter. The increased activity towards the lower left is near the beam pipe where electromagnetic showers can leak out the side of the FMS. The right plot in Figure 9 is an example of an ADC spectrum from one FPOST channel to illustrate the location of the minimum ionizing particle (MIP) signal above the pedestal with a fit to a Landau function. In addition to the calibration effort, monitoring of pedestal width and location of the MIP peak throughout the 2017 RHIC run can also be used to study the radiation damage from low energy neutrons to the silicon photomultiplier sensors, in particular in the high luminosity environment of  $\sqrt{s} = 500$  GeV proton collisions.

Additionally, data from the transverse polarized  $pp$  collisions at  $\sqrt{s} = 510$  GeV is used to extract the  $A_N$  for  $W$  production, Drell-Yan, and direct photons. These measurements are sensitive to the Sivers function, one of the  $p_T$  dependent parton distribution functions, which is predicted to have opposite sign in  $pp$  collisions from that observed in deep inelastic lepton-proton scattering. STAR performed an exploratory measurement of  $W$   $A_N$  with a small data set taken in 2011 [24]. The 2017 data set will allow for a definitive answer of the sign change and/or provide new insights in thus far unknown evolution effects. Its analysis is currently in progress.

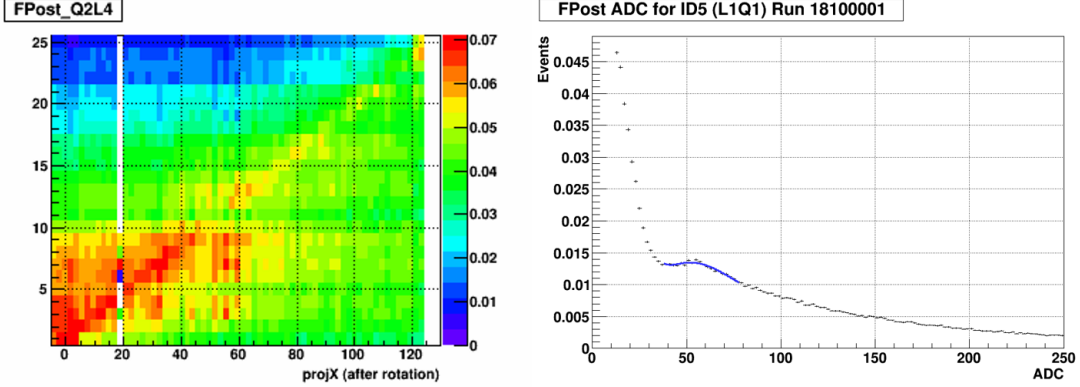


**Figure 9:** A look into the ongoing FMS calibration. The left plot shows the alignment between reconstructed points in the FMS (x-axis) and one layer of the post-shower detector (y-axis). The right plot is an example ADC spectrum from one post-shower channel, with an included Landau fit to the MIP signal above pedestal.

## 1.2 Heavy Ion Highlights

A prominent physics goal of RHIC runs since 2014 has been to study QGP matter with heavy flavor probes (open charm and bottom, quarkonia etc.) utilizing the two mid-rapidity detector upgrades — the Heavy Flavor Tracker (HFT) and the Muon Telescope Detector (MTD). The HFT aims for precise measurements of charmed hadron production in heavy-ion collisions, with particular emphasis on low  $p_T$  coverage. It also offers the capability to probe open bottom production through decay daughters. The MTD is designed to measure Upsilon production in heavy-ion collisions via the dimuon channel in order to allow the separation of Upsilon( $2S + 3S$ ) from Upsilon( $1S$ ) states.

### 1.2.1 Open Heavy flavor

The first measurement of  $D^0$  meson elliptic flow from the HFT detector was published last year in Phys. Rev. Lett. [25]. The result shows that  $D^0$  meson  $v_2$  follows the same number-of-constituent-quark (NCQ) scaling when plotted as a function of transverse kinetic energy ( $m_T - m_0$ ) in mid-central Au+Au collisions at  $\sqrt{s_{NN}} = 200$  GeV. The  $D^0$   $v_2$  can also be described by a viscous hydro model calculation. These results suggest that charm quarks interact with the medium strongly and gain a significant amount of elliptic flow, similar to other light hadrons.

Figure 10 shows the  $D^0$  meson nuclear modification factor  $R_{CP}$  in several different centrality bins compared to other light and strange hadrons at  $\sqrt{s_{NN}} = 200$  GeV measured with the HFT. The reference used here is the  $D^0$  spectrum measured in the 40–60% centrality bin. The precision reported here is significantly improved in comparison with STAR’s previous measurement with the TPC only. The  $R_{CP}$  of  $D^0$  mesons at  $p_T > 4$  GeV/ $c$  in central 0–10% Au+Au collisions is significantly suppressed, and is comparable to that of other light hadrons, re-affirming that charm quarks suffer a large amount of energy loss in the hot QCD

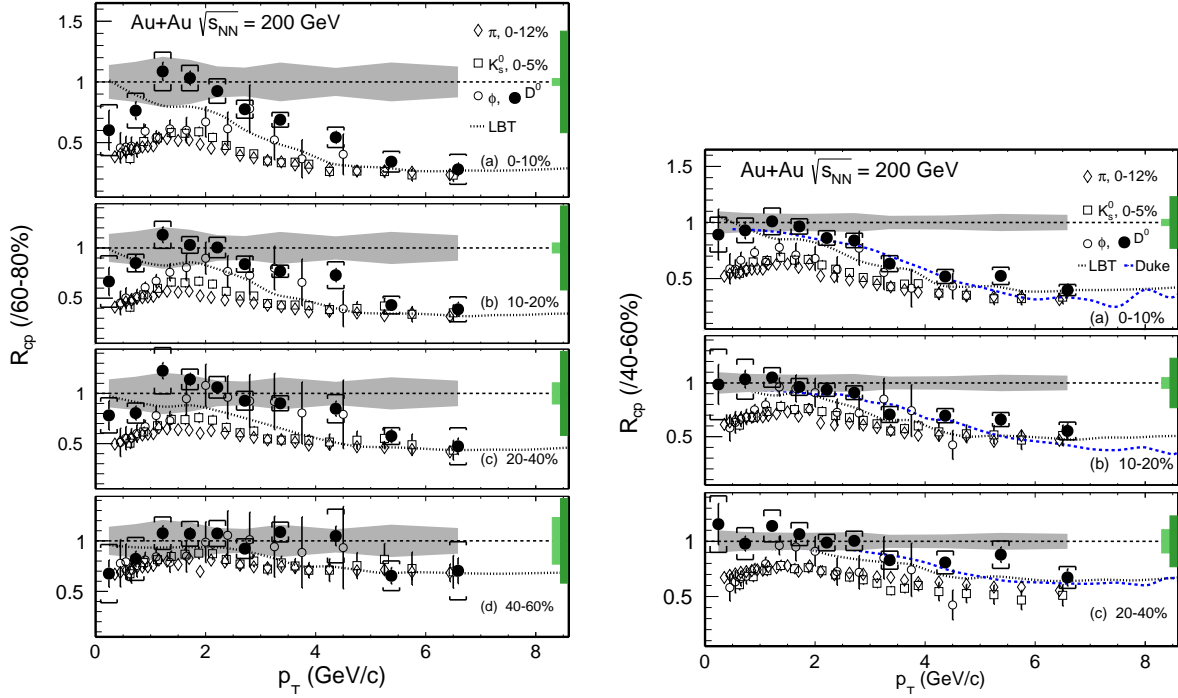


**Figure 10:**  $D^0$ -meson nuclear modification factor  $R_{CP}$  for seven centrality bins in Au+Au collisions at  $\sqrt{s_{NN}} = 200$  GeV. Results are compared with light strange hadrons as well as with model calculations.

medium. The suppression level shows a smooth centrality dependence. The  $R_{CP}$  at low  $p_T$  is higher than that of light hadrons and shows a characteristic bump structure, consistent with the model-motivated expectation that charm quarks gain sizable collectivity during the medium evolution.

Charm quark hadronization via coalescence can lead to an enhancement in the  $D_s^+$  and  $\Lambda_c$  baryon production in heavy-ion collisions. At the Quark Matter 17 conference STAR reported the  $D_s^+/D^0$  ratio and observed an enhancement in central and mid-central Au+Au collisions with respect to the fragmentation baseline from PYTHIA, as shown in Fig. 11. The enhancement is also higher than the latest model predictions from the TAMU and the Catania groups. Figure 12 shows the measured  $\Lambda_c/D^0$  ratio in Au+Au collisions compared to other light hadron baryon-to-meson results in Au+Au collisions. The data point shows a significant enhancement compared to the PYTHIA model calculation. The  $\Lambda_c/D^0$  value is compared to those of light and strange baryon-to-meson ratios and is compatible with a few theoretical model calculations involving hadronization via charm quark coalescence.

Since the QM 2017 conference, analysis of  $D_s$  and  $\Lambda_c$  hadron production has focused on two main improvements: a) applying a supervised training method for topological reconstruction to improve the signal significance; b) utilizing the new dataset collected during the 2016 run. Figure 13 shows the reconstructed  $\Lambda_c$  signal in the 10–80% centrality bin, based on 1.3 billion Au+Au minimum-bias events collected in the 2016 run. The statistics used here

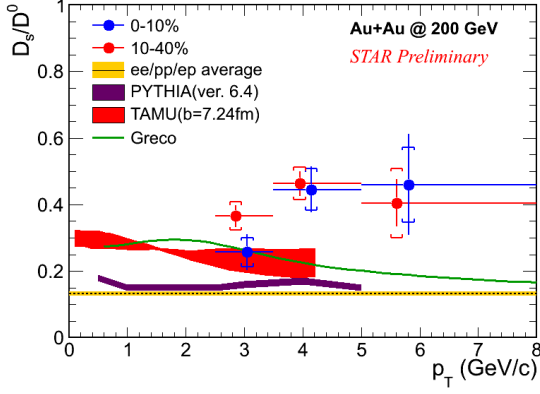


**Figure 11:** The  $D_s^+/D^0$  ratio as a function of  $p_T$  in central and mid-central Au+Au collisions at  $\sqrt{s_{NN}} = 200$  GeV compared with fragmentation baselines from world-average data and with PYTHIA as well as two dynamical model calculations.

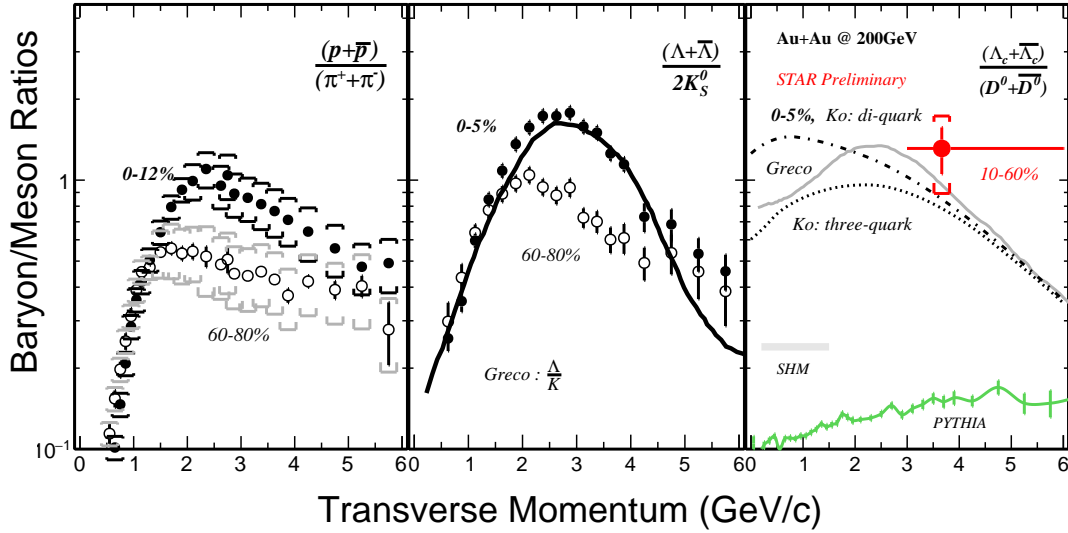


**Figure 12:** STAR measurements of baryon-to-meson ratios for light (left), strange (middle) and charm (right) hadrons in Au+Au collisions at  $\sqrt{s_{NN}} = 200$  GeV. The new  $\Lambda_c/D^0$  data are compared to several model predictions.

correspond to  $\sim 75\%$  of the total recorded data in 2016. The new supervised training method has been successfully applied to the reconstruction of various charm hadrons. The improved signal significance allows us to study the centrality and  $p_T$  dependence of  $\Lambda_c$  production, and the new results are planned to be reported at the 2018 Quark Matter conference.

Measurements of  $D^0 v_2$  and  $R_{CP}$  indicate that charm quarks are strongly coupled with the medium. We have also extended the  $D^0$  measurement to  $D^+$  and  $D^{*+}$  mesons. Study of their production will offer complementary information about the in-medium dynamics of charm quarks. Figure 14 shows the reconstructed raw signals of  $D^{+/-}$  candidates from the  $D^{*+} \rightarrow K^- \pi^+ \pi^+$  channel (left panel) and  $D^{*+}$  candidates from the  $D^{*+} \rightarrow D^0 \pi^+ \rightarrow K^- \pi^+ \pi^+$  channel (right panel) in Au+Au collisions at  $\sqrt{s_{NN}} = 200$  GeV. Analysis of these measurements in both the 2014 and 2016 datasets is ongoing, and these results, combined with  $D^0$  measurements, are expected to offer more insights on the in-medium interactions of

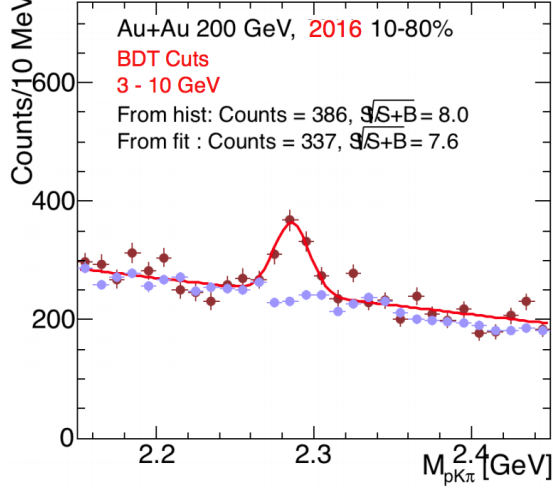


**Figure 13:** Reconstructed  $\Lambda_c$  signal in the 10–80% centrality bin, based on 1.3 billion Au+Au minimum-bias events collected in the 2016 run.

charm quarks.

STAR will have the capability to measure all the charmed hadrons  $D^0$ ,  $D^+$ ,  $D^{*+}$ ,  $D_s^+$  and  $\Lambda_c^+$  in the same experiment, which will allow us to constrain the total charm production cross section in heavy-ion collisions. Combining the Au+Au datasets recorded in the 2014 and 2016 runs will offer measurements of unprecedented precision, and new results are expected at the 2018 QM conference.

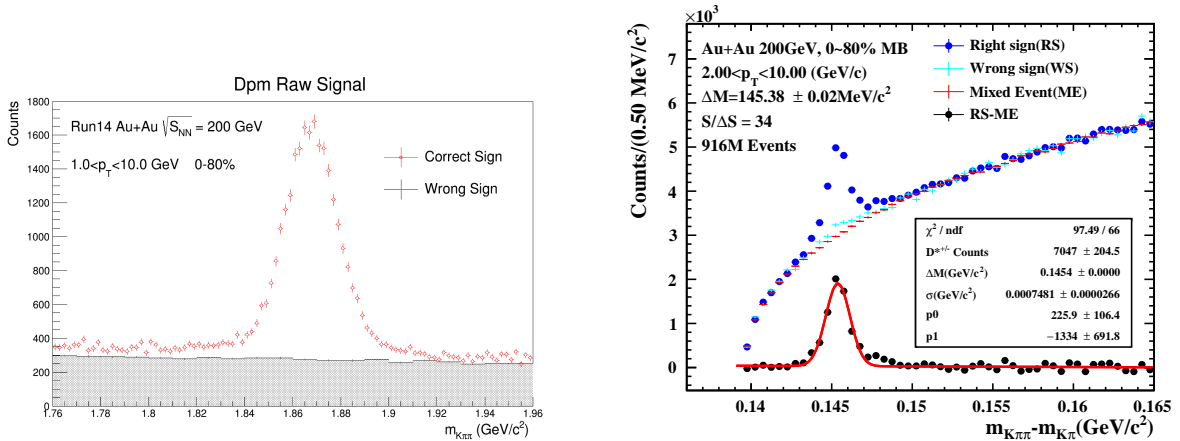


**Figure 14:**  $D^+$  (left) and  $D^{*+}$  (right) raw signals reconstructed via  $K^+K^-\pi^+$  and  $D^0 + \pi^+$  channels, respectively, in Au+Au collisions at  $\sqrt{s_{NN}} = 200$  GeV.

Combining the full Au+Au statistics together with the first-order event plane from the ZDC-SMD, STAR can carry out the first measurement of  $D^0/\bar{D}^0$   $v_1$  at RHIC energies. The  $D^0$   $v_1$  is expected to be sensitive to the longitudinal structure of the QGP medium, according to model calculations [26]. Furthermore, it is predicted that the difference in  $v_1$  between  $D^0$  and  $\bar{D}^0$  mesons is highly sensitive to the early-stage magnetic field created in these collision [Das:2016c wd]. The  $D^0/\bar{D}^0$   $v_1$  measurements are underway and the results

will be reported soon.

Measurements in Run 15  $pp$  and  $p$ +Au, and Run 16 d+Au data taken with the HFT are expected to provide useful references for open heavy flavor measurements in Au+Au collisions. Offline production for these datasets has been completed. Analysis of open charm hadron production in small systems has been carried out, and we expect to report physics results in the near future.

### 1.2.2 Quarkonia

Figure 15, left plot, shows the preliminary result for the  $J/\psi$  polarization parameter  $\lambda_\theta$  measured in the helicity frame in  $pp$  collisions at  $\sqrt{s} = 200$  GeV through dielectron (2012 data) and dimuon (2015 MTD data) channels, compared to previously published STAR and PHENIX results. The  $J/\psi$  polarization parameters are measured also in the Collins-Soper frame via the dimuon channel. Both  $\lambda_\theta$  and  $\lambda_\phi$  parameters are consistent with zero in both frames. The right plot shows the nuclear modification factor for inclusive  $J/\psi$  in  $p$ +Au collisions compared to various model calculations. The result is similar to that measured in d+Au collisions and favors an additional nuclear absorption effect on top of the nuclear PDF effect.

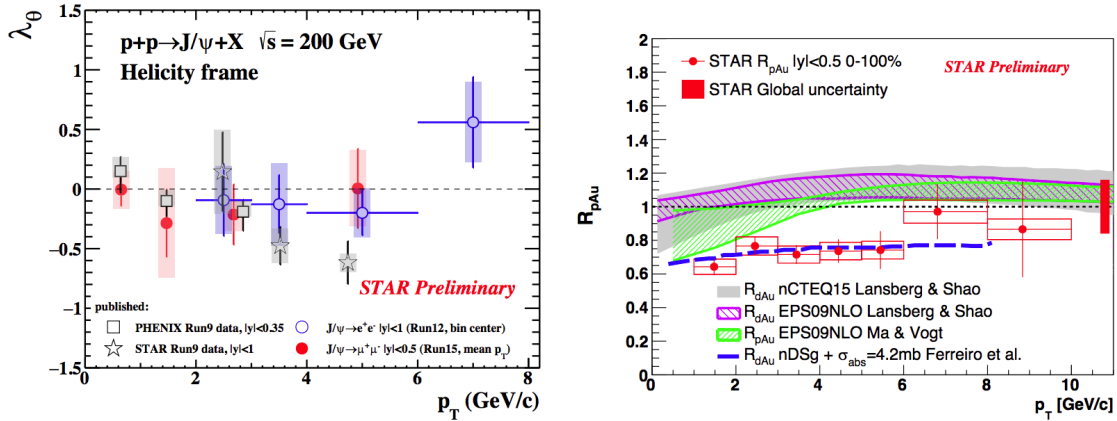


**Figure 15:** Left: The  $J/\psi$  polarization parameter  $\lambda_\theta$  measured in the helicity frame in  $pp$  collisions at  $\sqrt{s} = 200$  GeV through dielectron and dimuon channels, compared to previously published STAR and PHENIX results. Right:  $J/\psi$   $R_{pAu}$  measured from the dimuon channel as a function of  $p_T$  at mid-rapidity compared to various model calculations.

$\Upsilon$  production in Au+Au collisions at  $\sqrt{s_{NN}} = 200$  GeV is measured in the dielectron and dimuon channels from BEMC- and MTD-triggered data in 2011 and 2014. The combined results on  $\Upsilon R_{AA}$  for the  $(1S)$  state (left) and the  $(2S + 3S)$  states (right) as a function of centrality are shown in Fig. 16. The left plot shows that the  $\Upsilon(1S)$  state is clearly suppressed in central Au+Au collisions, and the suppression level is similar to that measured at 2.76 TeV by CMS. The right plot shows the first  $\Upsilon(2S + 3S)$   $R_{AA}$  from STAR and the  $\Upsilon(2S)$ ,  $\Upsilon(3S)$ , and  $R_{AA}$  measurements from CMS. The results are consistent for the most central collisions,

but there is a hint of less suppression at RHIC in mid-centrality classes. Furthermore,  $\Upsilon(2S + 3S)$  shows a stronger suppression in the most central collisions at RHIC, consistent with the sequential melting phenomenon.

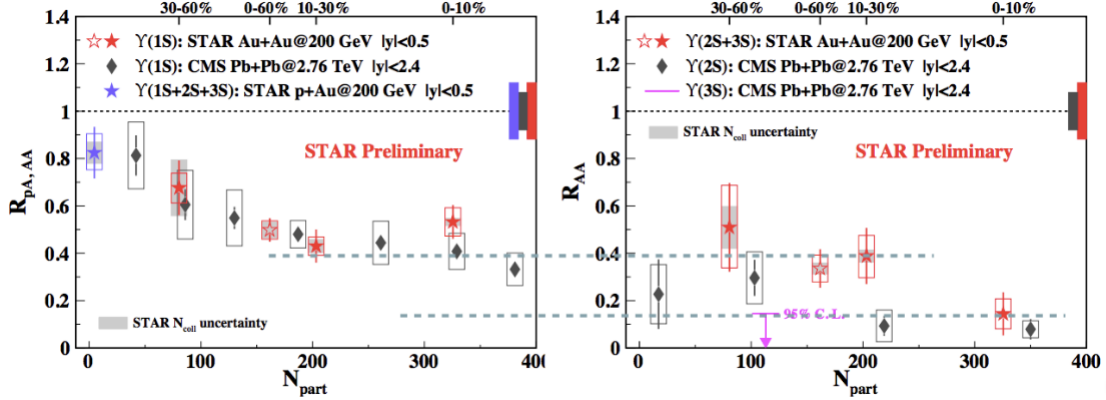


**Figure 16:**  $\Upsilon(1S)$   $R_{AA}$  (left) and  $\Upsilon(2S + 3S)$   $R_{AA}$  (right) as a function of centrality in  $p+Au$  and  $Au+Au$  collisions at 200 GeV from STAR compared to CMS measurements at 2.76 TeV.

Another significant set of MTD data was recorded in the 2016 run. Analysis of  $\Upsilon$  production in this dataset is underway. Figure 17 shows the combined  $\Upsilon$  raw signal from 2014 ( $14 \text{ nb}^{-1}$ ) and 2016 ( $13 \text{ nb}^{-1}$ ) runs at  $\sqrt{s_{NN}} = 200 \text{ GeV}$ . The new  $R_{AA}$  result for various  $\Upsilon$  states is on track to be released at the 2018 Quark Matter conference.

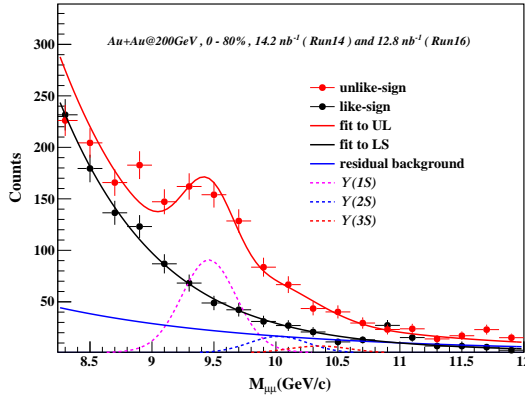


**Figure 17:**  $\Upsilon$  raw signal combining 2014 and 2016 MTD data, corresponding to  $27 \text{ nb}^{-1}$   $Au+Au$  collision data at  $\sqrt{s_{NN}} = 200 \text{ GeV}$ .

### 1.2.3 Beam Energy Scan - Phase I

In the 2014 run, STAR took  $Au+Au$  data at  $\sqrt{s_{NN}} = 14.5 \text{ GeV}$ , thereby completing the BES-I program. In this section, we highlight a few recent publications from this program.

In 2018, STAR published a PRL on the measurement of identified particle directed flow ( $v_1$ ), extending the analyzed species to strange hadrons ( $\Lambda, \bar{\Lambda}, K^\pm, K_s^0$  and  $\phi$ ) [27]. The

slopes  $dv_1/dy$  near mid-rapidity as a function of beam energy for  $\Lambda$ s agree with those of protons, and change sign near 11.5 GeV. Antiprotons,  $\bar{\Lambda}$ , kaons and pions have negative  $dv_1/dy$  throughout the studied energy range. A new facet of the analysis that was first reported at CPOD in summer 2017, and is included in Ref. [27], is a  $v_1$ -related investigation of constituent quark coalescence versus beam energy, exploiting a different but complementary approach compared with the familiar NCQ scaling of elliptic flow versus transverse mass; refer to subsection 2.1 for further details.

STAR recently submitted to PRL a paper on the beam energy dependence of jet quenching. The high- $p_T$  net suppression in central Au+Au collisions at top RHIC energy for charged hadrons evolves smoothly to a large net enhancement at lower energies. Figure 18 shows the binary-collision-scaled high- $p_T$  yield as a function of centrality for various collision energies in two  $p_T$  bins: 3.0–3.5 GeV/ $c$  and 4.0–4.5 GeV/ $c$ . The data reveal an interesting non-monotonic shape in the energy region around 14.5–19.6 GeV/ $c$ . Note that many other non-monotonic behaviors are also observed around roughly the same energy region: proton and net-proton  $v_1(y)$  slope, the high-moment product of kurtosis times variance, multiplicity-scaled  $v_3$ , etc. These interesting observations certainly deserve more systematic investigations, which we are planning to conduct in the BES-II program.

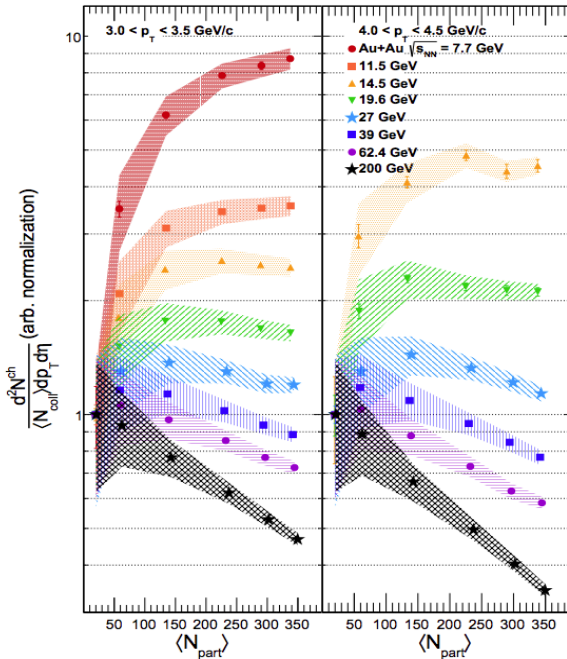


**Figure 18:** The binary-collision-scaled high- $p_T$  yield as a function of centrality for various collision energies. The left and right panels show the scaled yields in two  $p_T$  bins: 3.0–3.5 GeV/ $c$  and 4.0–4.5 GeV/ $c$ , respectively.

## 1.2.4 Bulk Correlations

### *System Size Dependence of Anisotropic Flow*

The collectivity in small systems such  $pp$  and  $p(d)+A$  is of great interest in searching for possible creation of QGP droplets, and it is important to study the onset of QGP not only as the collision energy is scanned, but also as the system size is varied. Azimuthal anisotropic

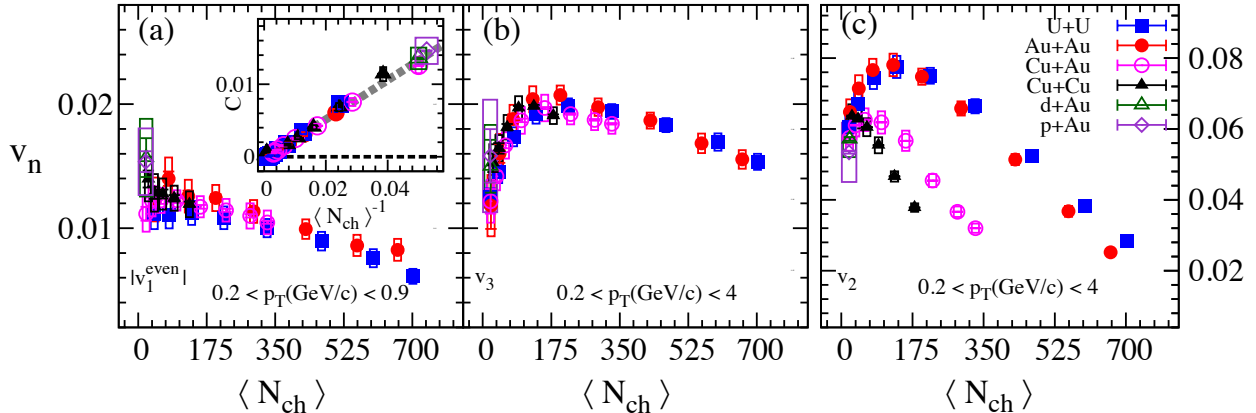


**Figure 19:** Magnitude of  $v_1^{\text{even}}$  (left),  $v_3$  (middle), and  $v_2$  (right) as a function of mean multiplicity of charged particles  $\langle N_{\text{ch}} \rangle$ .

flow coefficients  $v_n$  can be used to study the collectivity of the system, as extensively studied in A+A collisions [28].

STAR has studied  $v_n$  anisotropy coefficients via two-particle correlations for six collision systems:  $p$ +Au,  $d$ +Au,  $\text{Cu}+\text{Cu}$ ,  $\text{Cu}+\text{Au}$ , and  $\text{Au}+\text{Au}$  at  $\sqrt{s_{NN}}=200$  GeV and  $\text{U}+\text{U}$  at  $\sqrt{s_{NN}}=193$  GeV. Figure 19(a) shows dipole flow ( $v_1^{\text{even}}$ ) which originates from density asymmetry in the initial state, with elliptic ( $v_2$ ) flow in panel (c) and triangular ( $v_3$ ) flow in panel (b) for all the above systems as a function of the number of charged particles measured in  $|\eta| < 0.5$ , denoted  $\langle N_{\text{ch}} \rangle$ . The  $v_1^{\text{even}}$  and  $v_3$  for all the systems, including  $p$ +Au and  $d$ +Au, fall on the same curve at any given multiplicity, supporting the picture where the signal originates from initial-state density fluctuations.

Elliptic flow  $v_2$  exhibits system dependence as illustrated in Fig. 20(left). This dependence can be understood in terms of different initial eccentricities for each collision system at a given  $\langle N_{\text{ch}} \rangle$ . Scaled  $v_2$ , using the initial eccentricity  $\varepsilon_2$  calculated by a Monte-Carlo Glauber simulation in the denominator, is plotted as a function of  $\langle N_{\text{ch}} \rangle^{-1/3}$  in Fig. 20(left), where  $\langle N_{\text{ch}} \rangle^{-1/3}$  is in inverse proportion to a geometric radius of the system. Results for all the systems fall on the same curve, which suggests a similar collective behavior among the systems.

In small systems, or low-multiplicity events, non-flow contributions such as back-to-back jets and resonance decays become dominant compared to high-multiplicity events in A+A collisions. Therefore it is important to reduce these non-flow contributions in the measurements. STAR checked such contributions via the measurement of four-particle cumulants  $c_2\{4\}$  using the three-sub method [29, 30], which significantly suppresses non-flow, as shown in Fig. 20(right). For a given multiplicity in A+A(A') and  $d$ +Au collisions,  $c_2\{4\}$  shows negative values, which are required at least to claim collectivity by definition ( $v_2\{4\} = (-c_2\{4\})^{-1/4}$ ).

### Longitudinal Flow Decorrelation

Density fluctuations in the initial state followed by the space-time evolution process of the

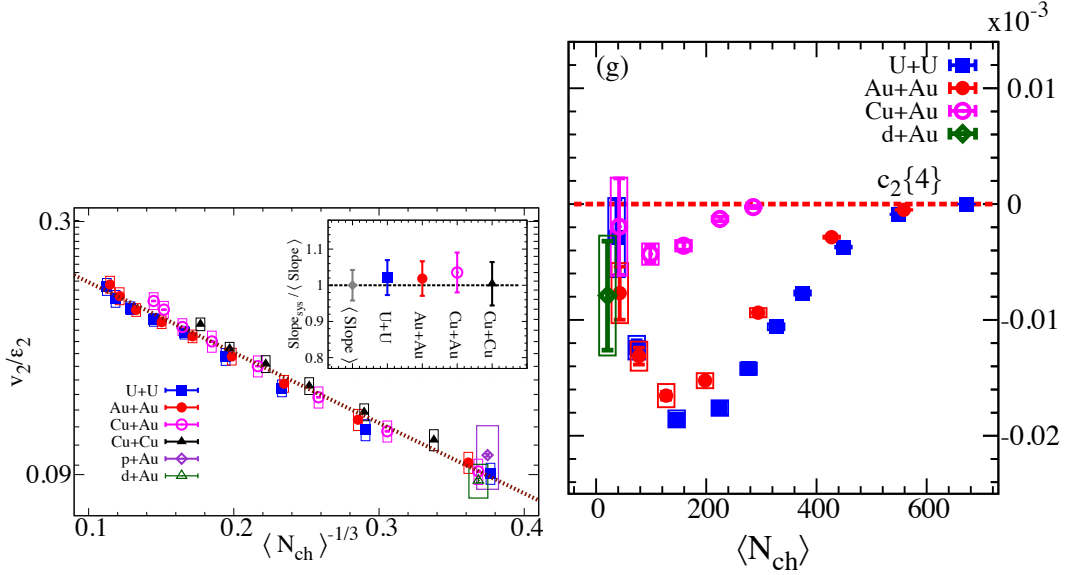


**Figure 20:** Elliptic flow  $v_2$  scaled by the initial eccentricity  $\epsilon_2$  as a function of  $\langle N_{ch} \rangle^{-1/3}$  (left), and the 4-particle cumulant  $c_2\{4\}$  as a function of  $\langle N_{ch} \rangle$  (right).

collision lead to correlations of produced particles in momentum space in both transverse and longitudinal directions. Studies of azimuthal anisotropy coefficients  $v_n$  at mid-rapidity provide important constraints on the transport properties of the medium, e.g., the shear viscosity over entropy density [31]. On the other hand, the longitudinal structure of the initial state is not well understood, especially at lower energies. Study of two-particle correlations along the rapidity direction would help for further understanding of the initial state and for improving (3+1)D modeling of heavy-ion collisions.

STAR has measured the flow decorrelation along the longitudinal direction, for the first time at RHIC energy,  $\sqrt{s_{NN}} = 200$  GeV. The decorrelation observable  $r_n$  is defined as  $r_n(\eta_a) = V_{n\Delta}(-\eta_a, \eta^{\text{ref}}) / V_{n\Delta}(\eta_a, \eta^{\text{ref}})$  where  $V_{n\Delta} = \langle \langle \cos(n\phi^a - n\phi^{\text{ref}}) \rangle \rangle$ . The quantity  $\eta^{\text{ref}}$  denotes the reference pseudorapidity window. In this study, the  $\eta_a$  for particles of interest was taken from within the TPC acceptance ( $|\eta| < 1$ ) and the  $\eta^{\text{ref}}$  was taken from the Forward Meson Spectrometer (FMS,  $2.5 < \eta < 4.0$ ) installed at STAR prior to the year 2015. The FMS allows us to remove the effect of short-range non-flow correlations. If there is no decorrelation,  $r_n$  should be 1.0.

Figure 21 shows  $r_n$  as a function of pseudorapidity, including a comparison to results at LHC energies [32]. Our results clearly show a flow decorrelation for both elliptic and triangular flow, indicating the breaking of boost-invariance over the relevant  $\eta$  window. The results at RHIC show stronger decorrelation than that at the LHC and (3+1)D ideal hydrodynamic calculations [33] overestimate the magnitude of the data at RHIC for both  $v_2$  and  $v_3$ . For further understanding of energy dependence, studies for lower energies are ongoing.

### *Polarization from Vorticity*

The system created in non-central heavy ion collisions has large angular momentum carried

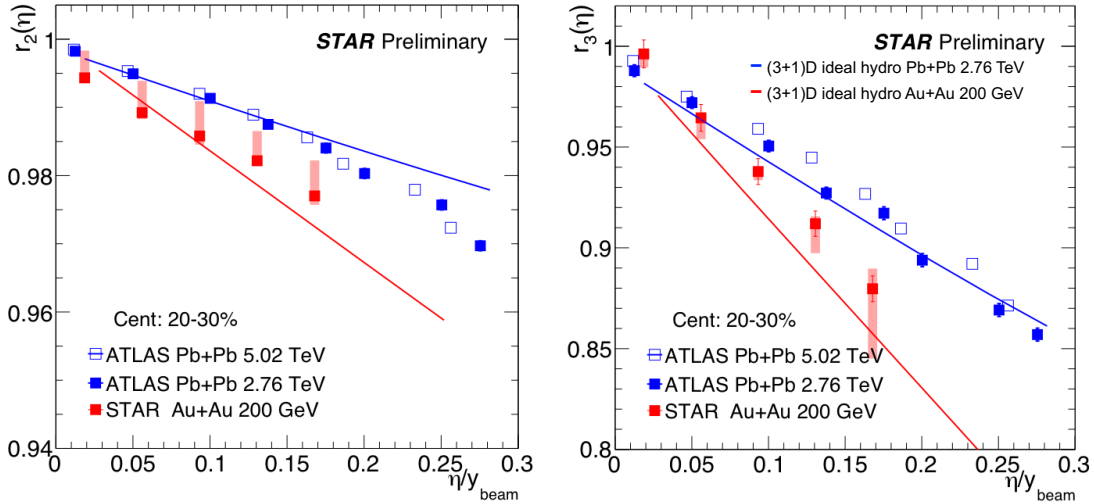


**Figure 21:** Flow decorrelation measure  $r_2$  and  $r_3$  as a function of pseudorapidity normalized by the beam rapidity, compared to results for Pb+Pb collisions at  $\sqrt{s_{NN}} = 2.76$  and 5.02 TeV from ATLAS [32] and (3+1)D ideal hydrodynamic model calculations [33].

by the two colliding nuclei, of the order of  $\sim 10^3 \hbar$ , which may result in a strong vortical structure of the system [34, 35]. Due to spin-orbit coupling, this initial angular momentum might be transferred to the spin degree of freedom and lead to global polarization of produced particles. Such a global polarization can be measured experimentally with hyperons via parity-violating weak decays in which the daughter baryon is preferentially emitted into the direction of the hyperon spin, and using our knowledge of the direction of the angular momentum based on the first-order event plane. Further details of these BES-I highlights can be found in the BES-II proposal subsection dealing with this measurement topic: 2.2.

We also found that new preliminary results for  $\sqrt{s_{NN}} = 200$  GeV, using year 2014 data combining with 2010 and 2011 data, show a non-zero positive signal for the polarization, which follows the global trend of the energy dependence. The results are in good agreement with expectations from viscous hydrodynamic models [36] and a multi-phase transport (AMPT) model [37]. These new 200 GeV results have been announced to RHIC and are on track for journal submission in May 2018. These results further support the discovery reported in *Nature* in August 2017 [38], indicating that the system behaves as the most vortical fluid that has been ever observed, with vorticity on the order of  $\sim 10^{22} \text{ s}^{-1}$  (for  $T = 160$  MeV).

Another way to search for a signal of the vorticity is to measure a spin alignment of vector mesons. The decay angular distribution of a vector meson is parameterized by the spin density matrices  $\rho$ . A deviation of the diagonal elements  $\rho_{mm}$  ( $m = -1, 0, 1$ ) from  $1/3$  signals a net spin alignment. Since vector mesons decay strongly, the elements  $\rho_{-1-1}$  and

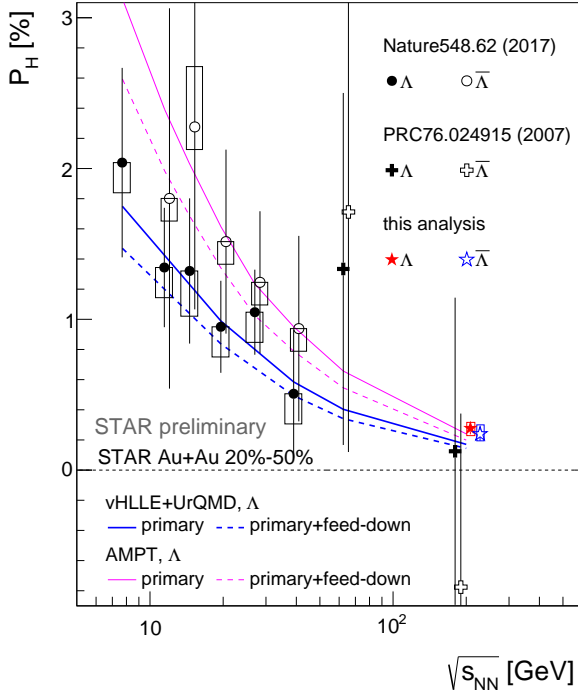


**Figure 22:** Global polarization of  $\Lambda$  hyperons for 20-50% central Au+Au collisions as a function of collision energy. Bold lines show calculations from the hydrodynamic model [36] and thin lines are from the AMPT model [37]; solid lines are for primary  $\Lambda$ s and dashed lines for all  $\Lambda$ s including the feed-down effect.

$\rho_{11}$  are degenerate and  $\rho_{00}$  is the only independent observable. Figure 23 shows  $\rho_{00}$  of  $\phi$  mesons measured with respect to the first-order event plane as a function of collision energy for 20-60% central Au+Au collisions. For higher energies, results show a deviation from  $1/3$ , indicating spin alignment due to the vorticity. Results with the second-order event plane, which is less correlated with the initial angular momentum, are also in agreement with results based on the first-order event plane within current uncertainties.

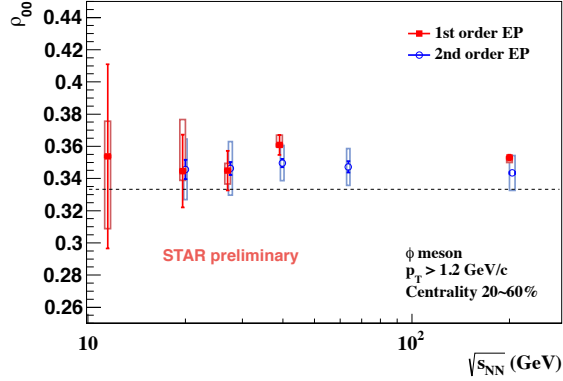


**Figure 23:** The spin density matrix  $\rho_{00}$  of  $\phi$  mesons with respect to the first- and second-order event planes for 20-60% central Au+Au collisions as a function of collision energy.

### Chiral Magnetic Effect

The chiral magnetic effect (CME) refers to the induction of an electric current  $\vec{J}_e$  by the magnetic field  $\vec{B}$  in a chiral system:  $\vec{J}_e \propto \mu_5 \vec{B}$ . A chiral system bears a nonzero  $\mu_5$ , which characterizes the imbalance of right-handed and left-handed fermions in the system. The

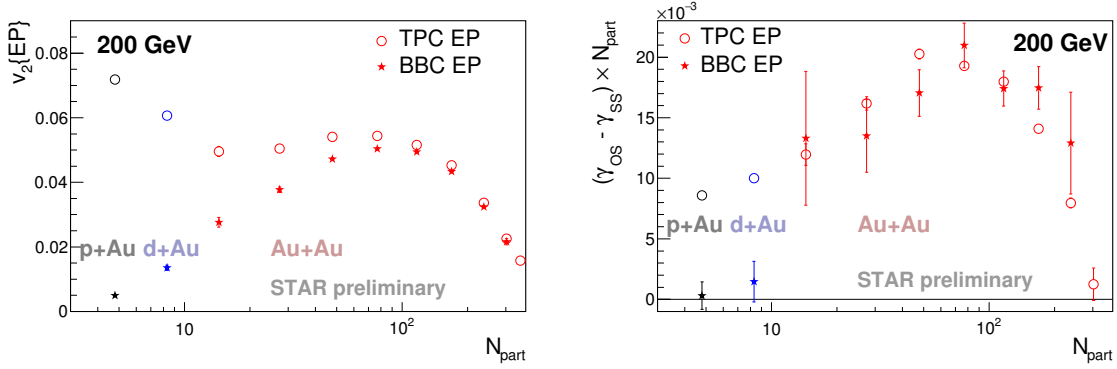


**Figure 24:**  $v_2$  (left) and  $\Delta\gamma \times N_{\text{part}}$  (right) vs  $N_{\text{part}}$  for  $p$ +Au,  $d$ +Au, and Au+Au collisions at 200 GeV, measured using event planes from both TPC and BBC detectors.

discovery of the CME in high-energy heavy-ion collisions would confirm the simultaneous existence of ultra-strong magnetic fields, chiral symmetry restoration and topological charge-changing transitions in these collisions. On average,  $\vec{B}$  is perpendicular to the reaction plane ( $\Psi_{\text{RP}}$ ) that contains the impact parameter vector and the beam momenta. Hence the CME will manifest itself through a charge transport across the reaction plane.

Experimentally, the CME has been searched for via charge-separation fluctuations perpendicular to the reaction plane, e.g., with a three-point correlator  $\gamma \equiv \langle \cos(\phi_\alpha + \phi_\beta - 2\Psi_{\text{RP}}) \rangle$  where the averaging is done over all particles in an event and over all events. The expansion of the  $\gamma$  correlator,

$$\langle \cos(\phi_\alpha + \phi_\beta - 2\Psi_{\text{RP}}) \rangle = \langle \cos \Delta\phi_\alpha \cos \Delta\phi_\beta - \sin \Delta\phi_\alpha \sin \Delta\phi_\beta \rangle, \quad (1)$$

$$= (\langle v_{1,\alpha} v_{1,\beta} \rangle + B_{\text{IN}}) - (\langle a_{1,\alpha} a_{1,\beta} \rangle + B_{\text{OUT}}), \quad (2)$$

reveals the difference between the in-plane and out-of-plane projections of the correlations. The first term  $\langle v_{1,\alpha} v_{1,\beta} \rangle$  in the expansion provides a baseline unrelated to the magnetic field. The term  $\langle a_{1,\alpha} a_{1,\beta} \rangle$  quantifies the electric charge separation due to the CME. The background contribution ( $B_{\text{IN}} - B_{\text{OUT}}$ ) is largely canceled out, however it could be non-zero and contribute to the  $\gamma$  correlator. We take the difference in the  $\gamma$  correlators between like-sign and unlike-sign pairs for particle  $\alpha$  and  $\beta$  to reduce the background, although there would still be a non-negligible effect of the background due to resonance decays, jets, and different emission between in-plane and out-of-plane.

Recently, CMS reported the  $\gamma$  correlators for  $p$ +Pb and Pb+Pb collisions at  $\sqrt{s_{NN}} = 5.02$  TeV, showing very similar behavior in both systems [39, 40]. Since  $\Psi_2$  shows little correlation with the direction of the magnetic field in  $p$ +A collisions [41], the CMS finding indicates that the observed  $\gamma$  correlator at the LHC is dominated by the background, however there are expected to be several differences in the system at the LHC compared to RHIC e.g., a shorter lifetime of the magnetic field and a larger non-flow contribution. STAR performed systematic studies of non-flow effects in small systems, specifically  $p$ +Au (Run 15) and  $d$ +Au (Run 16). Figure 24 shows  $v_2$  (left) and  $\Delta\gamma \times N_{\text{part}}$  (right) for  $p$ +Au,  $d$ +Au and Au+Au

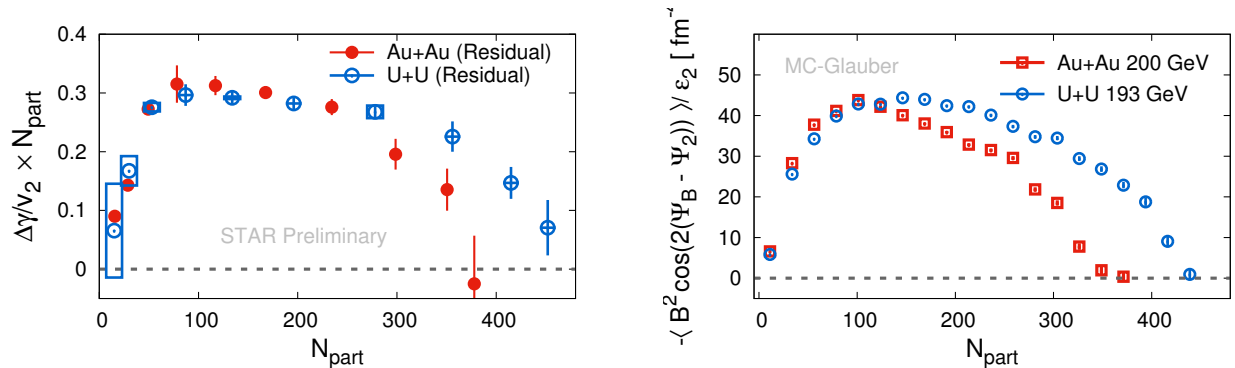


**Figure 25:**  $\Delta\gamma/v_2 \times N_{\text{part}}$  vs  $N_{\text{part}}$  (left) and the magnetic field projection onto the second-order event plane divided by the initial ellipticity (right) for 200 GeV Au+Au and 193 GeV U+U collisions. Positive short-range correlations have been removed from the  $\gamma$  measurements in the left panel.

collisions at 200 GeV, measured using event planes from both TPC and BBC. Using the TPC event plane,  $v_2$  displays an enhancement at small values of  $N_{\text{part}}$ , demonstrating the short-range non-flow contributions, whereas with the BBC event plane, a pseudorapidity gap of at least 2.8 units is introduced between the event plane and the particles of interest, and  $v_2$  goes down monotonically with decreasing  $N_{\text{part}}$ . Likewise,  $\Delta\gamma \times N_{\text{part}}$  measured for  $p$ +Au stops at a sizable positive value using the TPC event plane, and diminishes using the BBC event plane. The disappearance of the charge separation observable in  $p$ +Au is in line with the idea that the magnetic field direction and the second-order participant plane ( $\Psi_2$ ) are so decoupled that no CME signal should be observed with  $\Psi_2$  in  $p$ +Au.

Another test of the signal/background scenario has been carried out with the comparison of  $\Delta\gamma/v_2 \times N_{\text{part}}$  between 200 GeV Au+Au and 193 GeV U+U, as shown in Fig. 25 (left). Note that the  $\gamma$  measurements shown here have excluded the positive short-range correlations between particles  $\alpha$  and  $\beta$ , which are determined with a multi-component fit to the differential measurement of  $\gamma$  as a function of the pseudorapidity gap between particles  $\alpha$  and  $\beta$ . PHENIX has shown that at the same  $N_{\text{part}}$ , the multiplicity is almost identical for 200 GeV Au+Au and 193 GeV U+U [42], thus  $\Delta\gamma/v_2 \times N_{\text{part}}$  should be constant and almost the same for these two systems, according to the background scenario. Data show different rise-and-fall trends for Au+Au and U+U. The two trends merge at lower  $N_{\text{part}}$ , and separate from each other at higher  $N_{\text{part}}$ . These very features can be naturally explained by the magnetic field projection divided by ellipticity, as depicted in the right panel of Fig. 25. A uranium nucleus has 13 more protons than a gold nucleus, which in turn causes the difference in the magnetic fields in U+U and Au+Au collisions. The difference in the magnetic field is compensated by the difference in ellipticity at lower  $N_{\text{part}}$ , but becomes overwhelming towards higher  $N_{\text{part}}$ .

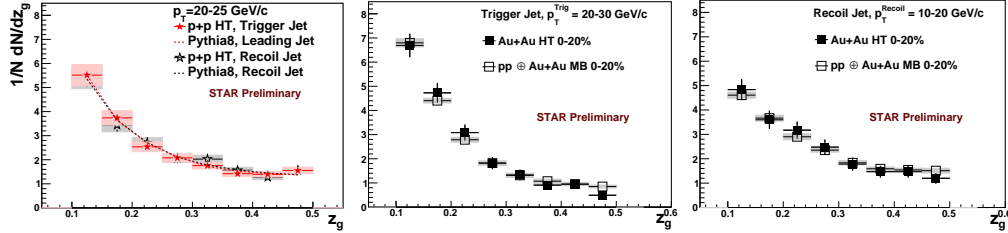


**Figure 26:** Left:  $z_g$  distributions for trigger (filled symbols) and recoil (open symbols) jets independently binned in  $p_T^{\text{part}}$  in  $pp$  HT compared to PYTHIA8 (dashed lines). Middle (Right):  $z_g$  in Au+Au HT (filled symbols) data and  $pp$  HT plus Au+Au MB (open symbols) for trigger (recoil) jets. Shaded bands indicate systematic uncertainty estimates due to the jet energy scale.

### 1.2.5 Jet Measurements

Jets are an important probe to study properties of the QGP. Measurement of dijet imbalance [43] and semi-inclusive hadron+jets [44] were recently published by STAR. In these studies, dijet pairs reconstructed from constituents with  $p_T > 2$  GeV/ $c$  are found to be significantly imbalanced in Au+Au collisions in comparison to the results from  $pp$  collisions. However, the lost energy is recovered in soft constituents ( $p_T > 0.2$  GeV/ $c$ ) with signs of broadening of the jet structure within a jet radius of  $R = 0.4$  [43]. This is consistent with the measurement of semi-inclusive hadron+jets, where the yield of jets recoiling from a high- $p_T$  trigger hadron is suppressed in central Au+Au collisions, corresponding to medium-induced energy transport to large angles relative to the jet axis of  $\sim 3 - 5$  GeV/ $c$  [44].

The internal structure of jets is studied via measurement of the Jet Splitting Function  $z_g = \frac{\min(p_{T,1}, p_{T,2})}{p_{T,1} + p_{T,2}}$  through the SoftDrop grooming process in  $pp$  and Au+Au collisions at  $\sqrt{s_{NN}} = 200$  GeV (Fig. 26). Modification of the  $z_g$  function is predicted in some energy loss models, and thus the measurement of  $z_g$  gives qualitative constraints for theoretical treatment. As can be seen in Fig. 26, the measured  $z_g$  for  $10 < p_T^{\text{part}} < 30$  GeV/ $c$  in  $pp$  collisions at 200 GeV are in good agreement with PYTHIA simulations. Here  $p_T^{\text{part}}$  is the jet  $p_T$  corrected to the particle level. In Au+Au collisions, di-jet pairs used in the previous momentum imbalance measurement [43] are used in the  $z_g$  measurement. It is found that within uncertainties, there are no signs of a modified Jet Splitting Function on the trigger or recoil sides of this di-jet selection, while in a similar study, the CMS collaboration at LHC energies reported modifications of the Jet Splitting Function. Also shown for the first time at QM2017 were studies of semi-inclusive recoil jets coincident with a high  $p_T$   $\pi^0$  and hadron correlations with respect to reconstructed di-jets. The  $\pi^0$ -jet distributions show agreement, within uncertainties, with the  $h^\pm$ +jet distributions. The novel jet measurements with larger statistics from Runs 14 and 16 are expected to allow precise comparisons with theoretical calculations, potentially revealing further details of partonic interactions with the medium.

## 2 Proposal for Beam Energy Scan Phase 2

In Run 19, STAR proposes to initiate BES-II. Specific details of the physics goals and required statistics at each energy are given below. In addition, STAR is proposing a fixed target program to allow access to energies below those possible at RHIC in collider mode.

**Table 8:** Event statistics (in millions) needed in BES-II for various observables. This table updates estimates originally documented in Ref. [45].

Collision Energy (GeV)	7.7	9.1	11.5	14.5	19.6
$\mu_B$ (MeV) in 0-5% central collisions	420	370	315	260	205
<b>Observables</b>					
$R_{CP}$ up to $p_T = 5$ GeV/ $c$	-		160	125	92
Elliptic Flow ( $\phi$ mesons)	80	120	160	160	320
Chiral Magnetic Effect	50	50	50	50	50
Directed Flow (protons)	20	30	35	45	50
Azimuthal Femtoscopy (protons)	35	40	50	65	80
Net-Proton Kurtosis	70	85	100	170	340
Dileptons	100	160	230	300	400
$>5\sigma$ Magnetic Field Significance	50	80	110	150	200
<b>Required Number of Events</b>	100	160	230	300	400

In 2014, the STAR Collaboration released a white paper [45] in which the status of the analysis results was summarized from the first phase of the Beam Energy Scan (BES-I) and a second phase dedicated to low-energy running was proposed. In the following years, this white paper was followed by several detector-upgrade proposals [46, 47, 48] which in anticipation of Phase-II significantly improve STAR’s capabilities in terms of acceptance, efficiency, and particle identification. At this time, the STAR collaboration has published 23 papers pertaining to beam energies at and below 39 GeV (one in Nature, 8 in PRL and 2 in PLB), has submitted 3, and has another 5 papers in advanced stages of preparation. The results contained in these publications, while spectacular in many ways, point to several unanswered questions of far-reaching importance.

A disappearance of QGP signatures was indeed seen in the breakdown of constituent quark scaling of elliptic flow at beam energies below 19.6 GeV, in the disappearance of high  $p_T$  suppression for energies near 27 GeV and below, and in the collapse of charge separation that is attributed to the Chiral Magnetic Effect below 11.5 GeV, to name a few. There still remains some uncertainty in the interpretation of these observations, *i.e.*, it can be a challenge to unambiguously distinguish between a scenario where QGP production itself disappears, and the alternative picture in which our sensitivity to a QGP signature fades away. Hints of a first-order phase transition are seen in directed flow for baryons and net baryons. The measured directed flow at intermediate centralities has moderately good statistical significance, but as will be detailed in the next subsection, comparisons with recent

models yield contradictory conclusions, and a clear physics interpretation requires both further theoretical development as well as constraints from more comprehensive measurements. Meanwhile, searches for critical point signatures in particle ratio fluctuations and in the analysis of higher moments (skewness and kurtosis) of the multiplicity distribution of conserved quantities remain inconclusive, but arguably the net-protons kurtosis shows a departure from a monotonic dependence on  $\sqrt{s_{NN}}$ , as expected in the presence of a critical point. These observations narrow-down the most promising region for future searches that will involve improved detectors and higher statistics.

The BES-II proposal requests high statistics (typically 20 times higher than BES-I), as set out in Table 8 for the BES-II beam energies currently envisaged. The searches for new physics will benefit substantially from a much larger rapidity acceptance, lower  $p_T$  thresholds, and improved  $dE/dx$  resolution, all provided by the iTPC upgrade — see [46] and Sect. 4.1. The endcap Time of Flight detector (eTOF) upgrade, [47] and Sect. 4.3, will enable particle identification at higher momenta in the extended rapidity coverage. The Event Plane Detector (EPD), [48] and Sect. 4.2, already fully implemented, allows the centrality and the event plane to be measured in the forward region. This offers, for example, several advantages for analyses involving collective flow, including reduced statistical errors in many cases, and also reduced systematic errors arising from non-flow.

In the next subsections, we describe the main goals of the proposed BES-II program.

## 2.1 Search for the First-Order Phase Boundary: Measurement of Baryon Directed Flow

Directed flow excitation functions have been proposed by theorists as promising observables of evidence for a first-order phase transition, based on hydrodynamic calculations [49, 50, 51]. Some early hydro models predicted a sharp minimum in directed flow versus beam energy, referred to in the theory literature as the “softest point collapse” of flow, and this collapse was not predicted unless a first-order phase transition was assumed [51].

Figure 27 (left panel) presents directed flow measured by STAR for net-protons in Au+Au collisions at intermediate centrality [52]. The plotted quantity is the slope of  $v_1(y)$  near mid-rapidity. Compared with proton flow, the net-proton flow has a contribution by constituent quarks transported from the initial nuclei that is enhanced relative to the contribution by quarks produced in the collision process. These properties of net-particle flow are elucidated by new measurements in STAR’s most recent paper on BES  $v_1$  [27], see below.

The panel on the right side of Fig. 27 presents the directed flow calculations from a recent implementation of the Jet AA Microscopic (JAM) transport model [53] with three options for the QCD equation of state (see caption). The JAM scenario with a first-order phase transition (red triangles) is qualitatively similar to an early three-fluid hydro prediction with a first-order phase transition [51], and also has a qualitative resemblance to the STAR measurements. However, the magnitude of directed flow from JAM is several times larger than STAR’s data, and the position of the minimum along the beam energy axis is about one-third that measured by STAR.

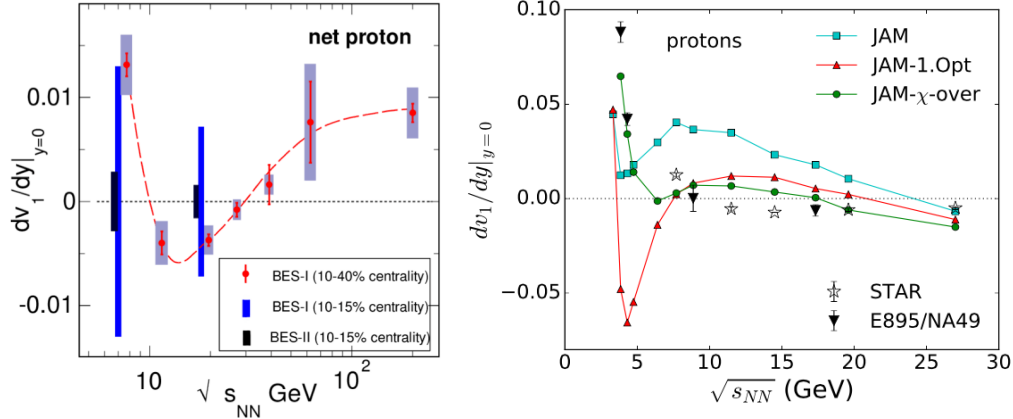


**Figure 27:** Left: Comparison of the published BES-I 10-40% centrality net-proton directed flow slope [52] with the BES-I error bar size for a much less populated centrality bin (10-15%), and with the expected BES-II error bar size in the same narrow centrality bin. Right: Directed flow slope from the JAM transport model [53]. The “JAM-1.Opt” in the legend denotes a first-order phase transition, and “JAM- $\chi$ -over” denotes a crossover, and the remaining option (green squares) involves a purely hadronic equation of state. Note the  $\sim 5$ -fold difference between the vertical scales of the two plots, and also note that below  $\sqrt{s_{NN}} \sim 15$  GeV, there is negligible difference between the definition of net-proton  $v_1$  (plotted on the left) and proton  $v_1$  (plotted on the right).

STAR’s 2014 BES  $v_1$  paper [52] prompted a series of comparisons with state-of-the-art models, based on hydrodynamics or Boltzmann-type transport or a hybrid of the two, all with realistic treatments of the QCD phases and the possible types of boundary between those phases [53, 54, 55, 56, 57, 58, 59]. Overall, these recent model calculations all confirm that directed flow at BES energies is quite sensitive to the assumed QCD equation of state and to the assumed type of phase transition between hadronic and QGP phases, and they all disfavor scenarios where only hadronic phases exist. On the other hand, agreement with data is quite poor for all assumed QCD equations of state in all models; no model scenario reproduces STAR’s observed minimum in proton directed flow in the relevant energy region and there is disagreement among different theory authors on whether a crossover or first-order phase transition is favored [60].

In particular, the authors of papers based on the JAM transport model [53, 58, 59] conclude that  $v_1$  comparisons tend to favor the EOS with a first-order phase transition. The authors of the Frankfurt hybrid model (which features Boltzmann transport for the early and late stages of the collision, and hydrodynamics for the intermediate hot and dense stage) conclude that overall agreement with proton  $v_1$  measurements is still too poor to draw conclusions about the preferred EOS [54]. Meanwhile, the authors of comparisons with the Parton-Hadron String Dynamics (PHSD) model [55] (a microscopic approach with equations of state constrained by lattice QCD) and with a relativistic 3-fluid hydrodynamic model (3FD) [57] report that the crossover EOS option is favored.

There is a close connection between the search for a first-order phase transition and

the search for a critical point. A confirmed observation of a first-order phase transition would imply that a critical point must exist, by ruling out a hypothesized scenario where the boundary between hadronic matter and QGP is a smooth crossover throughout the phase diagram as accessed by heavy-ion collisions. Such an observation would also have implications for the allowed and excluded locations in  $\mu_B$  of the critical point. While model comparisons to date have underlined the importance of further theoretical work in order to reach a confident interpretation, new experimental data are also essential for a definitive conclusion.

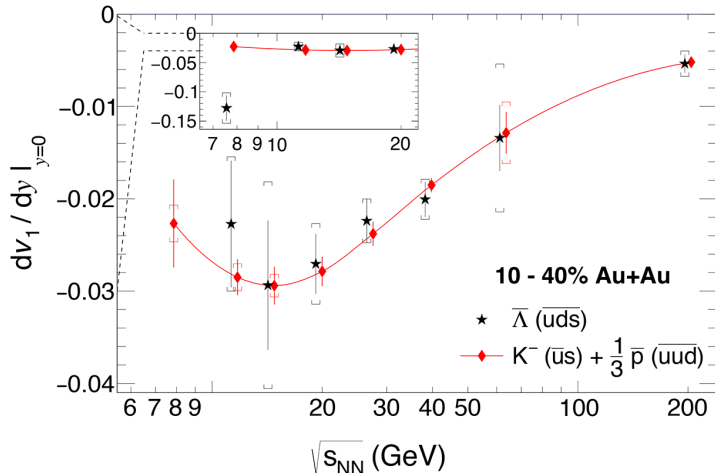


**Figure 28:** Collision energy dependence of the  $\Lambda$  directed flow slope  $(dv_1/dy)$  for intermediate centralities (10–40%) compared to the prediction of the coalescence sum rule for produced quarks. The inset shows the same comparison where the vertical scale is zoomed-out by a factor of 15 [27].

Because of the strong non-monotonic behavior observed for protons and net protons [52, 27], other baryon species like  $\Lambda$  hyperons [27] are of special interest, and will have excellent statistics in BES-II. In STAR’s 2018 paper on BES  $v_1$ , results for  $\Lambda$  and anti- $\Lambda$  have been particularly useful in probing quark coalescence behavior, as illustrated in Fig. 28. We now have a sufficient number of different particle species to test a set of assumptions: That  $v_1$  is imparted while quarks are deconfined, that specific types of quark have the same directed flow in the QGP phase, and that the detected hadrons form via statistical coalescence. In the limit of small azimuthal anisotropy coefficients  $v_n$ , statistical coalescence of deconfined quarks which have already acquired azimuthal anisotropy leads to the  $v_n$  of the resulting mesons or baryons being the summed  $v_n$  of their constituent quarks [61]. The familiar number-of-constituent-quark (NCQ) scaling follows from this coalescence behavior. The  $\bar{\Lambda}$  results in Fig. 28 are especially relevant for demonstrating that excellent agreement with a scaling pattern based on the three assumptions above is observed for  $\sqrt{s_{NN}} = 11.5$  to 200 GeV, while one or more of them breaks down at 7.7 GeV at the level of  $\sim 4.5\sigma$  (statistical). The enhanced statistics of BES-II will allow these patterns of quark-level behavior to be probed more accurately and for several additional species.

Although BES-I statistics are insufficient for a systematic study of the centrality dependence of directed flow, it is noteworthy that at low BES energies, proton  $v_1(y)$  magnitudes appear to increase by roughly a factor of 5 when going from intermediate centralities to more peripheral centralities. Normally, anisotropic flow coefficients exhibit far less central-

ity dependence over this range, and so this unusual pattern is highly deserving of targeted investigation in BES-II.

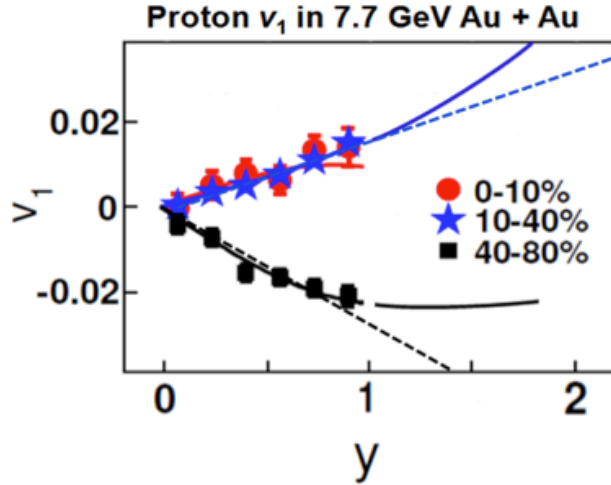


**Figure 29:** Plotted points show measured directed flow  $v_1(y)$  for protons in three centrality bins for Au+Au collisions at  $\sqrt{s_{NN}} = 7.7$  GeV. The solid curves are a cubic fit to the measured data points for intermediate and peripheral centralities while the dashed lines are linear fits. To improve statistics, all measurements have been reflected to the same side of midrapidity.

The BES-I  $v_1$  measurements are based on the rather wide 10-40% centrality sample. The right-hand panel of Fig. 27 compares these measurements with the associated uncertainties for the 10-15% centrality class and the expected impact of the proposed statistics for BES-II on the  $v_1$  measurement for the  $\sqrt{s_{NN}} = 7.7$  and 19.6 GeV collision energies. It is expected that such significantly reduced uncertainties will allow for definite conclusions.

In addition, the restriction of measurements to the region near mid-rapidity is a serious limitation that must be overcome in order to reach a full understanding of the physics. Figure 29 illustrates the improved rapidity coverage of the iTPC via the extrapolated cubic and linear fits to  $v_1(y)$  for protons at 7.7 GeV measured in BES-I. Clearly the extrapolation to higher rapidity is a major source of systematic error in this analysis and it will be significantly reduced by the extended rapidity coverage of BES-II. The most significant point of Fig. 29 is that with the present rapidity coverage of the STAR TPC,  $v_1(y)$  carries insufficient information to go much, if at all, beyond a study of a single parameter like the slope  $dv_1/dy$  averaged over the current rapidity acceptance, especially when statistics are limited. In contrast, the much wider  $v_1(y)$  coverage of the iTPC opens the possibility to go well beyond a study of the single number yielded by the average slope just described. In light of the fact that proton and net-proton  $v_1$  near  $y = 0$  have proven to be a highly promising signature, it is clearly of great interest and importance to extend the same form of analysis to the adjacent regions away from  $y = 0$ . Simulations indicate that the improved statistics and extended rapidity acceptance, in combination with improved RHIC luminosity in the future, will be sufficient to meet this challenge.

Finally, the improved first-order event plane resolution of the EPD detector [48] directly leads to reductions in the required number of events to achieve the proton  $v_1$  centrality dependence BES-II physics goals as set out in the left panel of Fig. 27. Table 8 shows the updated number of required events at each BES-II energy, and it is clear that proton directed flow is below the level of driving the overall BES-II statistics request.

After the greatly improved BES-II measurements, any possible future explanation of  $v_1$  data in terms of purely hadronic physics would have to predict the detailed phenomenology of the centrality, rapidity, and transverse momentum dependence of directed flow for various particle species as a function of beam energy.

## 2.2 Global Polarization and Future Measurement of the Transient Magnetic Field During Heavy-Ion Collisions

In August 2017, STAR published in *Nature* the first observation of global polarization of  $\Lambda$  hyperons in heavy-ion collisions [38] and a graphic based on the STAR result was reproduced on the front cover. At intermediate centralities (20-50%), it was shown that the polarization direction of the  $\Lambda$ s is correlated, at the level of several percent, with the direction of the system angular momentum. As a result of this coupling, global  $\Lambda$  polarization measurements provide the first experimental access to the vortical structure of the “perfect fluid” created in a heavy-ion collision.

STAR’s observation of a non-zero signal of the global polarization of  $\Lambda$  hyperons for non-central Au+Au collisions at  $\sqrt{s_{NN}} = 7.7 - 39$  GeV, was with the level of 1.1–3.6 times statistical uncertainty at each energy. The fluid vorticity (non-relativistically defined in terms of the curl of the velocity vector) created at RHIC is estimated to be about  $9 \times 10^{21} \text{ s}^{-1}$ ; 14 orders of magnitude higher than that of any fluid observed to date. Thus, relativistic heavy-ion collisions produce not only record-setting temperatures and unprecedentedly low viscosity (in dimensionless units), but we now have experimental evidence that high-energy nuclear collisions generate unmatched high vorticity.

In 2016, Takahashi *et al.* [62] reported in *Nature Physics* the first observation of a coupling between the vorticity of a fluid (liquid mercury) and the internal quantum spin of the electron, opening the door to a new field of fluid spintronics. In their study, vorticity is generated through shear viscous effects as liquid mercury flows next to a rigid wall. Thus, STAR’s result at RHIC marks the first beginnings of the field of nuclear fluid spintronics.

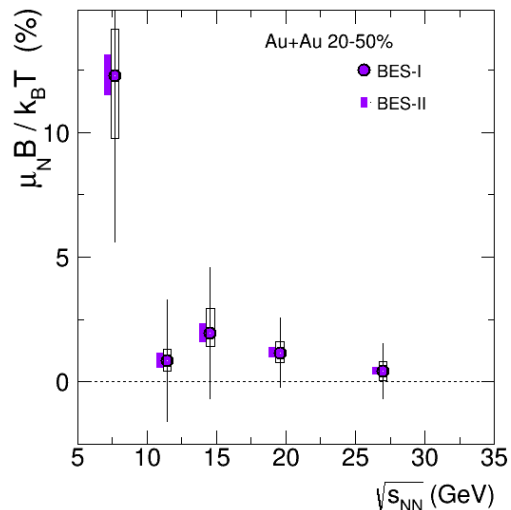


**Figure 30:** The global polarization difference,  $\bar{\Lambda}$  minus  $\Lambda$ , is directly proportional to the magnetic field  $B$  and varies inversely with the temperature  $T$ , as plotted here on the vertical axis. Ten percent on this dimensionless scale corresponds to a magnetic field of about  $8 \times 10^{14}$  Tesla. The points marked BES-I, along with their error bars, are based on the measurements published in [38], while the much smaller error bars marked BES-II in the legend indicate the expected statistical errors for event samples proposed in the BES-II whitepaper [45]. The plot includes a BES-I point at 27 GeV, and also an error bar for BES-II at this beam energy based on  $10^9$  events, as planned for Run 18.

The passing electric charges in nuclear collisions are expected to produce intense magnetic fields [63] parallel to the angular momentum vector of the system. So far, there is no experimental measurement of the magnetic field during a heavy-ion collision, and theoretical estimates become highly uncertain once the collision process starts. The  $\Lambda$  and  $\bar{\Lambda}$  have opposite intrinsic magnetic moments, and a larger global polarization for  $\bar{\Lambda}$  can be attributed to coupling between the field and the magnetic moments of the emitted particles [64]. An excess global polarization for  $\bar{\Lambda}$  is indeed observed [38], but with the existing BES-I statistics, it is only about a  $1.5\sigma$  effect. This significance can be seen in Fig. 30.

The projected significance of the likely magnetic field measurement in BES-II is presented in Fig. 30. The expected measurement at individual beam energies strongly fluctuates due to the large BES-I statistical errors, but combining all energies, the magnetic field measurement in BES-II is projected to be a  $9.6\sigma$  signal. The overall significance is dominated by the 7.7 GeV point with its very large statistical error. A more cautious projection can be made by simply assigning zero weight to the 7.7 GeV point when doing the statistics projection. Then the remaining energies would still yield a  $5.8\sigma$  signal with 50% of the original proposed BES-II statistics. The latter numbers are the basis of the new event requirement added this year to Table 8 in the row marked “ $>5\sigma$  Magnetic Field Significance”. Apart from the obvious goal of reducing statistical errors, it will be important in BES-II analyses of the magnetic field to understand systematic errors arising from factors like possible differences in the measured momenta of  $\Lambda$  and  $\bar{\Lambda}$  hyperons.

Assuming that the  $\sim 1.5\sigma$  hint of a magnetic field measurement provided by the BES-I data is enhanced as per the projections and thus confirmed by BES-II, this new result will establish yet another superlative — relativistic nuclear collisions produce the most intense magnetic field found in nature or generated in a laboratory environment. Experimental exploration of the magnetic field has great potential to become a new and exciting area of heavy-ion study.

It is a noteworthy and highly remarkable fact that the 2014 BES-II whitepaper [45] includes no mention anywhere of the topic of global hyperon polarization, much less measurements of fluid vorticity or the magnetic field. Global  $\Lambda$  polarization was first searched for by STAR in 2007 at 62.4 and 200 GeV [65], but those measurements were consistent with zero. At the time of writing of the 2014 BES-II whitepaper, there was no reason to suspect that BES-II, with its much lower statistics than 200 GeV, would uncover anything new in the area of global hyperon polarization. However, as we have seen, nature sometimes presents us with a welcome surprise, and the STAR detector has the flexibility and broad capabilities to be ready for novel opportunities that cannot always be anticipated during the BUR process.

### 2.3 Disappearance of the Chiral Magnetic Effect (CME) in Low-Energy Au+Au Collisions

As the collision energy at RHIC was decreased during the first phase of the Beam Energy Scan, several intriguing signatures that were ascribed to the formation of a QGP disappeared.

This included the CME charge separation signal as described in Sect. 1.2.4. It vanished below energies of  $\sqrt{s_{NN}} = 19.6$  GeV, which is consistent with the lessening of partonic influences at low energy. The CME depends on QGP formation, the presence of strong magnetic fields, and chiral symmetry restoration, so in collisions where a QGP is not formed, or is short-lived, the CME signal is not generated. Figures 31 and 32 show error projections at three different energies for the three-point correlator,  $\gamma$ , and the slope of  $\Delta v_2(A_{ch})$  assuming the requested event statistics for BES-II. The statistical precision possible for both observables is improved at all energies, but particularly at the lowest collision energies, where the QGP may not be formed.

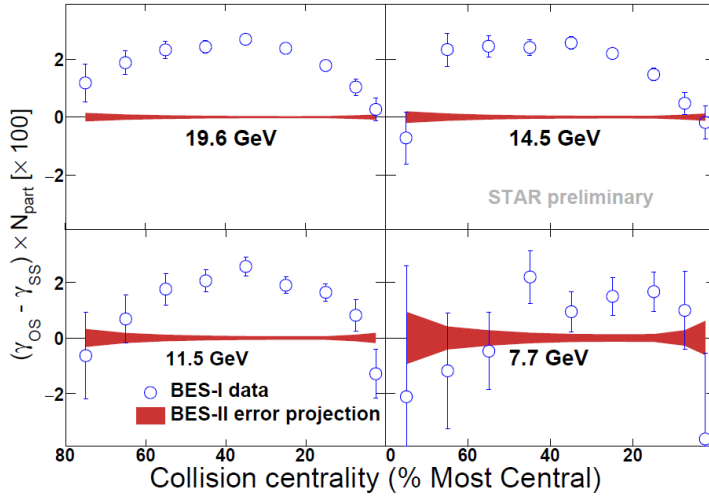


**Figure 31:** Error projections for the three-point correlator,  $\gamma$  (used to study the chiral magnetic effect), as a function of centrality for Au+Au collisions at four different energies with the requested statistics from the BES-II.

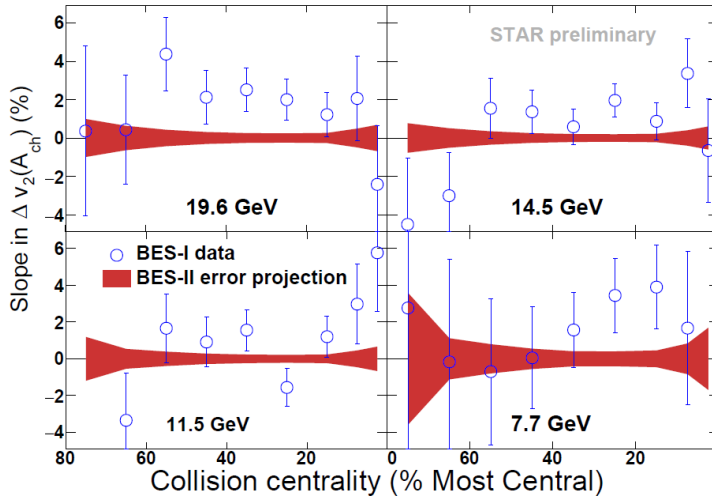


**Figure 32:** Error projections for the slope parameter (used to study the chiral magnetic wave), as a function of centrality for Au+Au collisions at four different energies with the requested statistics from the BES-II.

## 2.4 Dilepton Measurements and Search for Chiral Symmetry Restoration

Dileptons are a crucial probe of the strongly interacting matter created in ultra-relativistic heavy-ion collisions. Leptons traverse the medium with minimal interactions, but they are produced during the whole evolution of the created matter. Different kinematic ranges of dilepton pairs (mass and transverse momentum ranges) can be used to selectively probe the properties of the formed matter throughout its entire evolution.

The observed dilepton yields have contributions from many sources integrated over the entire evolution of the collision. In-medium properties of vector mesons (*i.e.* the mass and width of the  $\rho(770)$ ,  $\omega(782)$ , and  $\phi(1020)$  mesons) can be studied via their decays to dileptons in the low invariant mass ranges of lepton pairs ( $M_{ll} < 1.1 \text{ GeV}/c^2$ ). These in-medium properties may exhibit modifications related to possible chiral symmetry restoration. Observations at SPS and RHIC indicate enhancements of the dilepton yields at low  $p_T$  and in the low invariant mass range between the  $\pi$  and  $\rho$  mass. These enhancements cannot be described with model calculations that involve only the vacuum  $\rho$  spectral function.

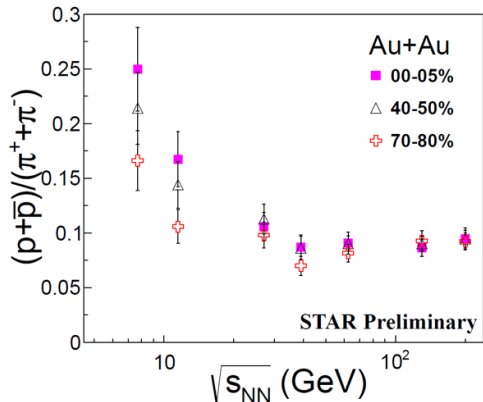


**Figure 33:** Total baryon density, represented by  $(p + \bar{p})/(\pi^+ + \pi^-)$ , *vs.* collision energy.

Dynamic models [66] show that the broadening of the width of the  $\rho$  can be attributed to interactions with the surrounding nuclear medium, *i.e.* to the coupling of  $\rho$  to the baryons and their resonances. These interactions affect the properties of the  $\rho$  even in the cold nuclear matter. In hot nuclear matter, where temperature and/or baryon density is high, these interaction are expected to cause the width to further broaden to the extent that it becomes indistinguishable from the radiation continuum. This continuum coincides with the dilepton thermal radiation from QGP at the phase transition temperature. Measuring the temperature dependence of the dilepton yields at low mass would thus be a key observable.

To help further disentangle the various factors that play a role in measuring the dielectron production in the low mass range, we show in Fig. 33 the charged baryon density *vs.* the collision energy. Here, the total baryon density at freeze-out is approximated by the measured ratio of the sum of proton and antiproton yields over the sum of charged pion yields. The plot shows that above approximately  $\sqrt{s_{NN}} = 20 \text{ GeV}$  the total baryon density remains almost independent of the beam energy. Consequently, the medium effect on the  $\rho$  meson and its dielectron spectrum are independent of beam energy when the dielectrons are emitted

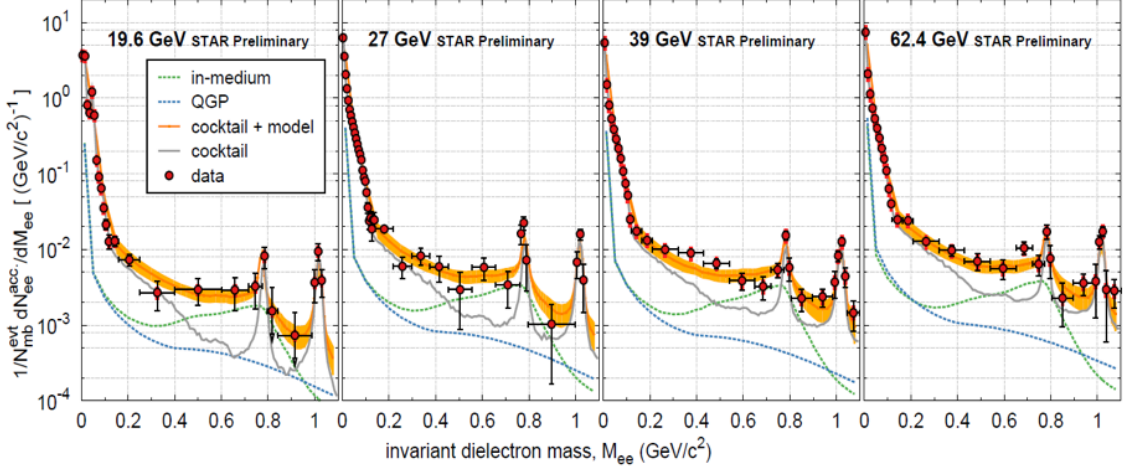


**Figure 34:** BES-1 preliminary results for the low-mass range dielectron invariant mass spectra at  $\sqrt{s_{NN}} = 19.6, 27, 39,$  and  $62.4$  GeV (red circles). The curves show the empirical contributions from empirical hadronic sources and the sum with a model calculation by Rapp, *et al.* The dotted lines are the in-medium and QGP contributions.

close to freeze-out. On the other hand, both the temperature and baryon density at the earlier stage of the collision strongly depend on the beam energy. This and the lifetime of the system are expected to impact the measured dielectron yields, and could result in measurable anomalies [67].

During BES-I, STAR collected dielectron data for minimum-bias Au+Au collisions at  $\sqrt{s_{NN}} = 19.6, 27, 39,$  and  $62.4$  GeV. Figure 34 shows the preliminary efficiency-corrected dielectron invariant mass spectra for these four beam energies. These dielectron measurements serve as an important bridge between those at top SPS and top RHIC energies, and provide an effective tool to study the temperature dependence of the  $\rho$  spectral function. These data are used to test models that involve a broadened  $\rho$  meson. Using these broadened  $\rho$  spectral function, verified against inputs from Lattice QCD through Weinberg/QCD sum rules, theorists have demonstrated [68] that when the temperature reaches 170 MeV, the  $a_1(1260)$  spectral function is the same as the  $\rho$  spectral function. This is a signature of chiral symmetry restoration as the axial vector meson  $a_1(1260)$  is considered to be the chiral partner of the  $\rho$  meson.

As can be seen in Fig. 33, further lowering the collision energy will result, in addition to a change in temperature, in a significant change in the total baryon density at freeze-out. Figure 35 shows the projected BES-II measurements from STAR together with data already taken at higher beam energies and compared to recent model calculations. STAR data in the BES-II era will cover a unique energy range because the excitation function above 20 GeV for the low mass region (LMR) depends strongly on initial temperature, while the LMR excess below 20 GeV depends more strongly on baryon density.

The dilepton spectra in the intermediate mass range ( $1.1 < M_{ll} < 3.0$  GeV/ $c^2$ ) are

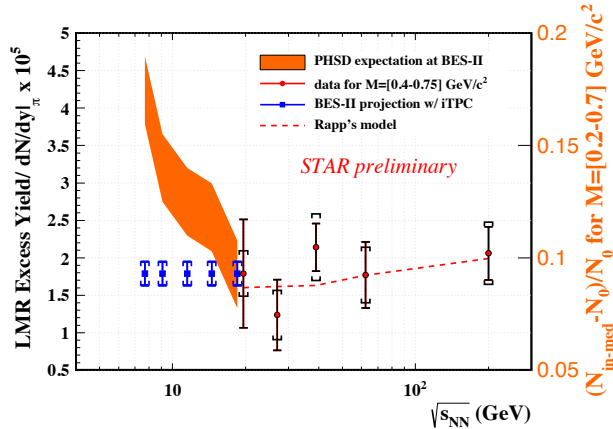


**Figure 35:** The Beam Energy dependence for the low-mass dielectron excess.

expected to be directly related to the thermal radiation of the QGP. However, significant background contributions from other sources have to be taken into account and measured experimentally. Such contributions include background pairs from correlated open heavy-flavor decays. For example, electrons or muons from the semileptonic decay of a pair of open charm or bottom hadrons,  $c \rightarrow l^+l$  or  $b \rightarrow l^+l$ , may be subject to in-medium modifications. In the high-mass region ( $M_{ll} > 3.0 \text{ GeV}/c^2$ ),  $J/\psi$ ,  $\Upsilon$ , and their excited states are used to study the color screening features of the QGP. Additionally, in the higher  $p_T$  range, direct photon yields have been derived through dielectron measurements at RHIC, allowing an assessment of thermal radiation. Large acceptance, precision measurements with a broad range of beam energies can provide invaluable insights in this subject.

STAR proposes to measure the low-mass range (up to  $M_{ll} \sim 1 \text{ GeV}/c^2$ ) dielectron spectrum down to  $\sqrt{s_{NN}} = 7.7 \text{ GeV}$  in order to further test the yields against models that connect the broadening of the  $\rho$  meson to chiral symmetry restoration.

At the same time, measurements of the intermediate mass range will allow STAR to determine how this range may smoothly transition and match to the  $p_T$  slopes in the low-mass range. While the charm contribution in the low-mass range will significantly drop with lower collision energies, charm rates continue to dominate the intermediate mass range. During BES-II STAR's muon detection capabilities will allow for independent measurements, through  $e\mu$  correlations, of the charm contribution to the dilepton continuum. Finally, one can also change the total baryon density by shifting the analysis frame from midrapidity towards a more forward rapidity.

The rapidity dependence of the total baryon density will provide a strong and independent observable to study the dependence of the low-mass dielectron emission on the baryon density.

Figure 36 shows the  $e^+e^-$  invariant mass distribution from Au+Au collisions at 200 GeV and U+U collisions at 193 GeV for  $p_T < 0.15 \text{ GeV}/c$ . The  $e^+e^-$  invariant mass distribution is shown for 60 – 80%, 40 – 60%, and 10 – 40% collision centralities. For each case the expected contribution from hadronic sources (excluding the  $\rho$  meson) is shown as a solid black curve. In 60 – 80% Au+Au and U+U collisions there is a significant excess visible with respect to the corresponding hadronic cocktail. The excess is less significant in 40 – 60% collisions

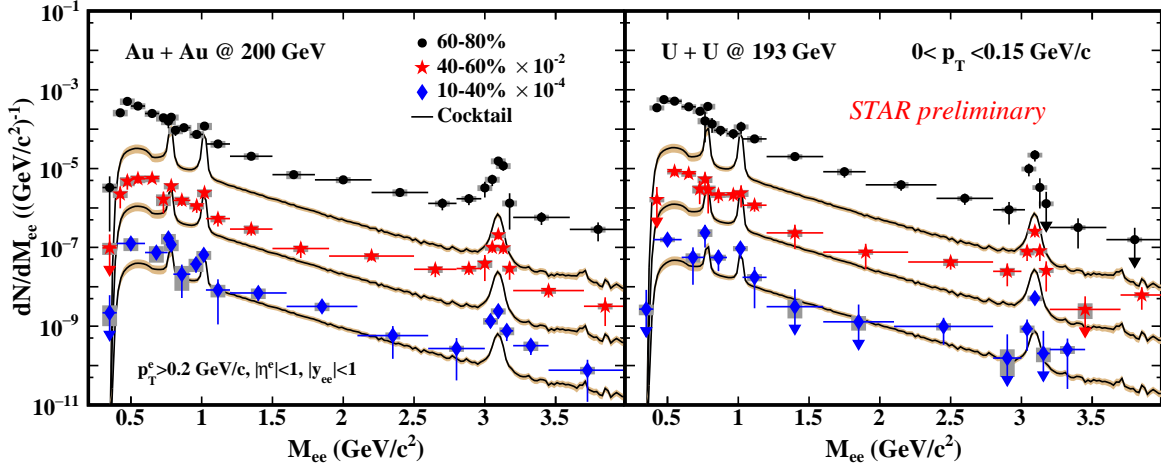


**Figure 36:** The low  $p_T$  ( $0 < p_T < 0.15$  GeV/ $c$ )  $e^+e^-$  invariant mass distribution for Au+Au collisions at 200 GeV (left) and U+U collisions at 193 GeV (right). The invariant mass distributions for collisions with 60 – 80%, 40 – 60%, and 10 – 40% centrality are shown. For each centrality the corresponding hadronic cocktail contribution is shown as a solid curve with the uncertainty as a shaded region.

and the data from 10 – 40% collisions are consistent with the expectation from the hadronic cocktail. The excess yield with respect to the hadronic cocktail is shown in the left panel of Fig. 37 for 60 – 80% Au+Au and U+U collisions and the expected excess in Au+Au collisions at 19.6 GeV along with the additional contributions expected from an in-medium modified  $\rho$  and thermal radiation from the QGP. The sum of these additional contributions is insufficient to explain the observed excess.

In Fig. 38, the preliminary acceptance-corrected excess spectrum for  $\sqrt{s_{NN}} = 27$  GeV is shown. Superimposed on the data points are projections of the improved uncertainties of our measurements for two scenarios. The uncertainties for each scenario are based on the measured preliminary uncertainties from the Run 11 data taking at 27 GeV. Furthermore, it includes the projected improvement of  $\sim 1.9$  for the Au-beam luminosity at 27 GeV, as well as an estimate of the performance envelope of the STAR DAQ rates based on Run 15’s performance (saturate at 1.7 kHz). The scenarios involve two cases: (i) running for 2 RHIC weeks at a data-taking efficiency comparable to what was previously achieved for the same energy during Run 11 and (ii) running for 3 full weeks. These scenarios yield approximately 400M and 700M events that pass the analysis criteria for both scenarios, respectively.

As a result, we expect the average uncertainties to reduce by a factor of 2.4 (2-week scenario) up to 3.2 (3-week scenario). Model calculations [69] show that for dielectron masses above that of the  $\phi$  meson the main contribution to the dielectron spectra arrives from the QGP component. The projected improvements in either scenario allow for the first measurement in this intermediate mass range, thus allowing a first potential measurement of the temperature of the hot medium at this energy.

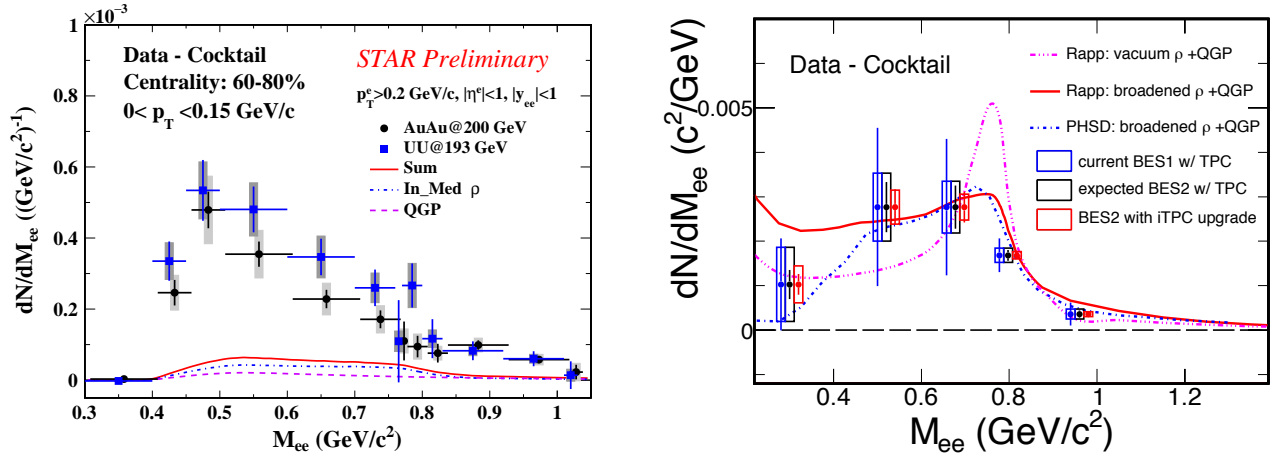


**Figure 37:** Left: The low  $p_T$   $e^+e^-$  excess yield with respect to the hadronic cocktail for Au+Au and U+U collisions with 60–80% centrality. The additional contributions expected from in-medium modified  $\rho$  production, QGP thermal radiation, and the sum of the two are shown. Right: The expected dielectron excess invariant mass spectra in Au+Au collisions at 19.6 GeV. Comparisons to PHSD and Rapp’s model calculations are also shown. The bars and boxes represent the statistical and systematic uncertainties respectively.

## 2.5 Onset of Deconfinement: the Disappearance of QGP Signatures

Every QGP signature, measured by STAR experiment during first phase of the BES program, will benefit from extended  $\eta$  coverage, improved  $dE/dx$  and lowered  $p_T$  cut-off in BES-II. Here we discuss, as examples, the improvement to elliptic flow analysis of  $\phi$  meson and to nuclear modification factor  $R_{CP}$ , which was intensively studied in BES-I.

### 2.5.1 Elliptic Flow $v_2$ of $\phi$ Meson

The results of analysis of BES-I data suggest that NCQ scaling, first observed at  $\sqrt{s_{NN}} = 200$  GeV, may no longer hold at lower energies. As the energy is lowered, the violation of NCQ scaling becomes stronger, and the splitting between mesons and baryons becomes stronger. These observations are consistent with the expectation that the system spends a smaller percentage of the collision duration in the partonic phase as the beam energy is lowered, and that at the lowest BES energies, the system might not reach the QGP phase at all.

The study of the  $v_2$  of particles with a very small hadronic cross section may elucidate to a much higher degree the partonic dynamics and collectivity in heavy-ion collisions.

The  $\phi$  meson, which is a bound state of the  $s$  and  $\bar{s}$  quarks, has a small interaction cross section with other hadrons, and freezes out early [70, 71]. Due to the small hadronic interaction cross section of the  $\phi$  meson, its  $v_2$  is almost unaffected by later-stage hadronic interactions, and will have a negligibly small value if  $\phi$ ’s are not produced via  $s$  and  $\bar{s}$  quark coalescence in the partonic phase [72]. Therefore the elliptic flow of the  $\phi$  meson is particularly interesting because the entire magnitude of its elliptic flow is expected to

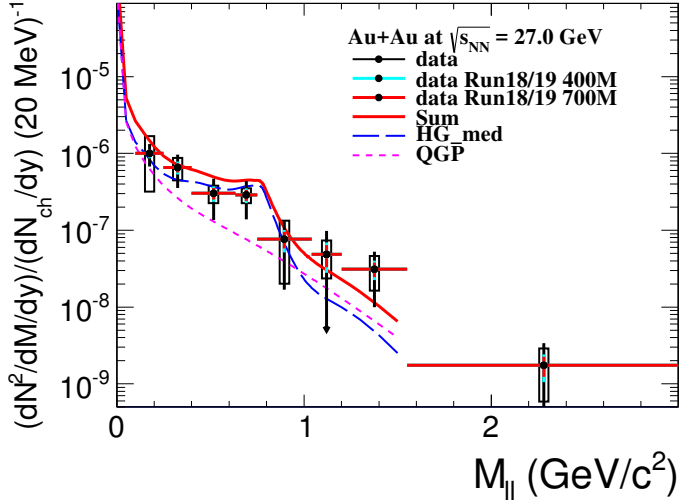


**Figure 38:** STAR preliminary measurement of the acceptance-corrected dielectron invariant mass spectrum for  $\sqrt{s_{NN}} = 27$  GeV. The hadron cocktail has been subtracted. The dotted and striped curves depict calculations by Rapp *et al.* that include a hadron gas (HG) and quark-gluon plasma (QGP).

originate from the partonic phase.

Figure 39 presents  $v_2(p_T)$  at 7.7 and 11.5 GeV for several identified particle types, scaled on both axes by the number of constituent quarks. The  $\phi$  meson result, the solid magenta circles with error bars, illustrate the fact that BES-I statistics for the  $\phi$  are far less than what is needed to reach a useful physics conclusion at these two beam energies. The height of the blue band in the lower part of each panel illustrates the errors estimated with the BES-II statistics, while the height of the red band shows the expected error with BES-II statistics and with the enhanced midrapidity acceptance of the iTPC. It is necessary to make measurements up to  $p_T = 3$  GeV/ $c$  with a statistical error of less than 10% on  $v_2$ . From this requirement we estimated the statistics necessary (see Table 8) for BES-II to reach transverse momenta beyond 2.5 GeV/ $c$  even at the lowest energies. This will allow us to test NCQ scaling in detail for many particle species, including multi-strange particles, and quantitatively address the suspected decrease, followed by an absence, of partonic collectivity below  $\sqrt{s_{NN}} = 19.6$  GeV.

Without the iTPC and eTOF upgrades, 100M and 200M useful minimum-bias events are required from the Au+Au collisions at 7.7 and 11.5 GeV, respectively. The blue band in Figure 39 does not include reduction of statistical errors due to iTPC upgrade. For example, for the lowest, and most statistics hungry, energy of 7.7 GeV this reduction of statistical error amounts to 12%, which translates to a significant decrease in the number of required minimum bias events at this energy: 100 million events without the upgrade drops to “only” 77 million (rounded to 80 million). This reduction to at least 80 million minimum bias events needed to perform the  $\phi$  meson elliptic flow analysis means that this observable is no longer a “driver” of our BUR request for the BES-II program.

These measurements will answer decisively the question how much  $\phi$  meson flow there is compared to that of light quark hadrons? Lack of the collectivity of the  $\phi$  meson will provide clear evidence of a hadronic-interaction dominated medium in low energy heavy ion collisions.

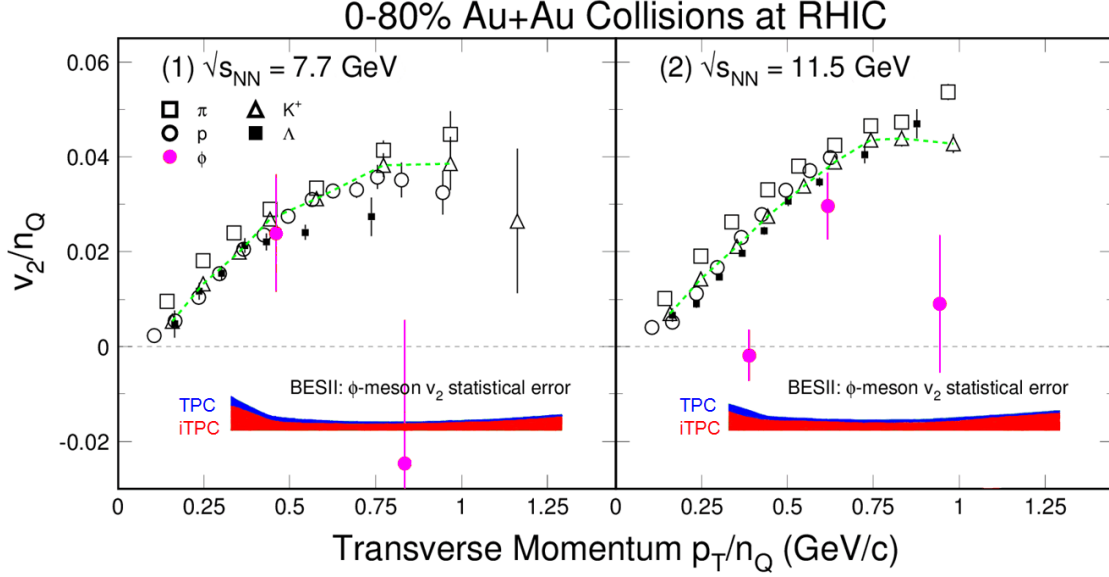


**Figure 39:** Scaled  $v_2$  of the  $\phi$  meson showing the projected error bars for BES-II with the current STAR TPC (blue band) and with the iTPC (red band).

### 2.5.2 Nuclear Modification Factor $R_{CP}$

Another broadly discussed result from BES-I related to the onset of deconfinement is the  $R_{CP}$  measurement shown in Fig. 40 (for all BES-I energies) and Fig. 42 (for 7.7, 11.5 and 19.6 GeV). The high- $p_T$  suppression observed at the top RHIC energies is seen as an indication of the energy loss of partons in a colored medium, and the  $R_{AA}$  measurements are one of the clearest signatures for the formation of the quark-gluon plasma. This suppression is expected to vanish at low collision energies, where the energy density becomes too low to produce a significantly large and long-lived QGP. Because there was not a comparable  $pp$  energy scan, the BES analysis has had to resort to  $R_{CP}$  measurements as a proxy. Still the study of the shape of  $R_{CP}(p_T)$  will allow us to quantitatively address the evolution of jet-quenching to lower beam energies.

A very clear change in behavior as a function of beam energy is seen in these data (see Fig. 40); at the lowest energies (7.7 and 11.5 GeV) there is no evidence of suppression for the highest  $p_T$  values that are reached. This plot demonstrates the turn-off of net suppression for high- $p_T$  hadrons produced in central collisions (0-5 %), relative to those produced in peripheral collisions, (60-80 %), as expected for this signature of QGP formation. Fig. 40 clearly demonstrates that enhancement effects become very large at lower energies. This does not exclude the possibility of QGP formation in the 7.7 and 11.5 GeV datasets, but simply demonstrates that enhancement effects (Cronin type interactions, radial flow, and the relative dominance of coalescence versus fragmentation for hadronization) might increase faster than quenching effects at these energies. In order to identify at what collision energy

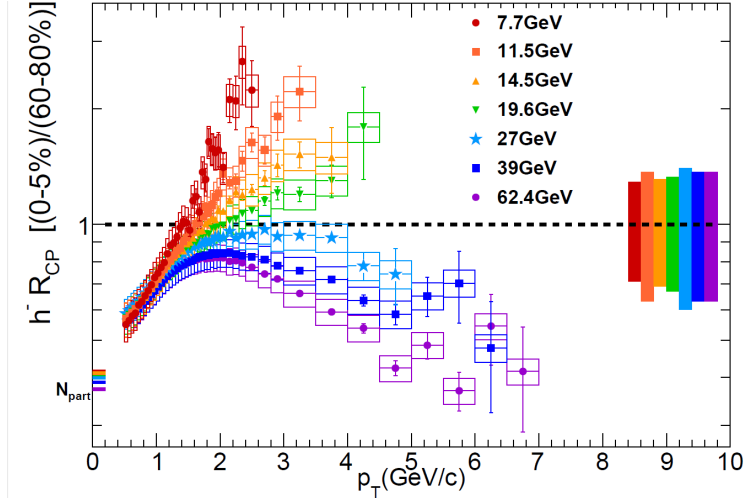


**Figure 40:** Nuclear modification factor versus transverse momentum for negatively charged hadrons from Au+Au collisions at various  $\sqrt{s_{NN}}$  at RHIC. The yield ratios for charged hadrons are taken for 0-5% to 60-80% collision centrality.

a QGP is formed, more sensitive observables are required. Therefore, we investigated  $R_{CP}$  for identified hadrons. Figure 41 shows  $R_{CP}$  as a function of  $p_T$  for feed-down subtracted identified particles at different collision energies. While net enhancement of high- $p_T$  particles is observed at all energies for protons and anti-protons, high  $p_T$  pions are suppressed for both 39 and 62.4 GeV, which drives the trends observed in charged hadrons. Kaons have similar energy dependence to pions, but show less net suppressions.

We have used the yields of identified particles measured in BES-I to make projections of the expected errors for the  $R_{CP}$  measurements with increased statistics of BES-II. Fig. 42 shows the BES-II projected error bands for  $\pi$ , K, and p for 7.7, 11.5, and 19.6 GeV. For clarity, the errors for 7.7 GeV energy, marked in red, are scaled by factor 10, those for 11.5 GeV energy, marked in blue, are scaled by factor 100 and those for 19.6 GeV, marked in green, are scaled by 1000. The error bands are truncated when the error reaches 50%; this represents the expected high  $p_T$  limit for each measurement.

While we do not expect to reach  $p_T$  range of  $\sim 5$  GeV/ $c$  for the lowest BES energies, we will be able, with the BES-II statistics, to investigate identified particles in the intermediate  $p_T$  range, which may allow us to better understand the Cronin effect and the evolution of  $R_{CP}$  (see Fig. 42 and Table 8.)

We have also projected the expected errors in BES-II for the inclusive charged hadron  $R_{CP}$  measurements, and we found that the high  $p_T$  limits for this measurement are: 5.2, 5.7, and 6.5 GeV/ $c$  for the 7.7, 11.5, and 19.6 GeV systems, respectively.

The improvements of particle identification and momentum resolution due to detector upgrades in BES-II directly result in reduction of the required number of events for accomplishing BES-II physics goals. The updated numbers of events for each energy, shown in Table 8, clearly demonstrated that  $R_{CP}$  analysis requirements are well below the level of driving the BES-II statistics request.

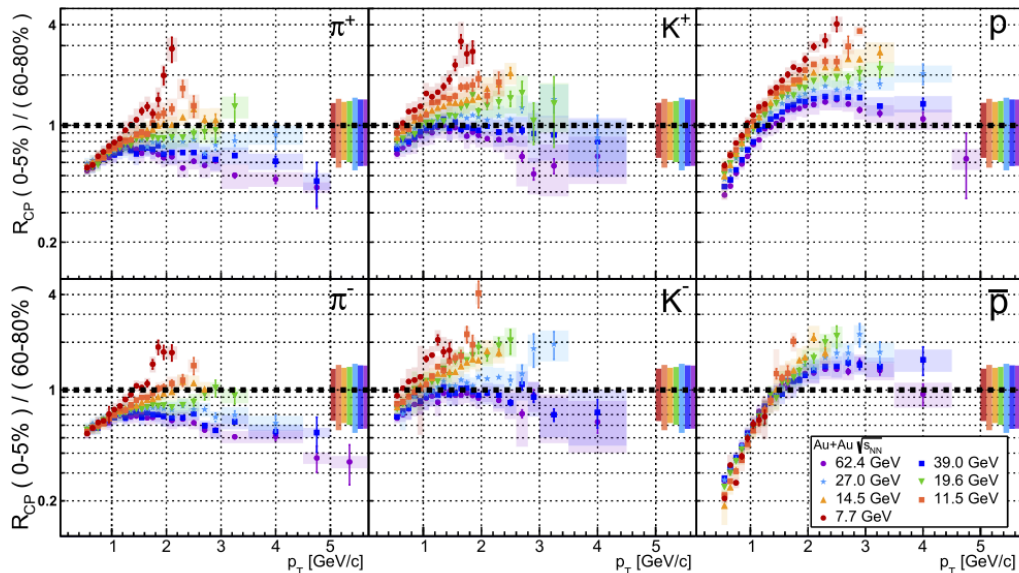


**Figure 41:** Identified particle  $R_{CP}$  for RHIC BES energies. The color shaded boxes describe the systematic uncertainties.

## 2.6 Higher Moments and the Search for the QCD Critical Point

Thermodynamic principles indicate that QCD matter should exhibit a first-order phase transition ending in a critical point, with a crossover transition thereafter [73, 74]. The discovery of the critical point would be a significant outcome of the RHIC BES programs. Models suggest that the critical point might be signaled by large fluctuations in event-by-event multiplicities of conserved quantities such as net-baryon number, net-charge, and net-strangeness. These quantities have variances  $\langle(dN)^2\rangle$  that are proportional to the correlation length ( $\xi$ ) squared. Higher moments like skewness,  $S$ , which is proportional to  $\langle(dN)^3\rangle$  and varies as  $\xi^{4.5}$  and kurtosis,  $\kappa$ , which is proportional to  $\langle(dN)^4\rangle$  and varies as  $\xi^7$ , are more strongly correlated with  $\xi$  and are argued to offer higher sensitivity to critical fluctuations [75, 76, 77]. In addition, the moments are related to the susceptibilities ( $\chi$ ) [78] and hence a comparison can be directly made to QCD calculations [79, 80]. Motivated by these considerations, STAR has studied the kurtosis times the variance ( $\kappa\sigma^2$ ) of net protons (a proxy for net baryons), net kaons (a proxy for net strangeness), and net-charge distributions to search for the critical point [81, 82, 83]. In the absence of a critical point, the hadron resonance gas model [84] suggests that the  $\kappa\sigma^2$  values will be close to unity and have a monotonic dependence on  $\sqrt{s_{NN}}$  [?]. However, because  $\kappa\sigma^2$  is related to the ratio of conserved number susceptibilities in QCD models ( $\kappa\sigma^2 = \frac{\chi^{(4)}}{\chi^{(2)}/T^2}$  [79]), it is expected to show a non-monotonic dependence on  $\sqrt{s_{NN}}$  close to the critical point.

Searches for the QCD critical point will only be successful if nature places that point within the search range of the BES-II program. Some studies place the QCD critical point

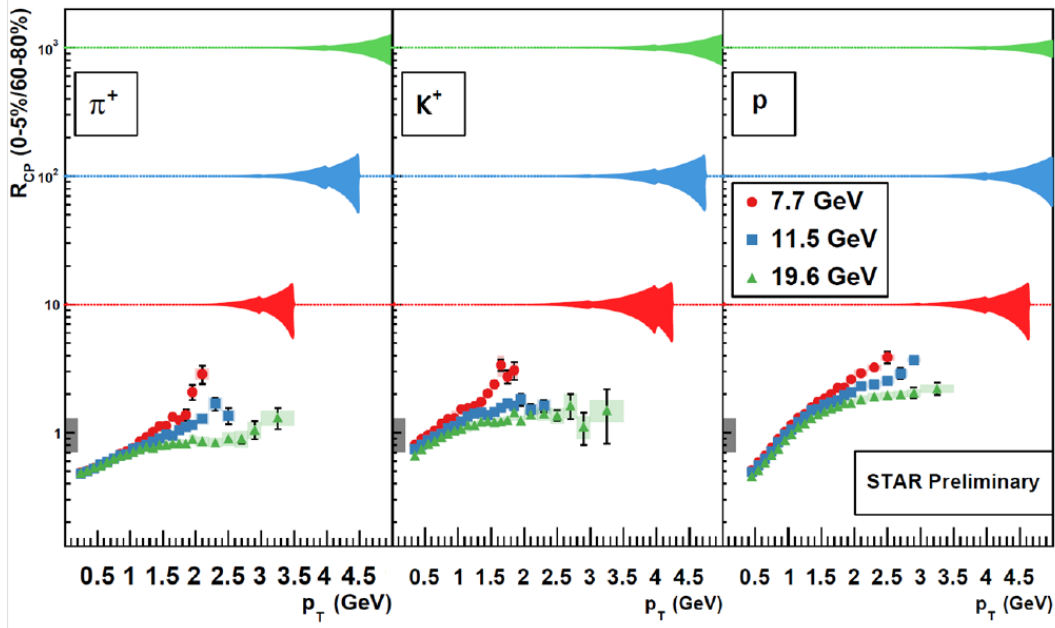


**Figure 42:** The BES-I  $R_{CP}$  data are shown for  $\pi$ , K, and p for 7.7, 11.5, and 19.6 GeV. The BES-II projected error bands are for the same energies, 7.7 (red, scaled by 10), 11.5 (blue, scaled by 100), and 19.6 (green, scaled by 1000).

within the BES-II search range [85, 86], but it is fair to say that theoretical studies have not converged on a best estimate of the location. Recent studies have attempted to exclude certain regions of the QCD phase space. Lattice QCD studies have excluded the high  $T$  and low  $\mu_B$  region of the phase diagram [87]. Finite-size scaling analysis suggests excluding regions with  $\mu_B$  below 440 MeV [88], and temperatures above 155 MeV. These regions are unlikely due to constraints from the curvature of transition lines [89]. Recent analyses using a truncated Dyson-Schwinger [90, 91] have suggested a critical point with  $\mu_B$  of 500 MeV, while black hole engineering studies suggest 720 MeV [92].

The experimental search for evidence of the critical point through the study of the higher moments of the fluctuations in event-by-event multiplicities of conserved quantities has produced suggestive results as shown in Fig. 43. The STAR results show a minimum at 19.6 GeV, and a rise at 7.7 GeV. These results are consistent with the energy trends suggested by theory [77] for behavior in the vicinity of a critical point. However, the theory also suggests that the  $\kappa\sigma^2$  signal should return to the Poisson baseline for energies below the critical point. It is intriguing to note that a recent study of Au+Au collisions at 2.4 GeV by HADES has found  $\kappa\sigma^2$  significantly above the Poisson baseline [93]. Although this result is puzzling, there are significant differences in acceptance between STAR and HADES making interpretation challenging.

The addition of the 9.1 GeV beam energy in BES-II and the fixed-target program will provide STAR with several collision energies in the vicinity of the observed rise in fluctuations

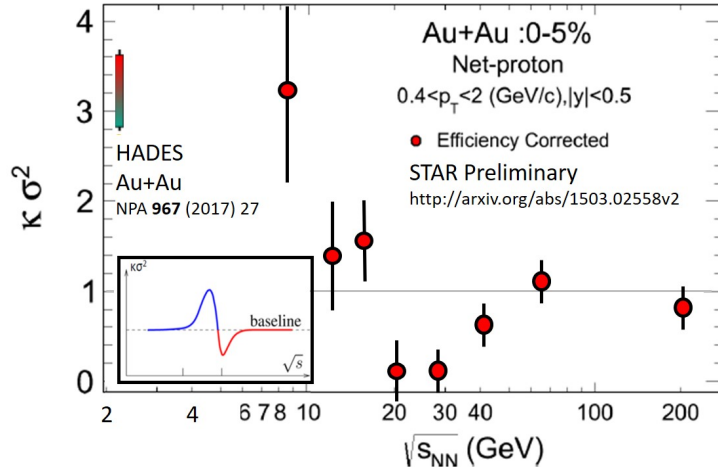


**Figure 43:** The experimental measurements of the net-proton  $\kappa\sigma^2$  from both STAR [94] and HADES [93]. The inset to the lower left is a theoretical prediction of the energy dependence [77] (arbitrarily scaled).

at 7.7 GeV. Detailed mapping of this proposed peak in fluctuations could provide convincing evidence of critical behavior. A fixed-target physics run at 3.0 GeV will be completed in June 2018. This will provide 100 million events and allow a precise measurement of the net-proton  $\kappa\sigma^2$ .

Another area of concern with the net-proton  $\kappa\sigma^2$  analysis is the efficiency corrections [95]; this can be seen in Fig. 43. An important feature of the energy scan program is the the 7.7 GeV energy will be run in both collider and fixed-target mode. The detector acceptances are significantly different in these two configurations and consistency between the collider and fixed-target result at 7.7 GeV will add confidence to the application of these efficiency corrections.

In light of the improved detector acceptance due to the iTPC and eTOF upgrades, it is appropriate to revisit the event statistics required to achieve the physics significance necessary to determine whether the variations of the  $\kappa\sigma^2$  observable are indicative of critical behavior. The net-proton higher moments analysis selects only protons with  $|y| < 0.5$  and  $p_T > 400$  MeV. Most of this analysis window falls with the current acceptance of STAR, however  $\eta = 0.96$  acceptance limit cuts off the low  $p_T$  corners near  $|y| = 0.5$ . The upgrades will allow full coverage in the analysis window, and this will increase the  $\langle N_p \rangle$  by 5% for all BES-II energies, increasing the significance of the physics results by 15% ( $1.05^3$ ), thus the event statistics required for the higher moments analysis has been reduced accordingly from the 2014 BES-II proposal.

## 3 Proposal for Fixed Target Program

### 3.1 Motivation for the FXT Program

In the RHIC collider mode, the lowest collision energy available is  $\sqrt{s_{NN}} = 7.7$  GeV. The fixed-target (FXT) program at STAR, with the iTPC and eTOF upgrades, will enable the energy scan range extension from 7.7 down to 3.0 GeV. It is important to measure key observables at energies lower than 7.7 GeV for several reasons:

- Some of the QGP signatures, observed at the top RHIC energies, fade or disappear at 7.7 GeV. We need to extend the energy range so that we can confirm that these signatures have indeed turned off.
- Findings, in particular the net proton kurtosis fluctuations (see section 2.6) from the first round of the BES program, suggest the possibility of critical point signals in the vicinity of 7.7 GeV. It is predicted that fluctuations rise and fall in the region of the critical point. The rise from the higher energy side is observed (Fig. 43), but the lower energy side can be only studied at RHIC with fixed target data. Any comparison with the recent HADES results at 2.4 GeV is difficult to interpret, since HADES data pertains to a different acceptance.
- There are theoretical calculations suggesting that the mixed phase is entered at energies well below 7.7 GeV [96].
- The CERN NA49 experiment results suggest that the onset of deconfinement occurs at 7.7 GeV [97].

The BES-I program was first proposed in the Run 7 STAR BUR; at that time, energies of 4.6 and 6.3 GeV were proposed. In the Run 9 STAR BUR, 100k events were requested at 5.0 GeV. C-AD tried circulating beams at 5.5 GeV (Run 9) and 5.0 GeV (Run 10), but due to the low luminosity, operating below 7.7 GeV proved to be impractical. The FXT program provides a practical way of acquiring data below 7.7 GeV and was included in the 2014 BES-II proposal.

In order to determine the best conduct of operation for a FXT program at RHIC, a gold target was installed inside the beam pipe in Run 14. The target was 1 cm in height, 6 cm in width, and 1 mm thick. The target was positioned 2 cm below the beam, and 2.1 meters to the west of the center of the detector (see Fig. 44).

The iTPC and eTOF upgrades improve the acceptance of STAR for the FXT. In particular:

- The largest  $\eta$  of the barrel TOF system in FXT mode is 1.47. The eTOF system covers  $\eta = 1.52$  to 2.24, extending detector coverage significantly.
- The track length in the STAR TPC for particles with  $\eta > 0.88$  is longer in fixed-target events. Therefore, the  $dE/dx$  resolution for these tracks is better than for tracks with similar  $\eta$  values in collider events.

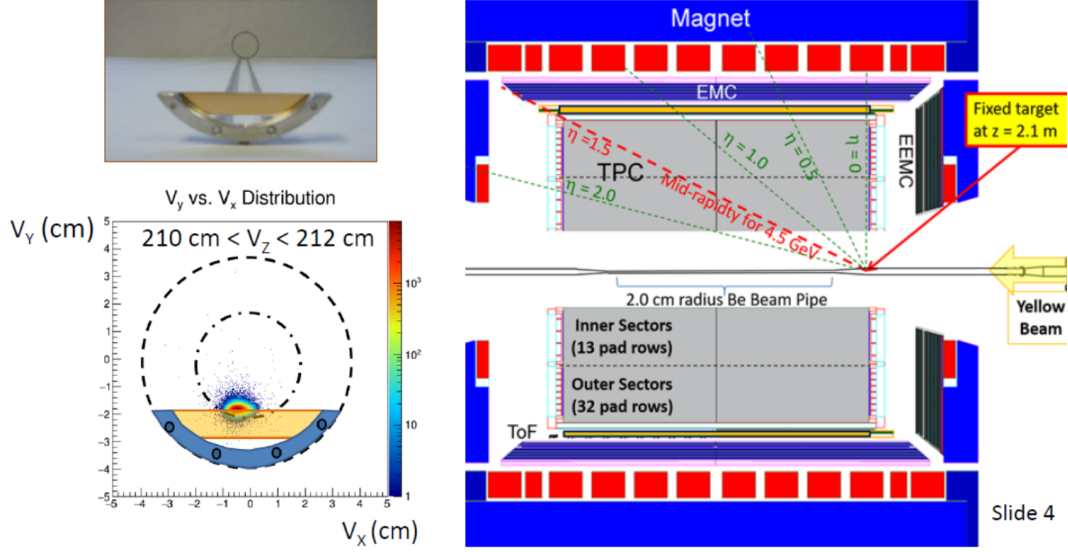


**Figure 44:** The top-left panel shows an image of the internal gold target. The lower-left panel shows the distribution of vertices with respect to the target. The right panel shows a side view of the STAR detector and the  $z$  location of the target.

- The flight path for particles with  $\eta > 0.96$  is longer in fixed-target events. Therefore, the TOF PID limits for these tracks extend to higher momentum than for tracks with similar  $\eta$  in collider events.

The acceptance and PID ranges for fixed-target events are shown in Fig. 45.

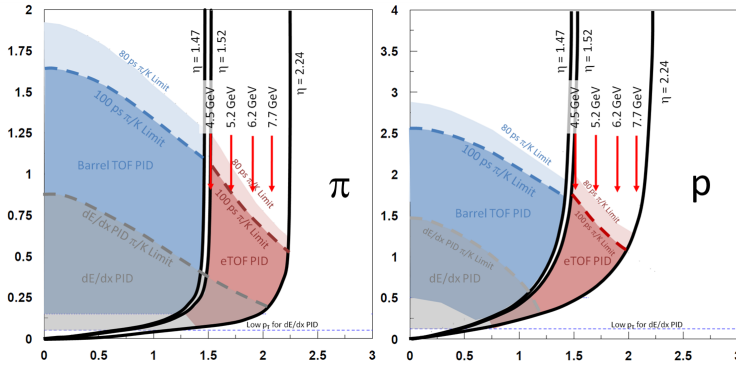


**Figure 45:** Acceptance maps in  $p_T$  vs.  $y$  space for the STAR detector in FXT mode. The regions in pink require the iTPC and eTOF upgrades.

### 3.2 FXT Test Runs

Preliminary results from the first dedicated FXT test run, conducted in 2015, with Au+Au at 4.5 GeV were already shown at recent QM conferences. Spectra and yields of pions, kaons and  $\Lambda$ 's as well as a directed flow of protons, elliptic flow of identified hadrons and HBT radii were presented and compared with previous results from AGS experiments. All the new

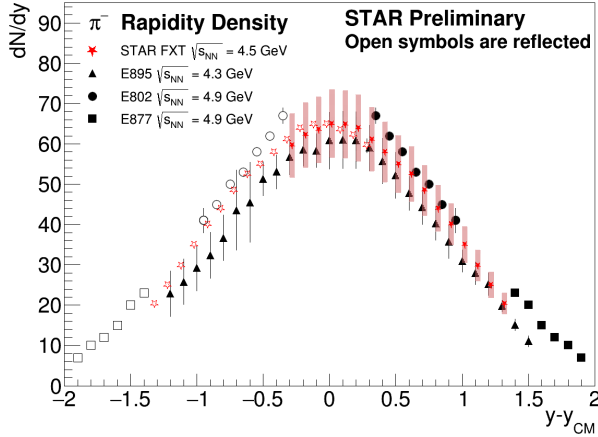


**Figure 46:** Rapidity density  $dN/dy$  for negative pions at  $\sqrt{s_{NN}} = 4.5$  GeV based on STAR FXT measurements, compared with published results from three AGS experiments [98, 99, 100] at nearly the same beam energy.

FXT results are consistent with earlier ones at similar energies, which validates the STAR FXT approach. These results demonstrate that STAR has good event reconstruction and particle identification capabilities in the fixed-target configuration.

From the point of view of conduct of operations, it was concluded that dedicated runs in which the elevation of the circulating beam is lowered to graze the top edge of the target can safely deliver a sufficient event rate to fill the DAQ bandwidth of STAR. For FXT events, STAR can take data at 2 kHz; therefore STAR can accumulate 50 million events per day (assuming data-taking 60% of the time).

The first publication of FXT results with Au+Au collisions at 4.5 GeV (to be submitted to PRC) is currently undergoing the STAR internal review process. As an illustration, we show in Fig. 46 the negative pion rapidity densities from STAR FXT data and from earlier AGS experiments E895 [98], E802 [99] and E877 [100]. Agreement between experiments is very good (note the slight difference in energies). Moreover, the 2015 FXT test run at 4.5 GeV allowed us to make the very first measurement of directed and elliptic flow of pions at this energy.

Recently, STAR has been able to perform a higher energy FXT test run. On April 19<sup>th</sup> 2018, a single gold beam of energy 26.53 GeV was circulating in RHIC for coherent electron cooling tests. By steering this beam close to STAR’s fixed-target, it was possible to simultaneously perform an FXT test with Au+Au collisions at  $\sqrt{s_{NN}} = 7.2$  GeV, close to the top proposed FXT energy of 7.7 GeV. This test had two goals. The first was to verify the proposed conduct of operations with accelerated beams; the 2015 tests used beams at injection energy which have a broader transverse profile. The second goal was to develop a minimum bias FXT trigger; the 2015 test used top 30% central triggers. The left panel of Fig. 47 shows the  $x - y$  distribution of the reconstructed event vertices. The majority of vertices are located at the top edge of the target ( $y = -2.0$  cm) as expected. It is interesting to note that there is a more diffuse cluster of vertices located at  $y = -1.4$  cm; these are “beam-gas” events which are evident because we had very loose trigger requirements, however this does give a very visual sense of the conduct of operations showing the profile of the ion beam circulating a few millimeters above the top edge of the target. The right panel shows the raw

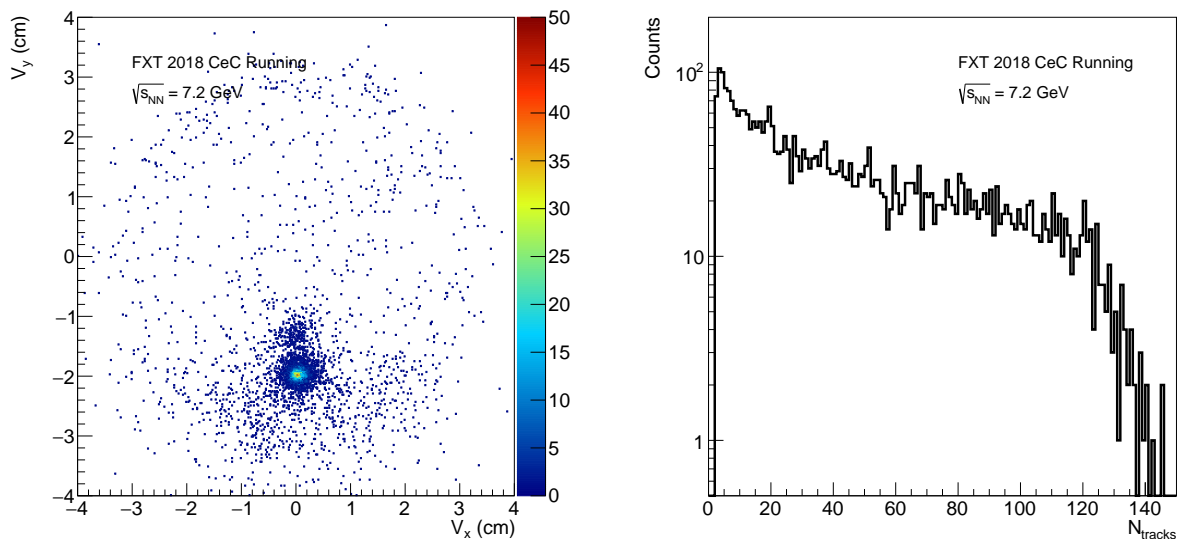


**Figure 47:** (Left) The  $x - y$  locations of  $\sqrt{s_{NN}} = 7.2$  GeV Au+Au vertices from the test on April 19<sup>th</sup>, 2018. (Right) The charged track multiplicity distribution for the vertices associated with the gold target.

charged particle multiplicity distribution for the target related events, and clearly exhibits the shape expected for a minimum bias trigger.

### 3.3 FXT Physics Program

Assuming a first-order phase transition, the concept of a single “onset of deconfinement” may be an oversimplification. Depending on the universality class of the phase transition, there can be a spinodal decomposition which would imply a mixed-phase region with a negative compressibility. Rather than a single “onset”, there may actually be several interesting onsets: the lowest energy which causes some fraction of the system to enter the mixed phase region, the energy at which the system spends the maximum amount of time in the instability regime, and the energy at which the system passes into the pure QGP phase. In order to understand the nature of the phase transition, we propose to study several observables in the context of the FXT Physics Program which are expected to have sensitivity to the compressibility.

(i) As is mentioned in the previous section, the directed flow of protons offers sensitivity to the early compressibility. We will study the evolution of the mid-rapidity “wiggle” which is particularly sensitive to compressibility and is known to be absent [101] at the lower end of the proposed fixed-target beam energy range. (ii) The width of the pion rapidity density distribution has been argued to be sensitive to the speed of sound in nuclear matter [102]. (iii) Femtoscopy measurements would further allows us to study the tilt angle [103, 104, 105] and volume of the pion source [106]. (iv) The elliptic flow of protons has been shown to change sign at a fixed-target beam energy of 6 AGeV ( $\sqrt{s_{NN}} = 3.5$  GeV) [107]. Its change is

explained by the transit speed of the projectile nucleus through the target nucleus matching the expansion speed from compression (speed of sound). (v) Finally, the Coulomb potential of the pion source provides an independent means of assessing the source volume, being affected by the expansion velocity of the system [108].

The fixed-target program will allow us to track other QGP signature observables, studied in the BES-I, spanning a collision energy range from 3.0 to 19.6 GeV ( $\mu_B$  from 720 to 205 MeV). (i) The NCQ, scaling for particles, which we discussed in the previous section, is expected to break at fixed-target energies. (ii) The rapidity correlator [109] sensitive to QGP formation. In the BES-I data this balance function shows a decreasing signal with decreasing beam energy [110]. Lower energy measurements are needed to demonstrate that this signature disappears. (iii) Strangeness enhancement is seen as an important QGP signature. The energy range covered by the fixed-target program sees the opening of several strange particle production channels. Currently, there is only a single  $\Xi^-$  measurement for collision energies below 7.7 GeV [111]. The STAR fixed-target program will map out the turn on of  $\Xi$  production with collision energy. Measurements of  $\Omega$ ,  $\bar{\Lambda}$ , and  $\bar{\Xi}^+$  have not been made at these energies previously. Using the eTOF, a study of the onset of the production of these species could be possible.

NA49 data suggest that the onset of deconfinement is achieved at 7.7 GeV [97]. This result is based on a set of inclusive observables: there is a kink in the rate of increase of the pion production with collision energy, there is a step in the slope parameter of the kaon spectra, and there is a peak (horn) in the  $K^+/\pi^+$  ratio. We will study all of these inclusive observables.

The observation of enhanced fluctuations would be the clearest evidence that the reaction trajectory of the cooling system had passed near the possible critical end point on the QGP/hadronic gas phase boundary. Recent analyses of the higher moments of the net-proton distributions have suggested the possibility of enhanced fluctuations at 7.7 GeV [81]. These results require higher statistics to improve the significance. It has also been shown in section 2.6 that the significance of the  $\kappa\sigma^2$  signal scales as  $\langle N_p^3 \rangle$ . An important test to determine if the enhanced fluctuations are related to critical behavior would be to see the fluctuation signals return to their baseline levels at energies below 7.7 GeV. The energies of the fixed-target program will provide these important control studies, allowing critical behavior searches to be extended to high  $\mu_B$  as was recently initiated by HADES at 2.42 GeV [93]. No critical fluctuation studies were performed at the AGS so the fixed target program will provide the first data in that energy regime.

The energy regime covered by the fixed-target program (3.0 to 7.7 GeV) should be optimal for the formation of matter (as opposed to anti-matter) hypernuclei. At energies below 3.0 GeV, few hyperons are produced, whereas at energies above 8 GeV, the increased production of anti-baryons stifles formation of composites of matter particles. Meaningful samples of  ${}^3_{\Lambda}\text{H}$  and  ${}^4_{\Lambda}\text{H}$  will be observed at all the fixed-target energies. The statistics are expected to be comparable to STAR data samples from  $\sqrt{s_{NN}} = 200$  GeV collider data; this will allow a precise measurement of the light hypernuclei lifetimes and a mapping of the  ${}^3_{\Lambda}\text{H}/({}^3\text{He} \times (\Lambda/p))$ , and  ${}^4_{\Lambda}\text{H}/({}^4\text{He} \times (\Lambda/p))$  ratios as a function of  $\sqrt{s_{NN}}$ . Searches for multi-strange hypernuclei

( ${}^5_{\Lambda\Lambda}\text{H}$  and  ${}^6_{\Lambda\Lambda}\text{He}$ ) make appealing physics goals. However, further simulations are required to determine if these measurements will be feasible with the expected integrated luminosity.

It will be possible to perform a high statistics analysis for signals associated with the CME in a region of the QCD phase-diagram with high baryon chemical potential ( $\mu_B \sim 721$  MeV) and where several other competing effects come in to play. These include whether a small portion of QGP is formed within the overlap volume even at these low energies?, whether the system is equilibrated?, or if it is fully in a mixed-phase that is expected by some theoretical descriptions of QCD matter at high  $\mu_B$ ? The properties of QCD matter at temperatures near or just below the deconfinement threshold are not well quantified. The STAR fixed target program is well positioned to perform a comprehensive study of this region of the QCD phase diagram. Because the magnetic field lifetime is inversely proportional to the collision energy, at top RHIC and LHC energies the B-field lifetime is shorter compared to fixed target collisions. After a successful test run with the fixed target at STAR in Au+Au and Al+Au collisions at  $\sqrt{s_{NN}} = 4.5$  and 4.9 GeV, respectively, in Run 18 STAR plans to acquire 100 million events in Au+Au collisions at  $\sqrt{s_{NN}} = 3.0$  GeV in only two days of beam time. At this energy the center-of-mass rapidity ( $y_{cm}$ ) is shifted forward by just over 1.0 units of rapidity. If no QGP is formed the charge separation signal from the CME will not persist.

### 3.4 FXT Beam Request

The FXT program at STAR will use energies that have already been developed for the BES-I program. Details of the sequence of energies is listed in the tables in the Executive Summary. Table 9 shows  $\sqrt{s_{NN}}$  set-up for the collider, the center of mass energy for FXT, the kinetic energy of the beam and the center of mass rapidity, as this gives insight to the acceptance of STAR for a given energy. Also list is the expected chemical potential to demonstrate the region of the QCD phase diagram to be studied.

In determining the required event statistics for the FXT program one needs to consider the various physics goals of the program, which include: directed flow, the width of rapidity distributions, HBT, elliptic flow, measurement of the Coulomb potential, higher moments analysis, and hypernuclei. Of these physics goals, the higher moments analysis will be the statistics driver. As has been mentioned previously, the significance of the  $\kappa\sigma^2$  observable varies with  $\langle N_p^3 \rangle$  (see section 2.6). From the 2015 test run data set at 4.5 GeV, we have demonstrated that the  $\langle N_p \rangle$  will be approximately the same as measured by STAR in central events at 11.5 GeV in collider mode. Therefore, with 100 million events we will achieve the same significance as proposed for the BES-II collider program. The mid-rapidity  $\langle N_p \rangle$  for central events varies as a function of collision energy as the rapidity of the center-of-mass shifts forward. For the lowest proposed energy, 3.0 GeV,  $y_{CM}$  is 1.05, which is well within the acceptance window for protons as seen in Fig. 45. For the highest energy proposed for the FXT program, 7.7 GeV,  $y_{CM}$  is 2.0, which is just beyond the acceptance of the upgraded detector, however enough protons will extend in the  $|y - y_{CM}| < 0.5$  analysis window to enable the net-proton  $\kappa\sigma^2$  analysis, with far more significant acceptance and efficiency corrections [95]. From previous measurements of the proton spectra and  $dN/dy$

**Table 9:** Collider set-up and fixed-target center-of-mass energies ( $\sqrt{s_{NN}}$ ), projectile kinetic energies (AGeV), center-of-mass rapidity offset ( $y_{CM}$ ) and baryon chemical potentials ( $\mu_B$ ) for the proposed fixed-target program.

Collider $\sqrt{s_{NN}}$	FXT $\sqrt{s_{NN}}$	Kinetic (AGeV)	Rapidity $y_{CM}$	$\mu_B$ (MeV)
62.4	7.7	30.3	2.10	420
39	6.2	18.6	1.87	487
27	5.2	12.6	1.68	541
19.6	4.5	8.9	1.52	589
14.5	3.9	6.3	1.37	633
11.5	3.5	4.8	1.25	666
9.1	3.2	3.6	1.13	699
7.7	3.0	2.9	1.05	721

yields, it can be demonstrated that the  $\langle N_p \rangle$  will exceed that of the BES-II collider program for energies below 4.5 GeV, and fall below that of the collider program above 4.5 GeV. We request 100 million events at each FXT energy in order to achieve similar significance of the physics observables as with the BES-II collider program, at least for the lower FXT energies. For the highest FXT energy, a far larger event sample would be needed to achieve similar physics significance, however as this is a redundant energy it is primarily motivated as a cross-check of the acceptance and efficiency corrections, both for the FXT and collider programs.

## 4 Detector Upgrades for Runs 19 and 20

For the BES-II program STAR have planned 3 upgrades: the inner Time Projection Chamber (iTPC), the Event Plane Detector (EPD) and the endcap Time of Flight (eTOF). The EPD was installed and became operational for Run 18. The EPD will replace the BBC as a minimum-bias trigger detector and will allow forward measurements of both centrality and event plane determination. The iTPC will increase the acceptance of the TPC, it will improve the  $dE/dx$  resolution, and will allow tracks to be reconstructed down to  $p_T$  of  $\sim 60$  MeV/ $c$ . A single inner sector was installed for Run 18 and the full complement of 24 will be installed for Run 19. The eTOF will be installed on one side of STAR, which will extend PID capabilities at forward rapidities. Three modules of eTOF were installed behind one of the TPC sectors for Run 18.

These upgrades are described in more detail below, and their overall location in the STAR detector is shown in Fig. 48.

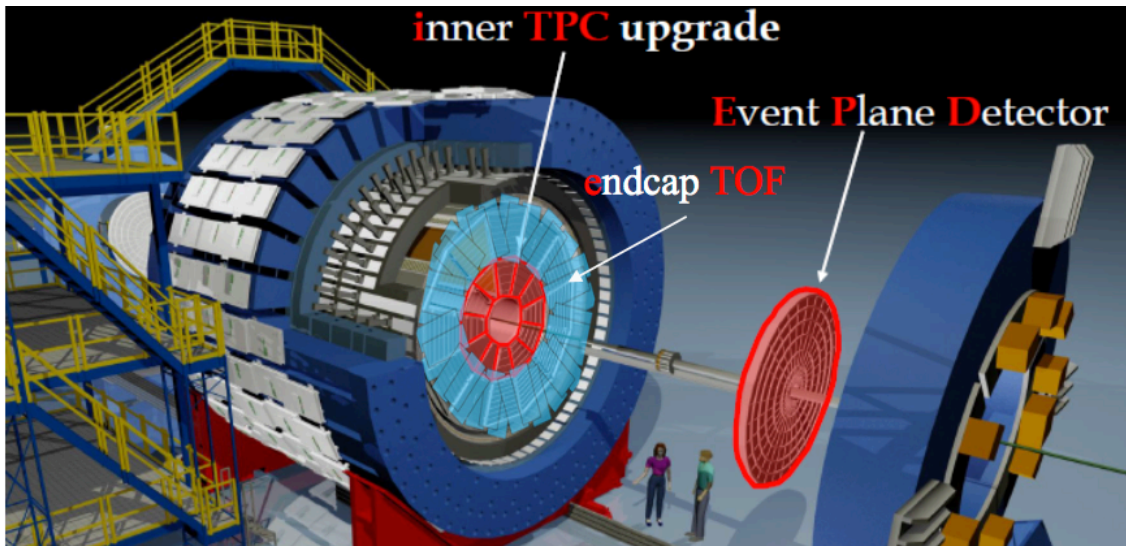


**Figure 48:** Rendering of the STAR detector with the upgrades highlighted in red. The EPD and iTPC are symmetric in STAR whereas the eTOF is only on the east side.

### 4.1 iTPC Upgrade

The inner sectors of the STAR TPC are being upgraded to increase the segmentation on the inner pad planes. These improvements will extend the capabilities of STAR in many ways. Most significantly, the enhanced tracking at small angles relative to the beamline will expand the TPC acceptance out to pseudorapidity  $|\eta| < 1.5$ , compared to the current limitation of  $|\eta| < 1$ . Furthermore, the detector will have better acceptance for tracks with low transverse momentum down to 60 MeV/ $c$ , as well as better resolution in both momentum ( $\delta p/p$  improvement  $\sim 15\%$ ) at larger momenta, and  $\sim 25\%$   $dE/dx$  improvement

of for full length tracks. The acceptance and the limit in  $p_T$  vs. rapidity for different species using PID from either the iTPC, bTOF or eTOF are show in Fig. 49.

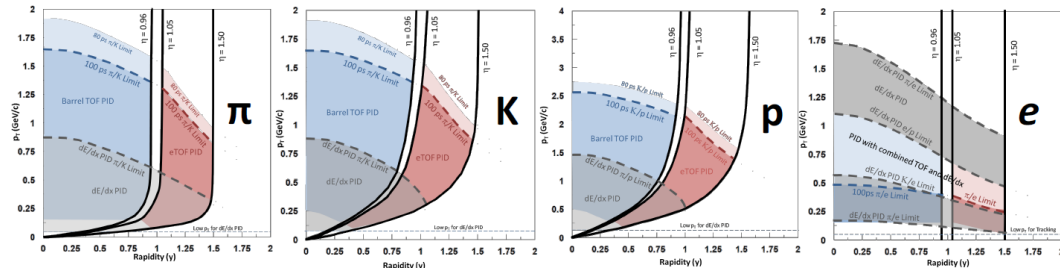


**Figure 49:** Acceptance and PID limits for  $\pi$ , K, proton and electrons with STAR instrumented with iTPC and eTOF.

These changes will enable the collection of data that are critical to the physics mission of the BES-II. In addition, the improved  $dE/dx$  and momentum resolution, as well as tracking at higher pseudorapidity, provide the foundation for the success of the eTOF. The iTPC project is described in detail in the Technical Design Report [46].



**Figure 50:** Installation platform with insertion tooling in the east end position in the 1006 assembly building.

A new fully tested iTPC sector was successfully installed on Oct. 5, 2017 into the STAR TPC for operation in RHIC Run 18. Replacement of a sector in the STAR TPC had never been attempted during the 18 years the detector has been taking data. Figure 50 shows the installation tool after it was moved onto the lift platform at the location of sector 20

where the new iTPC sector was installed. After the STAR detector was rolled back into the interaction region for Run 18, the newly installed iTPC sector was outfitted with electronics.

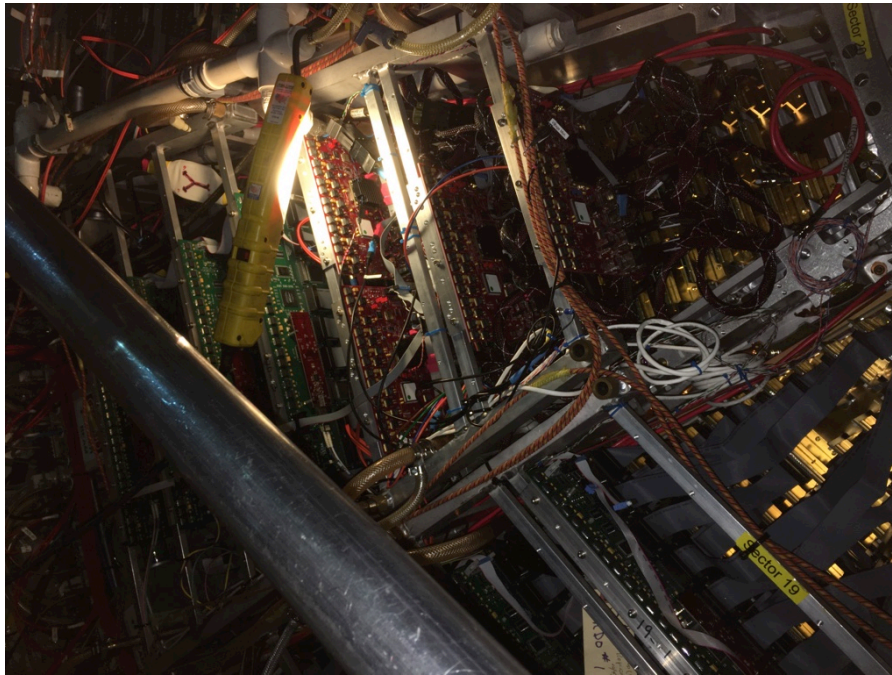


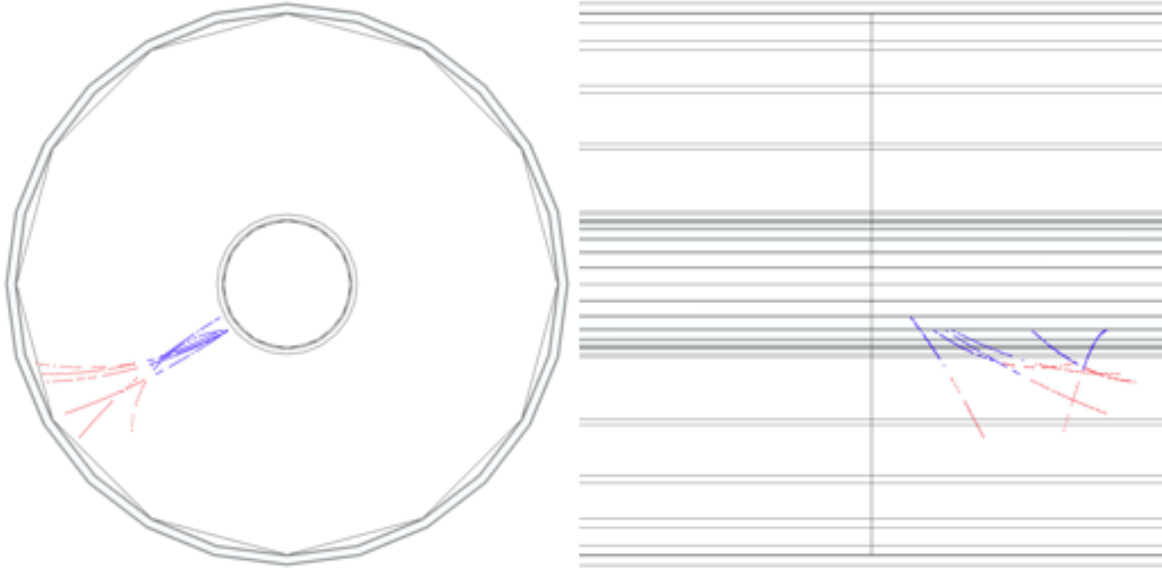
**Figure 51:** iTPC sector with electronics installed on TPC wheel.

The sector was fully tested for gain uniformity (better than 1%), current load, and vacuum at Shandong University Laboratory (SDU). At BNL it underwent further checks before installation. Extensive tests of the full electronics readout chain were performed in situ, while access to the location of the new sector was possible. After debugging was completed, successful readout of all 55 iFEE cards (99 % of the channels) on the upgraded iTPC sector was reported.

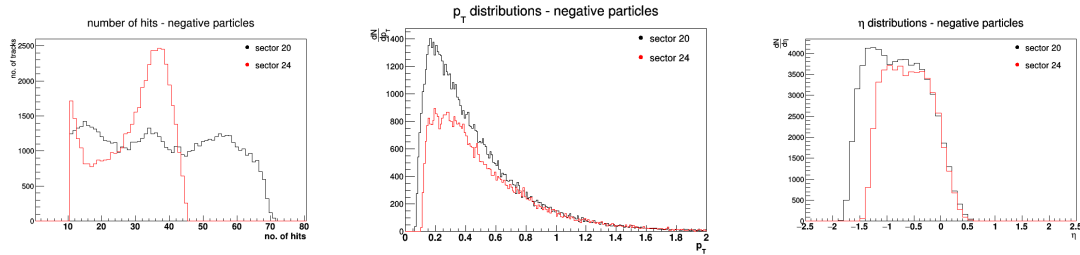
Further development of firmware for the iTPC and integration into the DAQ started during the cosmic ray running ahead of Run 18 and is ongoing. The iTPC is routinely included into the physics running, but taken out for updates and commissioning tasks. Analysis of data taken early in Run 18 is now underway with data from iTPC included in the tracking.

Figure 52 shows reconstructed tracks from one event in the 200 GeV isobar run. The tracks in other TPC sectors are suppressed. Figure 53 demonstrates the expected improvement with the iTPC: an increase from a maximum of 45 to 72 hits per track, a lower  $p_T$  threshold of 60 MeV/ $c$ , and an extended  $\eta$  coverage of about 0.4 units in the forward direction.

The production and testing of sectors is proceeding according to the schedule presented to the annual review of the iTPC in September 2017. The production at SDU is proceeding well, and as of mid-April 2018 18 production sectors have been completed. It is expected that construction and testing at SDU will be completed in July 2018. The production of electronics have started for RDOs and FEEs, following successful testing with cosmics and



**Figure 52:** Event display for reconstructed track in sector 20 only. The tracks in the iTPC are shown in blue while the track segments in the outer sector are shown in red. The left plot is an end view and the right a side view of the same event.



**Figure 53:** Comparison for reconstructed negative tracks in the iTPC (sector 20) with another TPC sector (sector 24) for left: number of hits per track, middle: raw  $p_T$  distribution, and right: raw  $dN/d\eta$  distribution.

in-beam.

The shutdown installation plan for all STAR activities has been worked out with the STAR chief mechanical engineer and calls for a 9 month shutdown period. The actual replacement of the inner sectors with the new iTPC sectors will start in August and be completed in December. It will be followed by about 2.5 months of regular pre-running STAR activities and commissioning of the iTPC using cosmics. A set of milestones in the current shutdown schedule are listed in Table 10 with the iTPC cosmic commissioning having an early finish on February 21, 2019. It should be stressed that the current schedule is tight and it is technically driven without float.

Activity	date
Shutdown period starts	6/18/2018
East side electronics stripped	7/20/2018
STAR rolled out	8/8/2018
Ready for East side installation	8/21/2018
East side installed	10/2/2018
Installation platform moved	10/19/2018
West side installed	11/27/2018
West side electronics installed	1/15/2019
Full system check	1/17/2019
Cosmic ray testing complete	2/21/2019

**Table 10:** Key activities and scheduled dates taken from the STAR operations schedule for all installation activities.

## 4.2 EPD Upgrade

A new, dedicated Event Plane, centrality, and trigger Detector (EPD) was installed in the forward direction of STAR in Run 18 as shown in Figure 54. This new detector has pseudorapidity acceptance of  $2.1 < |\eta| < 5.1$  with 16 radial segments and 24 azimuthal segments. The EPD allows both centrality and the event plane to be measured in the forward region, reducing the systematics due to autocorrelations for mid-rapidity analyses. The baseline detector design consisted of scintillator plastic, to form optically isolated tiles, wavelength-shifting fibers and silicon photomultipliers (SiPMs) as the read-out.

The EPD consists of two disks that are placed on either side of the STAR interaction region, in the current location of the Beam-Beam Counter (BBC) at  $z = \pm 375$  cm. The EPD is roughly the same size as BBC, as it was required to sit in the same space within the STAR experiment, but it is slightly closer to the beam pipe gaining an additional 0.1 of  $\eta$  in the very forward direction. The EPD extends from a radius of 4.5 cm to 90 cm. In 2018 the BBC small tiles were installed behind the EPD in order to calibrate the performance of the new detector. The EPD scintillator is 1.2 cm thick and has 12 azimuthal segments, spanning an angle of  $30^\circ$ , which we give the label “super-sector”. There are 16 segments in  $\eta$ , with the innermost tile spanning the entire super-sector, and the other tiles dividing it in two for better  $\phi$  resolution. This resulted in a total of 744 channels for the two EPD disks. The tile size was designed such that the probability of multiple particle hits in the same tile would be less than 10% at  $\sqrt{s_{NN}} = 19.6$  GeV, based on  $dN/d\eta$  measurements from PHOBOS. This increases to 65% for Au+Au collisions at 200 GeV. More details on the EPD design and expected performance can be found here [48]. Saturation of the signal can result if the 12-bit ADC input is larger than the maximum value of 4096, or the number of photons incident on the SiPM is more than  $\sim 25\%$  of the number of pixels illuminated (non-linear signal from either the FEEs or the ADCs could also cause saturation, however there is no evidence of this). From the 2017 commissioning run, we determined that there

is no saturation due to either effect for up to 4-MIP events. Scaling 200 GeV Au+Au data from PHOBOS by  $N_{part}$  indicates that the only tile that will have a significant number of 5+ MIP events is the innermost tile, indicating that saturation is not a problem for the highest energy isobar runs.

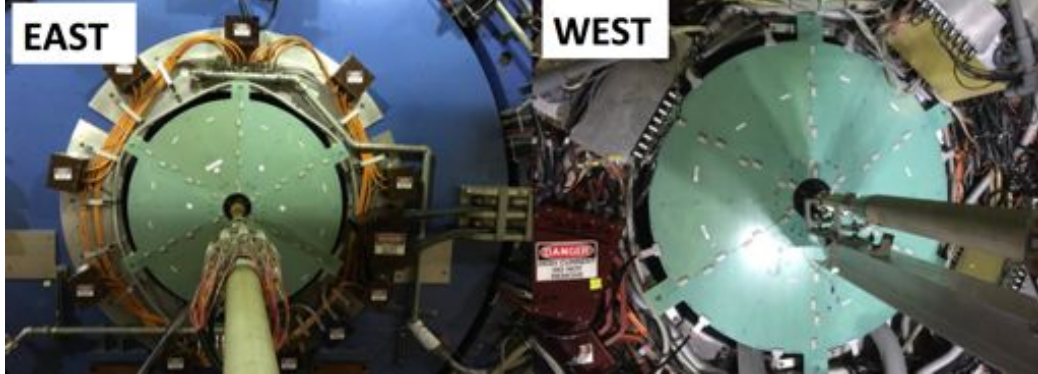


**Figure 54:** The EPD shown installed in STAR in preparation for the 2018 Run. The EPD strongback is divided into sextants, each of which hold two supersectors.

For Run 18, the EPD has signal in all 744 of its tiles. The detector was timed in and the bias voltages were set within the first day of operations so that the data from the EPD can be incorporated into all physics analyses from Run 18. The performance of the EPD tiles is extremely uniform, in Figure 55, the ADC spectra for the innermost tile (tile 1) is shown for all twelve tiles in the east side. There is no additional normalization applied to these distributions, the agreement between them is very good. The full ADC spectra for a single tile and in relationship to the TAC is also shown in this figure.

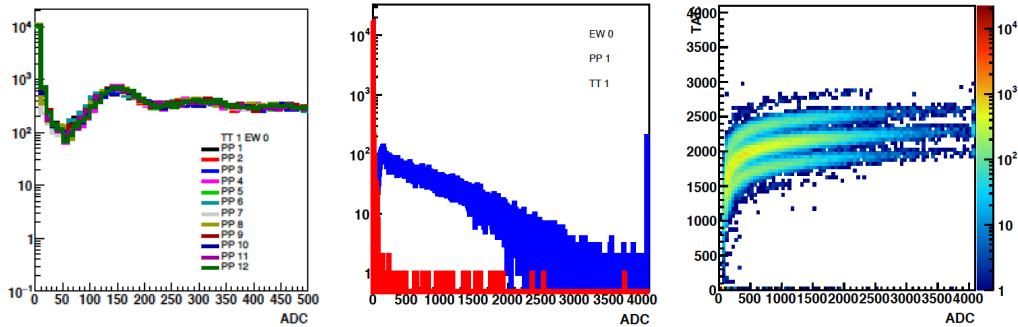


**Figure 55:** (left) ADC spectra for all twelve innermost tiles (tile 1) on the east side. There is no additional normalization in this plot. (middle) The full ADC spectrum for a single inner tile. The blue distribution is the ADC spectrum for in-time hits. The red distribution is the ADC spectrum from out-of-time hits. The level of saturation shown is not large. (right) The distribution of the ADC versus the TAC distribution for tile one. The beam satellites can clearly be seen.

The EPD ADC can be calibrated by dividing the ADC in a given tile by the ADC value of the single MIP peak. This will not yield a direct particle multiplicity, but will put the outer tiles and inner tiles on equal footing. The sum of the calibrated EPD sum compared

to the sum ADC from the BBC on the east side is shown in Figure 56. The correlation is strong, indicating that the timing of the EPD was set properly and that they are measuring the same events. In previous years, the centrality determination in STAR was made by measuring the multiplicity in the TPC in the acceptance  $|\eta| < 0.5$ , which was defined as the RefMult. In order for the EPD centrality to be utilized in the same fashion, the correlation with the TPC must be strong. This is shown in Figure 56. It should be noted that for this figure no cuts were applied to remove pile-up contamination. Pile-up affects the slowly drifting TPC but not the EPD, and is likely the cause of the stripes seen at TPC RefMult  $\sim 0$  and EPD MipSum  $\sim 0$ . A more detailed analysis will be used to remove these events and/or select the proper vertex, in the future. However, what is important is that the EPD multiplicity shows a linear response with the TPC multiplicity, indicating its suitability as a centrality detector.

A preliminary analysis of the second order event plane is shown in Figure 57. For this analysis, a rough centrality selection was used to select semi-central events. With no corrections to the distributions a clear correlation between the east and west second order event plane can be seen, indicating that the EPD is performing well. Also shown in this figure is a preliminary look at the event plane resolution, determined by comparing the east versus west event plane and using  $\phi$  reweighting to flatten the event plane itself.

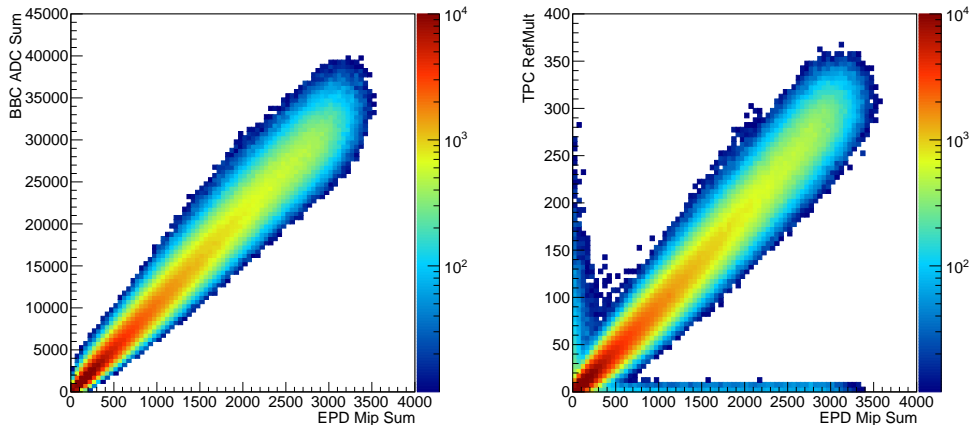


**Figure 56:** (left) The calibrated ADC for the EPD versus the sum ADC for the BBC on the east side. The nice correlation verifies that the EPD timing is set properly, and that both are measuring the same event multiplicities. (right) The calibrated ADC for the EPD versus the RefMult measured by the TPC.

In future runs, the EPD will be used as a trigger detector. This will require that it perform at least as well as the BBC. Some EPD timing information can be seen in Figure 58. The timing difference between east and west EPD can be seen in TAC. A determination of the resolution for using a single tile, chosen to be the fastest on the East and on the West after a rough slewing correction is 0.75 ns. Using the average timing of all the tiles improves the resolution to 0.39 ns. Further improvement in the timing resolution may be possible with an improved slewing correction and final calibrations.

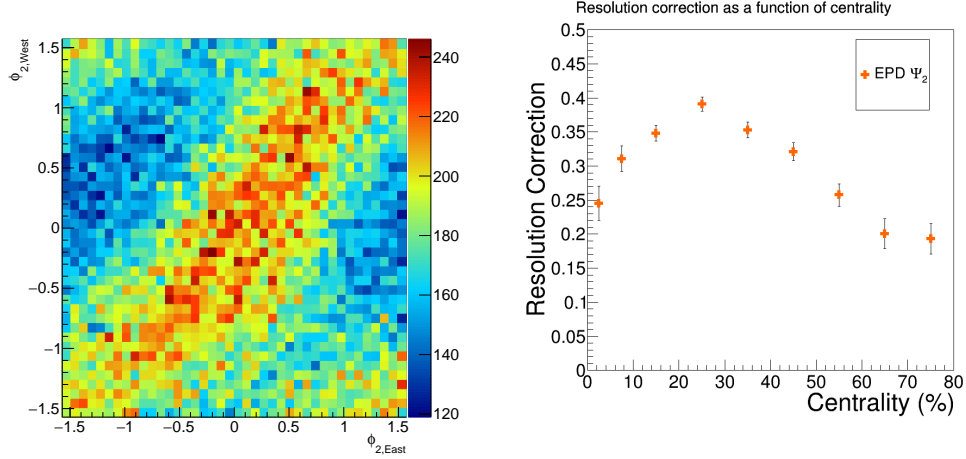


**Figure 57:** (Left) The second order event plane as measured in the EPD East versus the EPD West in 2018 without any additional corrections. The fixed target installation causes an anisotropy which will be corrected. (Right) An estimate of the second order event plane resolution at top energy Zr+Zr/Ru+Ru after  $\phi$  reweighting to flatten the event plane plane.

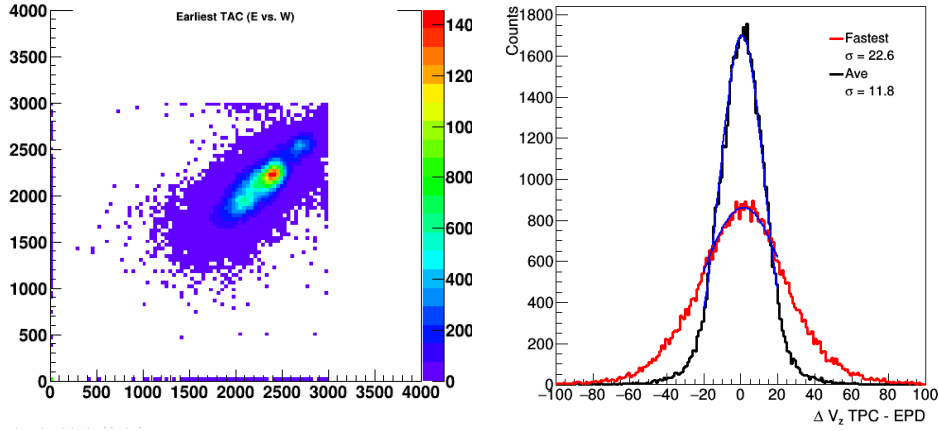


**Figure 58:** On the left is the distribution of the EPD earliest TAC versus the BBC earliest TAC. On the right is the difference in  $V_z$  between the vertex found using tracks in the TPC, which has a very good resolution, compared to the vertex found by the EPD. In red is the difference between the vertex found by the fastest signal on the east versus the west, in black is the difference between the average timing difference east versus west.

The EPD has performed well in Run 18, indicating that it will be an important upgrade for both Run 19 and Run 20. There is a well defined MIP peak in all channels and the detector has been shown to be in time with the rest of STAR. Preliminary studies show an event plane resolution at top energy of 0.4 in 20 - 30% events and a timing resolution is 0.75 ns, if one uses only a single tile, which can be improved to 0.39 ns by averaging the signals from all tiles. Work is ongoing to finalize these results.

### 4.3 eTOF Upgrade

The STAR Collaboration and institutions from the CBM Collaboration: Heidelberg, Darmstadt, Tsinghua, CCNU, and USTC have agreed to install an endcap time-of-flight upgrade (eTOF) in the STAR detector for the BES-II program. The eTOF will be installed at the east end of STAR in the small gap between the poletip and the TPC; behind the readout electronics as depicted in the left cartoon of Fig. 59. The right hand side of the same figure illustrates how the coverage in  $\eta$  is much improved with the combination of the iTPC and the eTOF (confirm also Fig. 49). The improvements in acceptance and PID and the physics goals of the upgrade are described in detail in Ref. [47]. The eTOF upgrade is part of the FAIR Phase 0 program.

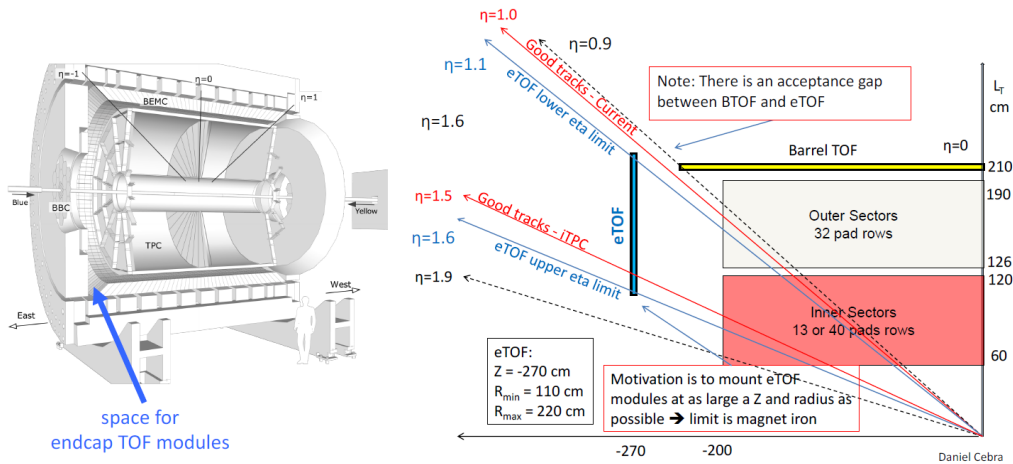


**Figure 59:** Placement and acceptance diagrams for the eTOF.

The eTOF upgrade comprises the installation, commissioning and operation of 36 CBM TOF modules arranged in 12 sectors (see Figure 60) matching the TPC sectors. Each module

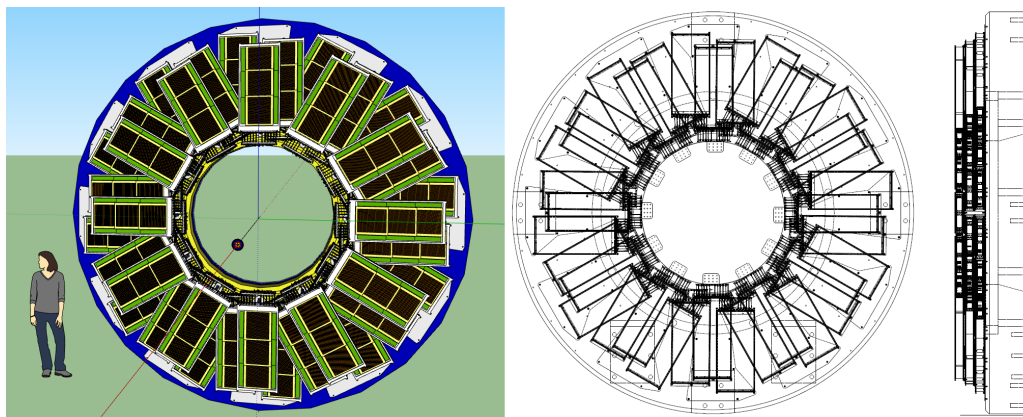


**Figure 60:** eTOF wheel with 36 CBM TOF modules arranged in 12 sectors. Left: illustration with visible MRPC counters, Right: technical drawing.

consists of 3 Multi-gap Resistive Plate Counters (MRPCs) with a 32 strip segmented read out electrode. In order to get a position resolution below 5 mm along the strip, the strip is read out from both sides. Thus, a total of 6912 readout channels build up the eTOF wheel. Each MRPC has an active area of 27 cm  $\times$  32 cm and a strip pitch of 1 cm. Across the strip a position resolution of 2.5 mm was demonstrated in cosmic tests. The eTOF wall will contain 2 types of MRPCs. 36 out of 108 counters have 0.7 mm thick low resistive glass as electrode material which makes them high rate capable. 72 MRPCs have normal float glass with a thickness of 0.28 mm as electrode material. Both counter types are full size prototypes for the CBM experiment and are described in detail in Ref [112].

One eTOF sector was installed behind TPC sector 18 for the ongoing Run 18 with the aim of testing the functionality of the modules with two different counter types in the RHIC environment, and integrating the CBM readout with the STAR trigger and DAQ systems. Figure 61 (left side) shows the sector mounted at the 6 o'clock position. The right side shows the simulated  $\eta\phi$  hit distribution of one sector. The modules are aligned at the mechanically smallest possible value of  $\eta = 1.1$  in order to close the gap to the barrel TOF as much as possible. In red are highlighted the overlap region to the neighbor sectors at higher  $\eta$  and the acceptance gap at lower  $\eta$ . The purple arrow indicates the border of good iTPC tracks. The

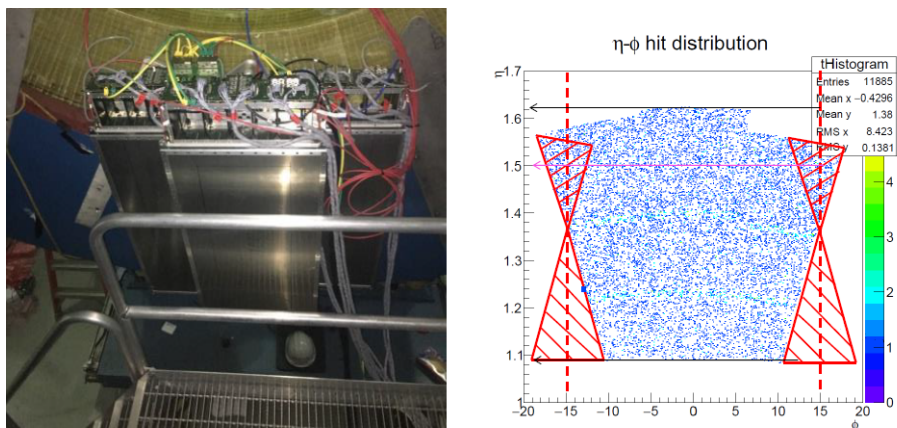


**Figure 61:** Left side: One sector installed for Run 18. Right side:  $\eta\phi$  hit distribution of one sector simulated with CBM-ROOT

real  $\eta\phi$  hit distribution was measured with beam and is depicted in Fig. 62. It demonstrates that the counter and the readout is working. Since the counter inside the module have an overlap of two strips a signal is generated on both MRPCs in this overlapping region. Thus, from these hits a system time resolution can be derived which amounts to 83 ps as depicted on the right side of Figure 62.

The mass production of the MRPC counters started at the end of 2017 and is ongoing in China until July 2018. The integration into the modules, which will take place in Heidelberg, will start in May 2018 and will continue till August. In parallel all the modules will be tested extensively with cosmic rays to ensure their functionality. The shipment of all modules to BNL is planned for October 2018. The installation of the eTOF infrastructure (gas

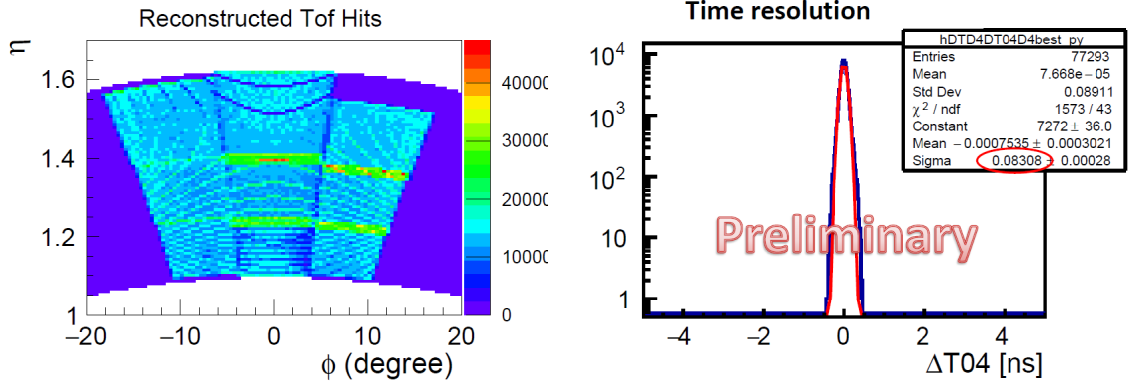


**Figure 62:** Left side:  $\eta\phi$  hit distribution obtained from data taken in Run 18. Right side: preliminary system time resolution of 83 ps between two MRPCs in their overlapping region.

distribution panel, HV distribution, mounting plates, rack) can start much earlier, i.e. after the roll-out (probably in August) of the STAR detector. The installation and commissioning of the full eTOF wheel is foreseen for the beginning of November. After the roll-in the full data acquisition and integration into the STAR environment will be commissioned. It is planned for the eTOF to be ready for beam by mid-February.

## References

- [1] Ani Aprahamian et al. Reaching for the horizon: The 2015 long range plan for nuclear science. 2015.
- [2] STAR. SN0669 - The STAR midrapidity pp, pA, AA physics program beyond BES-II.
- [3] STAR. SN0648 - The STAR Forward Calorimeter System and Forward Tracking System beyond BES-II.
- [4] Leszek Adamczyk et al. Azimuthal transverse single-spin asymmetries of inclusive jets and charged pions within jets from polarized-proton collisions at  $\sqrt{s} = 500$  GeV. *Phys. Rev. D*, 97(3):032004, 2018.
- [5] Leszek Adamczyk et al. Transverse spin-dependent azimuthal correlations of charged pion pairs measured in  $p^\uparrow + p$  collisions at  $\sqrt{s} = 500$  GeV. *Phys. Lett. B*, 780:332–339, 2018.
- [6] A. Airapetian et al. Single-spin asymmetries in semi-inclusive deep-inelastic scattering on a transversely polarized hydrogen target. *Phys. Rev. Lett.*, 94:012002, 2005.
- [7] C. Adolph et al. Collins and Sivers asymmetries in muonproduction of pions and kaons off transversely polarised protons. *Phys. Lett.*, B744:250–259, 2015.
- [8] X. Qian et al. Single Spin Asymmetries in Charged Pion Production from Semi-Inclusive Deep Inelastic Scattering on a Transversely Polarized  $^3\text{He}$  Target. *Phys. Rev. Lett.*, 107:072003, 2011.
- [9] Daniel Boer, Rainer Jakob, and Marco Radici. Interference fragmentation functions in electron positron annihilation. *Phys. Rev.*, D67:094003, 2003.
- [10] R. L. Jaffe, Xue-min Jin, and Jian Tang. Interference fragmentation functions and the nucleon’s transversity. *Phys. Rev. Lett.*, 80:1166–1169, 1998.
- [11] A. Bianconi, S. Boffi, R. Jakob, and M. Radici. Two hadron interference fragmentation functions. Part 2. A Model calculation. *Phys. Rev.*, D62:034009, 2000.
- [12] John C. Collins. Fragmentation of transversely polarized quarks probed in transverse momentum distributions. *Nucl. Phys.*, B396:161–182, 1993.
- [13] Umberto D’Alesio, Francesco Murgia, and Cristian Pisano. Testing the universality of the Collins function in pion-jet production at RHIC. *Phys. Lett.*, B773:300–306, 2017.
- [14] Zhong-Bo Kang, Alexei Prokudin, Felix Ringer, and Feng Yuan. Collins azimuthal asymmetries of hadron production inside jets. *Phys. Lett.*, B774:635–642, 2017.

- [15] Marco Radici, Alessandro M. Ricci, Alessandro Bacchetta, and Asmita Mukherjee. Exploring universality of transversity in proton-proton collisions. *Phys. Rev.*, D94(3):034012, 2016.
- [16] L. Adamczyk et al. Observation of Transverse Spin-Dependent Azimuthal Correlations of Charged Pion Pairs in  $p^\uparrow + p$  at  $\sqrt{s} = 200$  GeV. *Phys. Rev. Lett.*, 115:242501, 2015.
- [17] L. Adamczyk et al. Longitudinal and transverse spin asymmetries for inclusive jet production at mid-rapidity in polarized  $p + p$  collisions at  $\sqrt{s} = 200$  GeV. *Phys. Rev.*, D86:032006, 2012.
- [18] Amilkar Quintero. Measurement of the Longitudinal Double-Spin Asymmetry for Inclusive Jet Production in Polarized Proton Collisions at  $\sqrt{s} = 510$  GeV. Poster at RHIC & AGS Annual Users' Meeting.
- [19] Daniel L. Olivitt Jr. Probing  $\Delta g(x)$  Through Dijet Production in Polarized  $p + p$  Collisions. Poster at RHIC & AGS Annual Users' Meeting.
- [20] J. Adam et al. Longitudinal Double-Spin Asymmetries for Dijet Production at Intermediate Pseudorapidity in Polarized  $pp$  Collisions at  $\sqrt{s} = 200$  GeV. *To be submitted to Phys. Rev. D.*
- [21] J. Adam et al. Longitudinal Double-Spin Asymmetries for  $\pi^0$ s in the Forward Direction for 510 GeV Polarized  $pp$  Collisions. *To be submitted to Phys. Rev. D.*
- [22] Daniel de Florian, Rodolfo Sassot, Marco Stratmann, and Werner Vogelsang. Evidence for polarization of gluons in the proton. *Phys. Rev. Lett.*, 113(1):012001, 2014.
- [23] Emanuele R. Nocera, Richard D. Ball, Stefano Forte, Giovanni Ridolfi, and Juan Rojo. A first unbiased global determination of polarized PDFs and their uncertainties. *Nucl. Phys.*, B887:276–308, 2014.
- [24] L. Adamczyk et al. Measurement of the transverse single-spin asymmetry in  $p^\uparrow + p \rightarrow W^\pm/Z^0$  at RHIC. *Phys. Rev. Lett.*, 116(13):132301, 2016.
- [25] L. Adamczyk et al. Measurement of  $D^0$  Azimuthal Anisotropy at Midrapidity in Au+Au Collisions at  $\sqrt{s_{NN}}=200$  GeV. *Phys. Rev. Lett.*, 118(21):212301, 2017.
- [26] Sandeep Chatterjee and Piotr Bożek. Large directed flow of open charm mesons probes the three dimensional distribution of matter in heavy ion collisions. 2017.
- [27] L. Adamczyk et al. Beam-Energy Dependence of Directed Flow of  $\Lambda$ ,  $\bar{\Lambda}$ ,  $K^\pm$ ,  $K_s^0$  and  $\phi$  in Au+Au Collisions. *Phys. Rev. Lett.*, 120(6):062301, 2018.
- [28] Sergei A. Voloshin, Arthur M. Poskanzer, and Raimond Snellings. Collective phenomena in non-central nuclear collisions. *Landolt-Bornstein*, 23:293–333, 2010.

- [29] Jianguyong Jia, Mingliang Zhou, and Adam Trzupek. Revealing long-range multi-particle collectivity in small collision systems via subevent cumulants. *Phys. Rev.*, C96(3):034906, 2017.
- [30] Morad Aaboud et al. Measurement of long-range multiparticle azimuthal correlations with the subevent cumulant method in  $pp$  and  $p + Pb$  collisions with the ATLAS detector at the CERN Large Hadron Collider. *Phys. Rev.*, C97(2):024904, 2018.
- [31] Charles Gale, Sangyong Jeon, Björn Schenke, Prithwish Tribedy, and Raju Venugopalan. Event-by-event anisotropic flow in heavy-ion collisions from combined Yang-Mills and viscous fluid dynamics. *Phys. Rev. Lett.*, 110(1):012302, 2013.
- [32] Morad Aaboud et al. Measurement of longitudinal flow decorrelations in Pb+Pb collisions at  $\sqrt{s_{NN}} = 2.76$  and 5.02 TeV with the ATLAS detector. *Eur. Phys. J.*, C78(2):142, 2018.
- [33] Long-Gang Pang, Hannah Petersen, Guang-You Qin, Victor Roy, and Xin-Nian Wang. Decorrelation of anisotropic flow along the longitudinal direction. *Eur. Phys. J.*, A52(4):97, 2016.
- [34] Liang Z.-T. and X.-N. Wang. Globally polarized quark-gluon plasma in noncentral A+A collisions. *Phys. Rev. Lett.*, 94:102301, 2005.
- [35] F. Becattini, F. Piccinini, and J. Rizzo. Angular momentum conservation in heavy ion collisions at very high energy. *Phys. Rev.*, C77:024906, 2008.
- [36] I. Karpenko and F. Becattini. Study of  $\Lambda$  polarization in relativistic nuclear collisions at  $\sqrt{s_{NN}} = 7.7 - 200$  GeV. *Eur. Phys. J.*, C77(4):213, 2017.
- [37] Hui Li, Long-Gang Pang, Qun Wang, and Xiao-Liang Xia. Global  $\Lambda$  polarization in heavy-ion collisions from a transport model. *Phys. Rev.*, C96(5):054908, 2017.
- [38] L. Adamczyk et al. Global  $\Lambda$  hyperon polarization in nuclear collisions: evidence for the most vortical fluid. *Nature*, 548:62–65, 2017.
- [39] Vardan Khachatryan et al. Observation of charge-dependent azimuthal correlations in pPb collisions and its implication for the search for the chiral magnetic effect. *Phys. Rev. Lett.*, 2016. [Phys. Rev. Lett.118,122301(2017)].
- [40] Albert M Sirunyan et al. Constraints on the chiral magnetic effect using charge-dependent azimuthal correlations in pPb and PbPb collisions at the LHC. 2017.
- [41] R. Belmont and J. L. Nagle. To CME or not to CME? Implications of p+Pb measurements of the chiral magnetic effect in heavy ion collisions. *Phys. Rev.*, C96(2):024901, 2017.

- [42] A. Adare et al. Transverse energy production and charged-particle multiplicity at midrapidity in various systems from  $\sqrt{s_{NN}} = 7.7$  to 200 GeV. *Phys. Rev.*, C93(2):024901, 2016.
- [43] L. Adamczyk et al. Di-Jet Imbalance Measurements at  $\sqrt{s_{NN}} = 200$  GeV at STAR. 2016.
- [44] L. Adamczyk et al. Measurements of jet quenching with semi-inclusive hadron+jet distributions in Au+Au collisions at  $\sqrt{s_{NN}} = 200$  GeV. 2017.
- [45] STAR. SN0598- Studying the Phase Diagram of QCD Matter at RHIC. March 2014. STAR Note SN0598.
- [46] STAR. SN0644 - Technical Design Report for the iTPC Upgrade.
- [47] Physics Program for the STAR/CBM eTOF Upgrade. 2016.
- [48] STAR. SN0666 - An Event Plane Detector for STAR.
- [49] D. H. Rischke et al. The Phase transition to the quark-gluon plasma and its effects on hydrodynamic flow. *Heavy Ion Phys.*, 1:309–322, 1995.
- [50] J. Brachmann, S. Soff, A. Dumitru, Horst Stoecker, J. A. Maruhn, W. Greiner, L. V. Bravina, and D. H. Rischke. Antiflow of nucleons at the softest point of the EoS. *Phys. Rev.*, C61:024909, 2000.
- [51] H. Stöcker. Collective flow signals the quark-gluon plasma. *Nucl. Phys.*, A750:121–147, 2005.
- [52] L. Adamczyk et al. Beam-Energy Dependence of the Directed Flow of Protons, Antiprotons, and Pions in Au+Au Collisions. *Phys. Rev. Lett.*, 112(16):162301, 2014.
- [53] Yasushi Nara, Harri Niemi, Jan Steinheimer, and Horst Stöcker. Equation of state dependence of directed flow in a microscopic transport model. *Phys. Lett.*, B769:543–548, 2017.
- [54] J. Steinheimer, J. Auvinen, H. Petersen, M. Bleicher, and H. Stöcker. Examination of directed flow as a signal for a phase transition in relativistic nuclear collisions. *Phys. Rev.*, C89(5):054913, 2014.
- [55] V. P. Konchakovski, W. Cassing, Yu. B. Ivanov, and V. D. Toneev. Examination of the directed flow puzzle in heavy-ion collisions. *Phys. Rev.*, C90(1):014903, 2014.
- [56] W. Cassing, V. P. Konchakovski, A. Palmese, V. D. Toneev, and E. L. Bratkovskaya. Parton/hadron dynamics in heavy-ion collisions at FAIR energies. *EPJ Web Conf.*, 95:01004, 2015.

- [57] Yu. B. Ivanov and A. A. Soldatov. Directed flow indicates a cross-over deconfinement transition in relativistic nuclear collisions. *Phys. Rev.*, C91(2):024915, 2015.
- [58] Yasushi Nara, Harri Niemi, Akira Ohnishi, and Horst Stöcker. Examination of directed flow as a signature of the softest point of the equation of state in QCD matter. *Phys. Rev.*, C94(3):034906, 2016.
- [59] Yasushi Nara, Harri Niemi, Akira Ohnishi, Jan Steinheimer, Xiaofeng Luo, and Horst Stöcker. Enhancement of elliptic flow can signal a first order phase transition in high energy heavy ion collisions. *Eur. Phys. J.*, A54(2):18, 2018.
- [60] Subhash Singha, Prashanth Shanmuganathan, and Declan Keane. The first moment of azimuthal anisotropy in nuclear collisions from AGS to LHC energies. *Adv. High Energy Phys.*, 2016:2836989, 2016.
- [61] J. C. Dunlop, M. A. Lisa, and P. Sorensen. Constituent quark scaling violation due to baryon number transport. *Phys. Rev.*, C84:044914, 2011.
- [62] R. Takahashi, M. Matsuo, M. Ono, K. Harii, H. Chudo, S. Okayasu, J. Ieda, S. Takahashi, S. Maekawa, and E. Saitoh. Spin hydrodynamic generation. *Nature Physics*, 12:52–56, 2016.
- [63] V. Skokov, A. Yu. Illarionov, and V. Toneev. Estimate of the magnetic field strength in heavy-ion collisions. *Int. J. Mod. Phys.*, A24:5925–5932, 2009.
- [64] F. Becattini, I. Karpenko, M. Lisa, I. Upsal, and S. Voloshin. Global hyperon polarization at local thermodynamic equilibrium with vorticity, magnetic field and feed-down. *Phys. Rev.*, C95(5):054902, 2017.
- [65] B. I. Abelev et al. Global polarization measurement in Au+Au collisions. *Phys. Rev.*, C76:024915, 2007. [Erratum: *Phys. Rev.* C95, no.3, 039906 (2017)].
- [66] R. Rapp. Signatures of thermal dilepton radiation at RHIC. *Phys. Rev.*, C63:054907, 2001.
- [67] Ralf Rapp and Hendrik van Hees. Thermal Dileptons as Fireball Thermometer and Chronometer. *Phys. Lett.*, B753:586–590, 2016.
- [68] Paul M. Hohler and Ralf Rapp. Is  $\rho$ -Meson Melting Compatible with Chiral Restoration? *Phys. Lett.*, B731:103–109, 2014.
- [69] N. Brambilla et al. Heavy quarkonium: progress, puzzles, and opportunities. *Eur. Phys. J.*, C71:1534, 2011.
- [70] B. Mohanty and N. Xu. Probe the QCD phase diagram with phi-mesons in high energy nuclear collisions. *J. Phys.*, G36:064022, 2009.

- [71] Md. Nasim, Bedangadas Mohanty, and Nu Xu. Elliptic flow of  $\phi$  mesons as a sensitive probe for the onset of the deconfinement transition in high energy heavy-ion collisions. *Phys. Rev.*, C87(1):014903, 2013.
- [72] B. I. Abelev et al. Energy and system size dependence of phi meson production in Cu+Cu and Au+Au collisions. *Phys. Lett.*, B673:183–191, 2009.
- [73] Y. Aoki, Z. Fodor, S. D. Katz, and K. K. Szabo. The QCD transition temperature: Results with physical masses in the continuum limit. *Phys. Lett.*, B643:46–54, 2006.
- [74] Y. Aoki, G. Endrodi, Z. Fodor, S. D. Katz, and K. K. Szabo. The Order of the quantum chromodynamics transition predicted by the standard model of particle physics. *Nature*, 443:675–678, 2006.
- [75] M. A. Stephanov. Non-Gaussian fluctuations near the QCD critical point. *Phys. Rev. Lett.*, 102:032301, 2009.
- [76] Masayuki Asakawa, Shinji Ejiri, and Masakiyo Kitazawa. Third moments of conserved charges as probes of QCD phase structure. *Phys. Rev. Lett.*, 103:262301, 2009.
- [77] M. A. Stephanov. On the sign of kurtosis near the QCD critical point. *Phys. Rev. Lett.*, 107:052301, 2011.
- [78] M. Cheng et al. Baryon Number, Strangeness and Electric Charge Fluctuations in QCD at High Temperature. *Phys. Rev.*, D79:074505, 2009.
- [79] R. V. Gavai and Sourendu Gupta. Lattice QCD predictions for shapes of event distributions along the freezeout curve in heavy-ion collisions. *Phys. Lett.*, B696:459–463, 2011.
- [80] Sourendu Gupta, Xiaofeng Luo, Bedangadas Mohanty, Hans Georg Ritter, and Nu Xu. Scale for the Phase Diagram of Quantum Chromodynamics. *Science*, 332:1525–1528, 2011.
- [81] L. Adamczyk et al. Energy Dependence of Moments of Net-proton Multiplicity Distributions at RHIC. *Phys. Rev. Lett.*, 112:032302, 2014.
- [82] Amal Sarkar. Higher-moment measurements of net-kaon, net-charge and net-proton multiplicity distributions at STAR. *Nucl. Phys.*, A931:796–801, 2014.
- [83] L. Adamczyk et al. Beam energy dependence of moments of the net-charge multiplicity distributions in Au+Au collisions at RHIC. *Phys. Rev. Lett.*, 113:092301, 2014.
- [84] P. Garg, D. K. Mishra, P. K. Netrakanti, B. Mohanty, A. K. Mohanty, B. K. Singh, and N. Xu. Conserved number fluctuations in a hadron resonance gas model. *Phys. Lett.*, B726:691–696, 2013.

- [85] Saumen Datta, Rajiv V. Gavai, and Sourendu Gupta. The QCD Critical Point : marching towards continuum. *Nucl. Phys.*, A904-905:883c–886c, 2013.
- [86] Z. Fodor and S. D. Katz. Critical point of QCD at finite T and mu, lattice results for physical quark masses. *JHEP*, 04:050, 2004.
- [87] A. Bazavov et al. The QCD Equation of State to  $\mathcal{O}(\mu_B^6)$  from Lattice QCD. *Phys. Rev.*, D95(5):054504, 2017.
- [88] Eduardo S. Fraga, Leticia F. Palhares, and Paul Sorensen. Finite-size scaling as a tool in the search for the QCD critical point in heavy ion data. *Phys. Rev.*, C84:011903, 2011.
- [89] R. Bellwied, S. Borsanyi, Z. Fodor, J. Günther, S. D. Katz, C. Ratti, and K. K. Szabo. The QCD phase diagram from analytic continuation. *Phys. Lett.*, B751:559–564, 2015.
- [90] Xian-yin Xin, Si-xue Qin, and Yu-xin Liu. Quark number fluctuations at finite temperature and finite chemical potential via the Dyson-Schwinger equation approach. *Phys. Rev.*, D90(7):076006, 2014.
- [91] Christian S. Fischer, Jan Luecker, and Christian A. Welzbacher. Phase structure of three and four flavor QCD. *Phys. Rev.*, D90(3):034022, 2014.
- [92] Renato Critelli, Jorge Noronha, Jacquelyn Noronha-Hostler, Israel Portillo, Claudia Ratti, and Romulo Rougemont. Critical point in the phase diagram of primordial quark-gluon matter from black hole physics. *Phys. Rev.*, D96(9):096026, 2017.
- [93] Manuel Lorenz. Overview of recent results from HADES. *Nucl. Phys.*, A967:27–34, 2017.
- [94] Xiaofeng Luo. Energy Dependence of Moments of Net-Proton and Net-Charge Multiplicity Distributions at STAR. *PoS*, CPOD2014:019, 2015.
- [95] A. Bzdak, V. Koch, V. Skokov, and N. Strodthoff. Cumulants vs correlation functions and the QCD phase diagram at low energies. *Nucl. Phys.*, A967:465–467, 2017.
- [96] Jan Steinheimer and Jorgen Randrup. Spinodal amplification of density fluctuations in fluid-dynamical simulations of relativistic nuclear collisions. *Phys. Rev. Lett.*, 109:212301, 2012.
- [97] C. Alt et al. Pion and kaon production in central Pb + Pb collisions at 20-A and 30-A-GeV: Evidence for the onset of deconfinement. *Phys. Rev.*, C77:024903, 2008.
- [98] J. L. Klay et al. Charged pion production in 2 to 8 A GeV central Au+Au collisions. *Phys. Rev.*, C68:054905, 2003.
- [99] L. Ahle et al. Particle production at high baryon density in central Au + Au reactions at 11.6-A-GeV/c. *Phys. Rev.*, C57:466–470, 1998.

- [100] J. Barrette et al. Proton and pion production in Au + Au collisions at 10.8A-GeV/c. *Phys. Rev.*, C62:024901, 2000.
- [101] H. Liu et al. Sideward flow in Au + Au collisions between 2-A-GeV and 8-A-GeV. *Phys. Rev. Lett.*, 84:5488–5492, 2000.
- [102] Hannah Petersen and Marcus Bleicher. Longitudinal flow and onset of deconfinement. *PoS*, CPOD2006:025, 2006.
- [103] Michael Annan Lisa, Ulrich W. Heinz, and Urs Achim Wiedemann. Tilted pion sources from azimuthally sensitive HBT interferometry. *Phys. Lett.*, B489:287–292, 2000.
- [104] M. A. Lisa et al. Azimuthal dependence of pion interferometry at the AGS. *Phys. Lett.*, B496:1–8, 2000.
- [105] M. A. Lisa, E. Frodermann, G. Graef, M. Mitrovski, E. Mount, H. Petersen, and M. Bleicher. Shape analysis of strongly-interacting systems: The Heavy ion case. *New J. Phys.*, 13:065006, 2011.
- [106] Michael Annan Lisa, Scott Pratt, Ron Soltz, and Urs Wiedemann. Femtoscopy in relativistic heavy ion collisions. *Ann. Rev. Nucl. Part. Sci.*, 55:357–402, 2005.
- [107] C. Pinkenburg et al. Elliptic flow: Transition from out-of-plane to in-plane emission in Au + Au collisions. *Phys. Rev. Lett.*, 83:1295–1298, 1999.
- [108] G. Baym and P. Braun-Munzinger. *Nucl. Phys. A*, 610:286c, 1996.
- [109] Scott Pratt. General Charge Balance Functions, A Tool for Studying the Chemical Evolution of the Quark-Gluon Plasma. *Phys. Rev.*, C85:014904, 2012.
- [110] L. Adamczyk et al. Beam-Energy Dependence of Charge Balance Functions from Au+Au Collisions at RHIC. Submitted Jul. 13, 2015.
- [111] P. Chung et al. Near threshold production of the multistrange xi- hyperon. *Phys. Rev. Lett.*, 91:202301, 2003.
- [112] Norbert Herrmann, editor. *Technical Design Report for the CBM Time-of-Flight System (TOF)*. GSI, Darmstadt, 2014.